UNIVERSIDADE D
COIMBRA

Seomara Adão Félix

# Neutron imaging detector with ultra-thin $^{10}B$ layers

**Dissertação no âmbito do Mestrado em Engenharia Física orientada pelo Doutor Fernando Domingues Amaro e pelo Doutor Carlos Alberto de Oliveira Henriques, apresentada ao Departamento de Física da Faculdade de Ciências e Tecnologia da Universidade de Coimbra.**

Setembro de 2022

UNIVERSIDADE D
COIMBRA

Seomara Adão Félix

# Neutron imaging detector with ultra-thin $^{10}B$ layers

*Dissertação apresentada à Universidade de Coimbra para cumprimento dos requisitos necessários à obtenção do grau de Mestre em Engenharia Física.*

Orientadores:
Professor Doutor Fernando Amaro, Universidade de Coimbra
Professor Doutor Carlos Henriques, Universidade de Coimbra

Júri:
Professora Doutora Filipa Borges, Universidade de Coimbra
Professor Doutor Carlos Azevedo, Universidade de Aveiro
Professor Doutor Fernando Amaro, Universidade de Coimbra

Setembro de 2022

*"Mudem-me os deuses os sonhos,*

*mas não o dom de sonhar."*

- Fernando Pessoa

# Agradecimentos

Antes de mais, quero agradecer a todos os membros do GIAN por me terem acolhido.

Deixo um agradecimento aos meus orientadores. Ao professor Fernando Amaro, que me recebeu neste projeto, que partilhou comigo os seus ensinamentos e que esteve sempre disponível para as minhas questões. Ao professor Carlos Henriques, pela opinião científica ao longo da dissertação. Agradeço, também, ao professor Luís Panchorrinha Fernandes, que me deu a conhecer o GIAN.

Um agradecimento especial ao estudante de doutoramento Pedro Silva que me acompanhou desde o primeiro dia. Obrigada pelos ensinamentos, pelas experiências e pela paciência.

Ao Doutor Sérgio do Carmo, pelo acesso ao ICNAS e pela ajuda que providenciou durante os testes.

Obrigada a todos que, de certa forma, contribuiram para a minha educação.

Não poderia, também, deixar de agradecer às pessoas que tornaram isto possível. Um eterno agradecimento aos meus pais, que sempre me apoiaram incondicionalmente: à minha mãe, que cuidou de mim da melhor forma possível, e ao meu pai, que me transmitiu a paixão pela engenharia. Ao Henrique, por sempre partilhar as minhas alegrias e as minhas tristezas. À Laura, por ser a irmã mais chata, todavia, mais amiga que poderia ter. Aos meus amigos que me acompanharam nos melhores e nos piores momentos, desde o primeiro cortejo à escrita desta dissertação. E, por fim, à minha família pelo carinho e pelo orgulho que sempre transmitiram.

A todos, agradeço do fundo do coração por me permitirem colocar Eng[a] antes do nome.

# Abstract

Since the last 60 years, neutrons have played an important role in the characterization of materials because of their unique properties. Emerging applications have driven the evolution of neutron science in terms of detection technology, investment, and new large-scale research facilities. Notwithstanding, in the last two decades there has been a shortage of the considered golden standard gas for neutron detection: $^{3}$He. This crisis is mainly on account of the massive application of neutron detectors for homeland security purposes. For this reason, alternative techniques have been researched, being the reaction of $^{6}$Li and $^{10}$B the most attractive ones.

A new technique of slow neutron detection is discussed in this thesis. This novel detector consists of a detection layer composed by a thin $B_4C$ film deposited on an also thin mylar substrate, a gas medium, and two independent readout systems (MWPCs) on each side of the layer. From the interaction between a neutron and a $^{10}$B atom, an alpha particle and a $^{7}$Li ion are emitted along the same line, but in opposite directions. The aim of using ultra-thin $^{10}$B layers is to allow both secondary particles to simultaneously escape the detection layer. So, each reaction product is detected on each side of the conversion layer by each MWPC. Since they are emitted back-to-back, the neutron position can be reconstructured by determining the particle's track centroid and its deposited energy recorded by the two readout systems. This technique improves the spatial resolution when compared to conventional detectors with thick detection layers. Through Garfield++ simulations, a spatial resolution of 0.28 $mm$ using a $B_4C$ layer with thickness of 1 $\mu m$ on a 0.9 $\mu m$ mylar substrate.

**Keywords:** Neutron detectors, (cold, thermal, fast) neutrons, gaseous detectors, spatial resolution, Garfield++ simulations.

# Resumo

Desde os últimos 60 anos, os neutrões têm tido um papel importante na caracterização de materials devido às suas propriedades únicas. As novas aplicações têm levado à evolução da ciência de neutrões no que toca à sua deteção, investimento e novas instalações de pesquisa. No entanto, nas últimas duas décadas tem sido preocupante a escassez de $^{3}$He, que é o gás considerado como "golden standard" para deteção de neutrões. Esta crise é maioritariamente devida à aplicação massiva de detetores de neutrões para propósitos de segurança nacional. Por esta razão, técnicas alternativas têm sido estudadas, sendo que as mais apelativas são as reações de $^{6}$Li e $^{10}$B.

Nesta dissertação, é discutida uma nova técnica de deteção de neutrões térmicos. O novo detetor consiste numa camada de deteção composta por um filme fino de $B_4C$ depositado num susbtrato fino de mylar, um meio gasoso e dois sistemas de deteção independentes (MWPCs) colocados em cada lado da camada. Da interação de um neutrão com um átomo de $^{10}$B, uma partícula alfa e um ião $^{7}$Li são emitidos na mesma linha, mas com direções opostas. O propósito de utilizar camadas muito finas de $^{10}$B é permitir que ambas as partículas secundárias escapem simultaneamente da camada de deteção. Desta forma, cada produto da reação é detetado em cada lado da camada de conversão por cada MWPC. Como são emitidos na mesma linha com direções opostas, a posição do neutrão pode ser reconstruída determinando o centróide do seu percurso no gás e a sua energia depositada através das duas MWPCs. Esta técnica melhora a resolução espacial quando comparada com detetores convencionais com camadas de deteção espessas. Através de simulações computacionais em Garfiedl++, a resolução espacial obtida é de $0,28\,mm$ usando uma camada de $B_4C$ com uma espessura de $1\,\mu m$ depositada num substrato de mylar de $0,9\,\mu m$ de espessura.

**Palavras-chave:** Deteção de neutrões, neutrões (frios, térmicos e rápidos), detetores gasosos, resolução espacial, Garfield++.

# List of Tables

# List of Figures

# List of Acronyms

**BN** Boron nitride.

**$B_4C$** Boron carbide.

**$CH_4$** Methane.

**$CO_2$** Carbon dioxide.

**CSNS** China Spallation Neutron Source.

**ESS** European Spallation Source.

**FWHM** Full Width at Half Maximum.

**GEM** Gas Electron Multiplier.

**HV** High Voltage.

**IBA** Ion Beam Applications.

**ICNAS** Institute for Nuclear Sciences Applied to Health.

**ILL** Institute Laue-Langevin.

**J-Parc** Japan Proton Accelerator Research Complex.

**LIBPhys** Laboratory for Instrumentation, Biomedical Engineering and Radiation Physics.

**M** Multiplication factor.

**MWPC** Multi-wire Proportional Chambers.

**PC** Proportional Counter.

**PHS** Pulse Height Spectrum.

**PSF** Point Spread Function.

**PSI** Paul Scherrer Institute.

**PSND** Position Sensitive Neutron Detector.

**R&D** Research and development.

**RKF** DriftLineRKF Garfield++ class.

**RPM** Radiation Portal Monitor.

**SNS** Spallation Neutron Source.

**Z** Atomic number.

# Contents

# Chapter 1

# Introduction

## 1.1 Motivation and Outline

The neutron is a fundamental particle with neutral charge and one of the constituents of the atom. It was discovered by James Chadwick in 1932: he firstly introduced the "possible existence of a neutron" [1] and thereafter the "existence of a neutron" [2]. The discovery of the neutron quickly changed scientists' view of the atom and the technology to probe other nuclei.

Because of their chargeless characteristics, neutrons have high penetration power and low probability of interaction in matter. Because of these unique characteristics, neutrons play an important role in matter investigation in various scientific fields. Neutrons have high applicability in areas such as radiation physics, crystallography, archaeology, biology, medicine and homeland security [3]. Neutrons can be used to penetrate deep into a target nucleus, revealing information about the material's structure and properties. There are a variety of techniques that use neutrons to study samples: neutron imaging, diffraction, spectroscopy, reflectometry and small angle scattering. In all of these techniques it is necessary to detect neutrons that were transmitted or scattered by the sample.

The neutron has no electric charge, so it is not subject to Coulomb interactions with atomic electrons; however, it interacts with atoms' nuclei. When a neutron interacts with a nuclei, its energy or direction may be changed significantly, or it may totally disappear and be replaced by one secondary radiations. In fact, to be detected neutrons may undergo nuclear capture reactions. A nuclear capture reaction is commonly used due to the creation of secondary charged particles, which can be directly detected. For this reason, neutron detectors utilize a conversion material to convert the incident neutron into secondary charged particles. Consequently, neutrons are detected indirectly by the detection of the secondary particles using a known reaction. The target-nuclei commonly used are $^{3}$He, $^{10}$B and $^{6}$Li.

The most typical neutron-to-charged particle convertor is Helium-3. The Proportional Counter filled with $^{3}$He gas is the ideal neutron detector and considered the "golden standard" for neutron detection: the gas is non-toxic and does not present electron attachment, the detection efficiency is high, and the gamma-ray discrimination is reasonable [44]; hence, this detector has been widely used.

Neutron detectors are primarily used in science and research; however, they have ad-

ditional noteworthy applications: national and homeland security, and industry. Neutron detectors based on Helium-3 can register the presence of fissionable nuclear material (like plutonium) by absorbing the neutrons emitted by the material. After the attacks of September 11, 2001, the federal USA government implemented an aggressive program by deploying neutron detectors at the U. S. border to prevent smuggling of nuclear and radiological material. Despite the initial $^{3}$He vast abundancy, its consumption outweighs its production and thus the $^{3}$He shortage was recognized in 2010. Restricted measures were implemented forcing scientists to dedicate efforts to find sustainable alternatives for $^{3}$He.

The European Spallation Source (ESS) is currently under construction in Lund, Sweden, and aspires to become the most powerful pulsed neutron beam. This state-of-the-art facility requires state-of-the-art equipment, namely detectors with excellent detection efficiency, high rate-capability, and outstanding spatial resolution [40][41][42]. The alternatives for $^{3}$He must fulfill the requirements of new neutron facilities and achieve similar specifications as $^{3}$He Proportional Counters. The most suitable candidates to replace $^{3}$He are: $^{10}$B and $^{6}$Li [4] [18]. Concerning this thesis, $^{10}$B is the chosen alternative for the implementation of the novel detector presented in this thesis, for the reasons discussed in Chapter 3. From the interaction of a neutron and a $^{10}$B atom results an $\alpha$-particle and a $^{7}$Li ion. Because of energy and momentum conservation, the two secondary particles are emitted in the same line but in opposite directions. For conventional boron-lined detectors, only one of the reaction products escapes the boron layer into the gas volume in order to be detected. The other one is absorbed by the boron layer or the substrate; therefore, part of the neutron's information is lost since only one secondary particle is recorded.

This thesis focuses on the development of a novel neutron detection technique based on the implementation of micrometric boron-based conversion layers in gaseous detectors. The goal of this detector is to simultaneously detect both secondary particles that are emitted in a single $^{10}$B neutron capture reaction.

The physical fundamentals behind the interaction of radiation (charged and uncharged) with matter, neutron detection, and gaseous radiation detectors are briefly explained in Chapter 2.

In Chapter 3, an overview on the latest neutron detection technique is reported. This chapter also describe the impact of the $^{3}$He-shortage on neutron research and the requirements of current neutron spallation sources.

Chapter 4 introduces the coincidence detector. It describes the limitations of boron-coated gaseous neutron detectors in terms of spatial resolution, and the operating principle, geometry and materials of the coincidence detector.

The Garfield++ simulations are detailed in Chapter 5. Initially a brief description of the Garfield++ toolkit, the simulation setup, the classes used, and the detector's geometry in the simulation is done. Thereafter, it is performed a gain analyzes to optimize the applied voltages, a study of the reduced electric field in the most sensitive areas in the detector, a determination of the electron drift time, and a calculation of the induced current in the wires. Given that, the neutron capture site is reconstructed and the spatial resolution of the coincidence detector determined.

The detector was tested at ICNAS, a research facility of the University of Coimbra. In Chapter 6, the experimental setup is represented and explained, and the results are

analyzed.

Finally, Chapter 7 describes the principal conclusions and future work.

## 1.2 Scientific contribution

The efforts applied in the development of the neutron detector presented in this thesis resulted in the following publication:

*Improving position resolution of neutron detectors with ultra-thin $B_4C$ foils*, N. F. V. Duarte, J. S. Marcos, A. Antognini, C. Klauser, S. A. Felix, C. M. B. Monteiro, and F. D. Amaro, Journal of Instrumentation, vol 17 (2022).

# Chapter 2

# Scientific background

To easily understand the concept of this novel detector, a theoretical introduction on neutron detection is essential. It is also key to comprehend the physical fundamentals of the interaction of radiation with matter.

## 2.1 Interaction of radiation with matter

Particle detection techniques and devices are based on radiation interaction with matter and effects produced by it: depending on the type of material, the type of radiation, and its energy, different reactions and processes may occur allowing the detection and identification of particles.

Radiation can be divided into two main groups: charged radiations and uncharged radiations (table 2.1). On the one hand, charged radiations have an electric charge associated to the particles and therefore interact with the medium through Coulomb forces. On the other hand, uncharged radiations have no electric charge and thus are not subject to the Coulomb force. To be detected these type of radiation must first undergo scattering or absorption reaction.

| Charged radiations | Uncharged radiations |
|---|---|
| Heavy charged particles (alpha, protons, fission products, etc.) | Neutrons (slow and fast neutrons) |
| Electrons and positrons | Electromagnetic radiations (X-rays and gamma rays) |

**Table 2.1:** Types of radiation: charged and uncharged

### 2.1.1 Heavy charged particles

Heavy charged particles are energetic ions with mass of one atomic mass or greater, such as protons, alpha particles, and other ions. Protons are the fundamental heavy charged particles.

Heavy charged particles interact with the medium through inelastic collisions with orbital electrons of the absorber atoms. In these collisions these particles transfer energy to the atoms.

When a heavy charged particle enters an absorbing medium, it interacts simultaneously with multiple electrons due to the attractive Coulomb force. Depending on the transferred energy, a orbital electron can go to a higher energy electronic shell, or be removed from the atom. The latter process is called ionization. In any interaction, the transferred energy is a small fraction of incident particles' energy. Since particles interact simultaneously with many electrons, they lose its energy continuously along its trajectory. As a result, its velocity is decreased and eventually the particle stops when most of their energy is transferred. The stopping power, $S$, is the average energy loss per unit path length in a given material:

$$S = -\frac{dE}{dx} \tag{2.1}$$

The probability for an interaction to occur is given by the cross section. For a thin layer of material, this probability is proportional to the thickness and to the number of possible target particles per unit volume in the material.

The trajectory of heavy charged particles in a medium is approximately a straight line since they lose small fractions of their energy in each interaction; therefore, only a great number of collisions can slightly deflect their trajectory. This is due to particles' mass when compared to electrons' mass [4].

Assuming that the energy loss of a charged particle in matter is continuous, the range of the particle is a well defined quantity. The range is the distance that a particle travels inside a material before losing all their energy, and depends on the type of particle, their energy, and the type of material. Hence, heavy charged particles are characterized by a precise range.

### 2.1.2 Electrons and positrons

Electrons and positrons are similar to heavy charged particles when interacting with matter. The difference lies on their smaller mass: electrons and positrons lose a larger fraction of their energy in each collision, and so they are easily deflected when compared to heavy charged particles. Depending on their energy, electrons and positrons may undergo a significant energy loss by radiative emission. This process is called Bremsstrahlung emission and is more noticeable as particles' energy increases.

In short, the total energy loss of electrons and positrons is not only due to collisions, but also due to electromagnetic radiation emission. As a result, the energy loss of electrons and positrons fluctuates much more than on heavy particles [5].

### 2.1.3 Electromagnetic radiation

In this context, electromagnetic radiation is constituted by photons, also called X-rays and gamma rays, that travel with the speed of light $c$ and they have zero rest mass and charge.

Because of the lack of an electric charge, photons cannot interact with matter as charged particles. Instead, the main three process X-rays and gamma rays interact with matter are: photoelectric effect, Compton scattering, and pair production.

#### Photoelectric effect

This process involves the absorption of a photon by an atomic electron. This electron, called photoelectron, is then ejected from the atom with kinetic energy equal to the difference between the photon energy and the binding energy of the respecting atomic shell. The energy of the photoelectron is: $E = E_{photon} - E_{Binding} = hf - E_{Binding}$, given $h$ the Planck constant and $f$ the photon frequency.

#### Compton scattering

Electrons are normally bound in a medium; however, if the photon energy is higher than the binding energy of the electron, this last can be considered free. On that ground, the Compton effect is the collision between a photon and a free electron: the incoming photon is then deflected by an angle $\theta$ with respect to its original direction and a fraction of its energy is transferred to the electron (recoil electron).

#### Pair production

Pair production is an interaction between a photon and a nucleus. As a result, the photon disappears and an electron-positron pair appears. In order for this process to happen, the momentum must be conserved, which is accomplished by the presence of the nucleus, and the photon energy must exceed twice the rest mass of an electron (1.02 MeV) [6]. The nucleus does not undergo any change.

Due to its neutral charge, X-rays and $\gamma$-rays are more penetrating in matter than charged particles. Furthermore, the energy of a beam of photons does not degrade while crossing a material, instead it is only attenuated in intensity, e.g., the total number of photons is reduced in respect to the ones absorbed by the material. The linear attenuation coefficient represents the attenuation of photons. The total probability for interaction is given by the sum of the three linear coefficients for photoelectric effect, Compton scattering, and pair production.

### 2.1.4 Neutrons

Neutrons have neutral charge, consequently they are not subject to Coulomb interactions with electrons and nuclei. Their principal means of interaction is through the strong force with nuclei. In terms of charge, neutrons and electromagnetic radiation are identical (table 2.1).

Notwithstanding neutrons and electromagnetic radiation having neutral charge, the way one interacts with matter is distinct. X-rays and $\gamma$-rays interact with atomic electrons whereas neutrons interact (mainly) with atomic nucleus.

When a neutron does interact with matter, four main mechanisms can occur: elastic and inelastic scattering - scattering interactions -, neutron capture reactions, and nuclear fission - absorption reactions. In scattering interactions both neutron and nucleus reappear after the reaction; the neutron loses part of its energy in every collision. In absorption reactions the neutron disappears and it is replaced by one or more secondary radiations. The type of mechanism to occur depends on neutrons energy and type of material. Neutrons can be classified regarding their energy [5]. Despite the classification, no boundaries between classes are defined.

**Elastic scattering**

When a neutron suffers an elastic collision, the total kinetic energy of the two colliding particles is conserved. Part of neutron's kinetic energy is transferred to the recoil nucleus and thus the neutron velocity is decreased and its direction its changed. This is the principal mechanism of energy loss for neutrons in the MeV region [6].

**Inelastic scattering**

When a neutron suffers an inelastic collision, the total kinetic energy of the two colliding particles is not conserved. Part of neutron's energy is transferred to the nucleus, exciting it. As a result of nucleus excitation, the latter will return to the ground state emitting characteristic gamma-rays and losing a greater fraction of its energy than it would in an equivalent elastic collision [6]. To excite the nucleus the neutron must have an energy of 1 MeV or more [5].

**Neutron capture reactions**

In this mechanism the nucleus of the material absorbs the neutron, which is then in an excited state. The nucleus decays by producing secondary radiation: gamma-rays (radiative neutron capture), heavy charged particles, or conversion electrons. For this process to occur there are no requirements in terms of neutron energy; however, the reaction must have positive Q-value to be energetically possible [6][7]. The Q-value is the absorbed or released energy by the nuclear reaction.

At low energies the neutron capture cross section is proportional to the reciprocal of neutron's velocity, e.g, proportional to $1/v$ [5][7]. Therefore, it is more likely for a neutron capture reaction to occur if they travel at lower velocities and thus at lower energies.

For slow neutrons, their initial kinetic energy can be neglected when compared to the absorption reaction energy, which is several orders of magnitude greater. Because of that and since energies of the two fragments are calculated from energy and momentum conservation, they are emitted back-to-back. At the moment of creation of the two fragments, the atomic electrons are dispersed, thus they carry a net electric charge [8].

The indirect detection of cold and thermal neutrons is mainly achieved through neutron caption reactions. Reactions in which secondary radiation is emitted in the shape of charged particles, are more attractive since the latter is directly detected. Such reactions are (n, $\alpha$),

(n, p), (n, t), which respectively result in the emission of an alpha particle, a proton, and a triton, along with the ion formed by the neutrons and protons of the absorption nucleus.

**Nuclear fission**

When a neutron is absorbed by a nucleus it creates an unstable compound nucleus. Because of its instability, it splits into smaller nuclei (fission fragments) and releases two or more neutrons and gamma-rays. Fission fragments decay by $\beta^-$ decay [7]. Energy release by nuclear fission is greater than the typical Q-values of neutron capture reactions. Some fissile products that are capable of neutron absorption and make fission possible are: $^{233}$U, $^{235}$U, and $^{239}$Pu.

The neutron has a rest mass of 939.56 MeV, slightly greater than of the proton and is unstable when not bound in a nucleus undergoing $\beta^-$ decay:

$$n \rightarrow p^+ + e^- + \overline{\nu_e} \tag{2.2}$$

Its half-time is $(888.1 \pm 2.0)s$ [9]. The total probability for a neutron to interact in matter is given by the sum of the individual cross sections:

$$\sigma_{total} = \sigma_{elastic} + \sigma_{inelastic} + \sigma_{capture} + \sigma_{fission} \tag{2.3}$$

Multiplying $\sigma_{total}$ by the number of nuclei per unit volume, $N$, gives the probability for a neutron to interact per unit path length, $\Sigma_{total}$:

$$\Sigma_{total} = N\sigma_{total} = \frac{N_A \cdot \rho}{M}\sigma_{total} \tag{2.4}$$

given $\rho$ the material density, $N_A$ the Avogadro number, and $M$ the atomic mass. Analogous to photons, when a beam of monoenergetic neutrons with intensity $I_0$ passes through a material of thickness $t$, the number of neutrons that emerges without interacting with matter is:

$$I(t) = I_0 e^{-\Sigma_{total} t} \tag{2.5}$$

Meaning that a beam of neutrons is exponentially attenuated by an absorber. The average distance between two successive interactions, e.g. the mean free path, is given by $\lambda = 1/\Sigma_{total}$.

## 2.2 Neutrons

### 2.2.1 Neutron sources

Neutrons are valuable particles because of their applications; therefore the production of free neutrons is of high significance. Isotope sources of neutrons similar to gamma-ray sources are not available and do not exist. Neutron sources are much more limited and are

restricted to isotopic sources (spontaneous fission, radioisotope sources, and photoneutron sources), nuclear reactors and spallation sources.

On the one hand, isotopic sources are small, portable, and easy to handle; however, they have a very low neutron emission rate and can have a high gamma-ray emission rate. These are not the most appropriate neutron sources for neutron research. These sources are also continuously emitting neutrons, resulting in a large waste of neutrons during their life time. On the other hand, nuclear reactors and spallation sources produce a high flux of neutrons, which is more attractive for neutron detection. Nuclear reactors produce a continuous flux of neutrons and spallation sources a pulsed neutron source. For safety reasons and new mandatory regulations, nuclear reactors have become less common, moving the attention to spallation sources.

**Spontaneous fission**

Spontaneous fission is a radioactive decay where an atom's nucleus splits into two smaller nuclei and one or more neutrons. The most commonly used spontaneous fission source is $^{252}$Cf: a neutron-rich isotope that has a half-life of 2.73 years. It decays either by $\alpha$-particle emission or by spontaneous fission with a branching ratio of 96.9% to 3.1%. The neutron emission rate is $2.3 \times 10^{15}\ n\ s^{-1}\ kg^{-1}$ (average n-energy 2.35 MeV) [10]. A sample of such radionuclide can be a convenient isotopic neutron source in the sense that it can provide a useful neutron intensity over a sufficiently long half-life.

**Radioisotope sources**

Another possible way to fabricate a neutron source is by mixing an alpha-emitting isotope with a low atomic weight isotope: ($\alpha$, n) reactions. One common example is the beryllium source, which produces neutrons in the following sequence.

$$^{4}_{2}\alpha + ^{9}_{4}\mathrm{Be} \rightarrow ^{12}_{6}\mathrm{C} + ^{1}_{0}\mathrm{n} \quad (Q = 5.71\,MeV) \tag{2.6}$$

Other common example is the Americium-Beryllium, typically designated as AmBe source.

$$^{241}\mathrm{Am} \rightarrow ^{237}\mathrm{Np} + ^{4}\alpha + \gamma \quad (Q = 5.48\,MeV) \tag{2.7}$$

Americium-241 has a half-life of 433 years and decays by $\alpha$ emission. The $\alpha$-particles interact with beryllium producing neutrons (eq. 2.6). The problem of this source is the high gamma-ray emission rate which is orders of magnitude higher than the neutron yield.

**Photoneutron sources**

Like $\alpha$-particles, photons can also be used to stimulate nuclei to emit neutrons: ($\gamma$, n) reactions. Neutron emission results in the absorption of a gamma-ray photon with sufficient excitation energy. There are two target nuclei considered.

$$^{9}_{4}\mathrm{Be} + h\nu \rightarrow {}^{8}_{4}\mathrm{Be} + {}^{1}_{0}\mathrm{n} \quad (Q = -1.666\,MeV) \tag{2.8}$$

$$^{2}_{1}\mathrm{H} + h\nu \rightarrow {}^{1}_{1}\mathrm{H} + {}^{1}_{0}\mathrm{n} \quad (Q = -2.226\,MeV) \tag{2.9}$$

Because the Q-value is negative, a gamma-ray with an energy of at least the absolute value of Q is required.

**Nuclear reactors**

Nuclear reactors produce neutrons in large numbers as a result of neutron-induced reactions.

$$^{235}\mathrm{U} + {}^{1}\mathrm{n} \rightarrow {}^{236}\mathrm{U}^{*} \rightarrow fission \tag{2.10}$$

The element $^{236}$U can generate many fission fragments such as neutrons. Although many of these neutrons are used to produce more fission fragments, a large number of them manage to escape the nuclear core and thus be used in a laboratory setting. As common practice, due to the small natural abundance of $^{235}$U, nuclear reactions use $^{235}$U enriched with $^{238}$U (> 90%) to generate high neutron fluxes.

The Institute Laue Langevin (ILL) [11] in France, the Source Heinz Maier-Leibnitz (FRM II) [12] in Germany, and the PIK reactor [13] in Russia are examples of nuclear reactors aimed at for neutron research.

**Spallation sources**

Spallation is a violent reaction in which a target composed with high Z materials (such as lead, tungsten, silver, or bismuth) is bombarded by very high energy protons. The incident proton disintegrates the nucleus through inelastic nuclear collisions, resulting in the emission of protons, neutrons, $\alpha$-particles, and others. Protons are accelerated up to relativistic speeds using either a linear accelerator, a cyclotron, or a synchrotron in order to have sufficient energy to provide spallation.

Compared to nuclear reactors, spallation sources achieve peak intensities of 1 or 2 orders of magnitude higher. Neutron reactors have a continuous flux of neutrons and spallation sources a pulsed neutron beam.

Examples of spallation sources are: ISIS (United Kingdom) [33], SINQ (Switzerland) [34], SNS (USA) [35], J-PARC (Japan) [36], and CSNS (China) [37]. The European Spallation Source (ESS) [38] is being constructed in Sweden and is aiming to become the most powerful pulsed neutron beam.

Unlike the other spallation sources, the SINQ spallation source can be considered a continuous neutron source: the PSI-accelerator system consists of two isochronous cyclotrons, producing a proton beam with a time interval of 20 *ns* between pulses; this interval is irrelevant for thermal neutrons and thus can be ignored [14].

### 2.2.2 Neutron classification

Neutrons can be classified according to their energy; however, there are no defined limitations between classes and many energy classifications can be found across literature. One present classification will be considered in this work [5].

| Term | Energy | Velocity (m/s) | Wavelength (nm) | Temperature (K) |
|---|---|---|---|---|
| Ultracold | <0.2 $\mu eV$ | <6 | >64 | <0.002 |
| Very cold | 0.2 $\mu eV \leq E <$ 50$\mu eV$ | $6 \leq v < 100$ | $4 < \lambda \leq 64$ | $0.002 \leq T < 0.6$ |
| Cold | 0.05 meV <E ≤ 25$meV$ | 100 <v ≤ 2200 | $0.18 \leq \lambda < 4$ | 0.6 <T ≤ 300 |
| Thermal | 25 meV | 2200 | 0.18 | 300 |
| Epithermal | 25 meV <E ≤ 500$keV$ | 2200 <v ≤$1\times10^7$ | | |
| Fast | ≥ 500$keV$ | $>1 \times 10^7$ | | |

**Table 2.2:** Common terminology of neutron classification. Table from [15].

Ultracold neutrons have very low energies and thus low velocities, and have unique characteristics: they undergo total reflection at any angle of incidence, they behave like an ideal non-interacting gas, and they can be relatively easily confined and manipulated [16]. Therefore, they are a unique tool to study the properties of the neutron itself. Producing ultracold neutrons is not an easy task as it requires an extra moderation mechanism to reduce neutron's energy. Cold and thermal neutrons are the most commonly used in neutron research as they are easy to produce.

The energy a neutron has when it is released from the nucleus corresponds to the energy range of fast neutrons; therefore, neutrons are always originally emitted as fast neutrons. To become thermal, cold, etc., neutrons must go through an energy loss mechanism known as neutron moderation.

### 2.2.3 Neutron moderation

Neutron moderation is a process to reduce neutron's energy by repeated elastic and inelastic collisions with free nuclei. This process allows a neutron to slow down without being captured by the moderator.

In each collision, the neutron transfers a fraction of its kinetic energy to the target nucleus in the form of kinetic energy (elastic collision) or excitation energy (inelastic collision). By repeated elastic and/or inelastic collisions, the neutron loses part of their energy and is slowed down.

The selection of the moderator must be rigorously considered: the moderator must be "transparent" to neutrons, it must remove a large amount of energy from neutrons in a single collision, and the process must be as brief as possible to avoid captures by other nuclei.

Energy loss per collision goes down with nuclear mass and the rate of collisions goes up with higher scattering cross-section. Consequently, the moderator must have low mass numbers and high scattering cross-section in order to slow down neutrons. The most efficient moderator is hydrogen because neutrons can lose a large fraction of their energy

in a single collision. As a result, the most common moderators are water, paraffin and polyethylene (hydrogenous materials).

### 2.2.4 Neutron detection

Neutrons do not ionize atoms directly, and thus are detected indirectly by the production of a charged particle or a photon when interacting with a material. As seen in section 2.1.4, neutrons interact with matter through four mechanisms: elastic and inelastic collisions, nuclear capture reactions, and nuclear fission.

The fundamental principle of neutron detection is neutron conversion. To identify a passage of a neutron, the secondary radiation produced by its interaction with matter must be detected, hence neutron-to-charged-particle conversion is key. A neutron detector is a combination of a conversion material and a conventional radiation detector. The conversion material is designed to convert neutrons into energetic charged particles, such as protons, alpha particles, etc., possible to be detected by the radiation detector. This latter can be any type of radiation detector: solid, liquid, gaseous, or a combination.

The principal mechanism of interaction used in neutron detectors are nuclear capture reactions of type (n, charged particles).

Choosing the conversion material is a major aspect in designing neutron detectors. To achieve the best detector performance, a careful search and consideration must be done. The neutron capture reaction cross-section should be high enough to achieve a high detection efficiency. Depending on the isotope used for the neutron conversion reaction, several types of reaction products can be produced. Other aspect is to consider the best reaction products for the detection technique in use.

The cross-section for neutron interactions in most materials is a strong function of neutrons energy: $1/\sqrt{E}$; therefore, nuclear capture reactions are more likely to occur in low energies, such as cold and thermal neutrons. Nonetheless, there are no requirements in terms of neutron's energy, only the obligation for the reaction to have a positive Q-value. This is due to the possible low energy of the incoming neutron. The kinetic energy of the reaction products is given by the Q-value for the same reason. Then, the goal is to choose the neutron capture reaction with the higher Q-value. Other aspects may be considered such as robustness, price, and toxicity.

| Isotope | Isotopic abundance | $\sigma_{\text{th}}$ (barn) | Reaction products | Q-value (MeV) |
|---|---|---|---|---|
| $^{3}$He | 0.0002% | 5330 | t, $\alpha$ | 0.764 |
| $^{6}$Li | 7.6% | 940 | t, $\alpha$ | 4.78 |
| $^{10}$B | 19.9% | 3840 | $\alpha$, $^{7}$Li, $\gamma$ | 2.31 (94%)<br>2.79 (6%) |
| $^{113}$Cd | 12.2% | 20600 | $\gamma$,e$^{-}$ | 9.04 |
| $^{155}$Gd | 14.8% | 609000 | $\gamma$,e$^{-}$ | 8.54 |
| $^{157}$Gd | 15.7% | 254000 | $\gamma$,e$^{-}$ | 7.94 |

**Table 2.3:** Neutron capture reactions: isotopic abundance, cross-section, reaction products, and Q-value. Table from [64].

The widely used reactions are the ones which secondary particles are charged particles: $^{3}$He, $^{6}$Li, and $^{10}$B. These are the ones which will be considered in this chapter. From fig. 2.1, the neutron capture cross-section for both $^{3}$He, $^{6}$Li, and $^{10}$B is strongly dependent on the energy of the incoming neutron by a factor of $1/\sqrt{E}$, approximately.

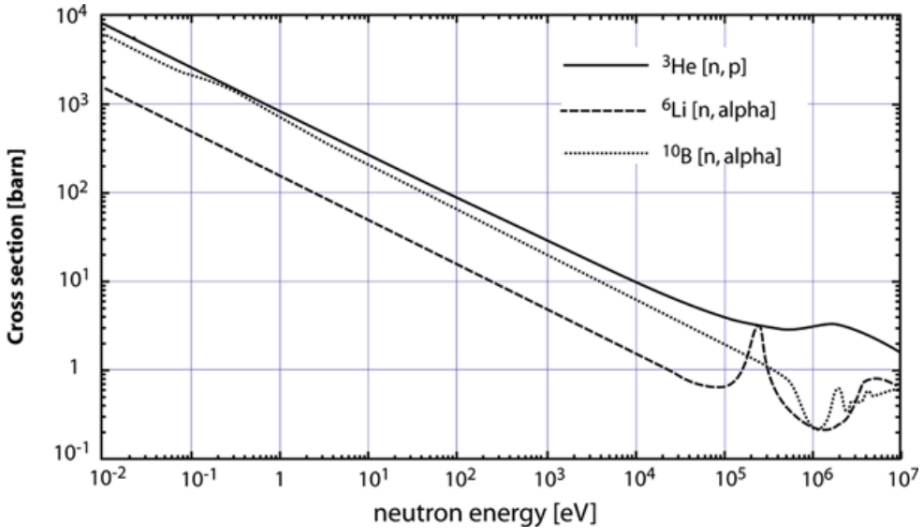


**Figure 2.1:** Neutron capture cross-section as function of incident neutron energy for $^{3}$He, $^{6}$Li, and $^{10}$B. Image from [18], data from [19].

### $^{3}$He reaction

The $^{3}$He-gas is typically used in gaseous proportional counters, and is the most commonly used converter material. Neutron detection by $^{3}$He is based on the reaction:

$$^{3}\mathrm{He} + n \rightarrow {}^{3}\mathrm{H}\ (191\,keV) + p\ (573\,keV) \quad (Q = 0.764\,MeV) \tag{2.11}$$

From the interaction between a neutron and a $^{3}$He atom a proton and a triton ($^{3}$H) are emitted. The cross-section for this reaction is higher than for the other ones of the type (n, charged particles). Due to momentum and energy conservation, both secondary particles are emitted in opposite directions. For cold and thermal neutrons, the Q-value is much higher than the neutron's energy; therefore, it is not possible to extract energy information from neutrons. The main disadvantage of $^{3}$He is its minimal natural abundance of 0.0002%.

### $^{6}$Li reaction

Another reaction for the detection of thermal neutrons is the (n, $\alpha$) reaction in $^{6}$Li, which is based on:

$$^{6}\mathrm{Li} + n \rightarrow {}^{3}\mathrm{H}\ (2.73\,MeV) + {}^{4}\alpha\ (2.05\,MeV) \quad (Q = 4.78\,MeV) \tag{2.12}$$

From the interaction between a neutron and a $^{6}$Li atom an alpha and a triton are emitted in opposite directions due to momentum and energy conservation. The cross-section of

this reaction is lower than for $^{3}$He and $^{10}$B; however, it has a higher Q-value. The reaction products emitted in this reaction interact with scintillating material and thus $^{6}$Li is an interesting convertor for neutron scintillator detectors.

**$^{10}$B reaction**

Neutron detection by $^{10}$B is based on the reaction:

$$n + {}^{10}\mathrm{B} \rightarrow {}^{7}\mathrm{Li}^{*}\ (0.84\,MeV) + {}^{4}\alpha\ (1.47\,MeV) \quad (Q = 2.792\,MeV)(94\%) \tag{2.13}$$

$$\rightarrow {}^{7}\mathrm{Li}\ (1.02\,MeV) + {}^{4}\alpha\ (1.78\,MeV) \quad (Q = 2.310\,MeV)(6\%) \tag{2.14}$$

From the interaction between a neutron and a $^{10}$B atom two situations are possible: an alpha particle and a $^{7}$Li in the first excited state are emitted with 94% probability (eq. 2.13), or an alpha particle and a $^{7}$Li in the ground state are emitted with 6% probability (eq. 2.14). The excited $^{7}$Li returns to its ground state by emitting a gamma-ray with 0.48 MeV. Because of momentum and energy conservation, the particles are emitted in the same line but in opposite directions. The Q-value of the reactions is large when compared to the incoming energy of the thermal neutron, so it is also not possible to extract information about the incoming kinetic energy of the neutron. The cross-section for this reaction is higher than for $^{6}$Li and lower than for $^{3}$He. The Q-value is again between the two reactions: higher than $^{3}$He and lower than $^{6}$Li. The $^{10}$B reaction is exploited both in $BF_3$ Proportional Counters and in Boron-Coated Gaseous Detectors.

The other three mechanisms of interaction (elastic and inelastic collisions, and nuclear fission) can also be used to detect neutrons [17] [4] [18], but are beyond the discussion of this work.

### 2.2.5 Gamma-ray discrimination

Because of neutrons neutral charge, mechanisms to detect neutrons in matter are based on indirect identification, so as for gamma-rays (2.1.3 and 2.1.4). Neutrons interact with matter through scattering and absorption. When a neutron suffers an inelastic collision the nucleus is excited, which quickly de-excites by emitting a gamma-ray. For neutron absorption, it may undergo radiative neutron capture where the secondary radiation is a gamma-ray. Also for nuclear capture reactions a gamma-ray can be emitted. The interaction of a neutron with Boron-10 has a 94% probability of emitting a gamma-ray with energy of 0.48 MeV (reaction 2.13). So, neutrons and gamma-rays are present in the same environments.

Similarly to the neutron, a photon can only be detected after being converted into a charged particle. For low energy photons the most common mechanism is the photoelectric effect. For medium energies the Compton scattering is dominant; moreover, for high energy photons the most usual mechanism is pair production [20]. In gas-filled detectors, a gamma-ray can interact in the gas volume or in the detector walls resulting in a high energy electron

which ionizes the gas while traversing the detector. The range of electrons in such detectors is bigger than the dimensions of the detector, while the range of protons or heavier particles is shorter. Consequently, the total energy of neutron conversion products is deposited in the medium, whereas the electrons energy measured only represents a fraction of its total energy. This leads to a very clear separation between energies deposited by neutrons and gamma-rays. Gamma-ray discrimination is generally done by selecting a cut-off energy in the pulse height distribution. Signals below that threshold are more likely to belong to gamma-rays and thus can be rejected.

To achieve a good gamma-ray discrimination, it is often necessary to select certain detector materials. For low energy gamma-rays, the probability of photoelectric interaction increases with the atomic number: it is proportional to $Z^n$, where $n$ varies between 4 and 5 over the gamma-ray energy region of interest [6]. For this reason, lower $Z$ numbers are chosen: for the detector walls aluminium ($Z = 13$) is preferred over stainless-steel, which is mainly composed by iron ($Z = 26$) [21].

## 2.3 Gaseous radiation detectors

Gaseous radiation detectors basically consist of two electrodes with an electrical potential applied and a filling gas between them. These detectors are based on the collection of the ionization electrons and ions produced by each interaction between the incident particle and the gas.

To detect radiation, first it must undergo interaction with matter through the processes discussed earlier. Depending on the technique and technology in place, it is possible to identify the particles, count them, measure their energy, know their incident position, and track their trajectories in the gas in two or three dimensions.

An example of a gaseous radiation detector is the proportional counter. Its geometry consists of a cylindrical cathode with a thin anode wire centred on its axis. When an electrical voltage is applied, this geometry creates an electric field, which intensity varies inversely with the radius. The PC is mainly used for the detection of low energy X-rays and neutrons.

### 2.3.1 The ionization process in gases

When a charged particle crosses the gas it interacts with it resulting in excited and ionized molecules along its path, given that it has sufficient energy to do so. When a molecule is ionized, a positive ion and a free electron are created, forming an electron-ion pair known as primary ionization. To create this pair, the particle must transfer at least an amount of energy equal to the ionization potential of the gas; however, because other processes may occur, the average energy lost by the particle in each electron-ion pair created (W-value) is greater than the ionization energy. Considering the W-value and knowing the energy of the incident particle, it is possible to estimate the total number of electron-ion pairs formed by each incident particle.

When an electric field is present, the electrons and positive ions are accelerated along the lines of the electric field towards the anode and cathode respectively. The average velocity

is the drift velocity. Because ions are heavier than electrons, the drift velocity of electrons is higher. The time it takes electrons to reach the cathode or ions to reach the anode is called drift time.

If the electrons from the primary ionization have sufficient energy, they can ionize gas molecules when drifting towards the anode. Consequently, a secondary ionization takes place where the produced secondary electrons can also collide with other gas molecules and create additional ionization. This process is called avalanche.

The motion of electrons and ions induces an electric current on the electrodes, which can be collected and measured.

### 2.3.2 Filling gas

To achieve the best specifications of the detector regarding its application, the selection of the filling gas employed in gaseous radiation detectors must be carefully reasoned. Some physical mechanisms are of extreme importance when choosing the gas and will be discussed below; however, practical applications must also be considered such as availability and acquisition price.

During the drift of electrons and ions, interactions with gas molecules may occur: charge transfer, electron attachment, and recombination. These interactions are harmful for the detectors good operation. When a positive ion encounters a neutral gas molecule an electron is transferred from the molecule to the ion, turning the latter into a neutral particle. This interaction is called charge transfer. Depending on the filling gas, the attachment of an electron to a neutral gas molecule forms negative ions. The filling gas must have a low electron attachment coefficient in order for this process to be minimized. A free electron and a positive ion can also collide. The electron is captured by the ion forming a neutral particle. This process is known as recombination [6].

| Gas | Excitation potential (eV) | Ionization potential (eV) | Mean energy for electron-ion pair creation (eV) |
|---|---|---|---|
| $H_2$ | 10.8 | 15.4 | 37 |
| He | 19.8 | 24.6 | 41 |
| $N_2$ | 8.1 | 15.5 | 35 |
| $O_2$ | 7.9 | 12.2 | 31 |
| Ne | 16.6 | 21.6 | 36 |
| Ar | 11.6 | 15.8 | 26 |
| Kr | 10.0 | 14.0 | 24 |
| Xe | 8.4 | 12.1 | 22 |
| $CO_2$ | 10.0 | 13.7 | 33 |
| $CH_4$ | | 13.1 | 28 |
| $C_4H_{10}$ | | 10.8 | 23 |

**Table 2.4:** Excitation and ionization potentials, and W-value for various gases. Table from [5].

In the detection process the ideal is to have a number of electron-ion pairs formed as great as possible; therefore, the average energy lost by the particle in each electron-ion pair

created (W-value) must be as low as possible. Table 2.4 shows the excitation and ionization potentials and the W-value for the most common gases used in gaseous radiation detectors.

Noble gases are a safe choice for gaseous radiation detectors, they have low chemical reactivity, low electron attachment coefficient, and require a lower electric field intensity for an avalanche to occur. Avalanche multiplication happens in noble gases at much lower fields than in complex molecules: this is a consequence of the many non-ionizing energy dissipation modes available in poly-atomic molecules [22]. The most commonly used noble gas is Argon. An avalanche is characterized by ionizations and excitations. The de-excitation of a noble gas particle to the ground state happens through radiative process. The photon can thus generate a new avalanche very soon after the primary, increasing the detector's dead time and causing a proportionality loss between the energy of the incoming radiation and the collected charge. In order to reduce these effects, a poly-atomic gas is added. Because of its rotational and vibrational modes, they can quench photon emission in a wide range of energies. These gases are named quenching gases and are normally $CH_4$ (methane) or $CO_2$ (carbon dioxide). A concentration of about 10% of a quenching gas is sufficient to reduce the effects.

The final aspect to consider is gas purity, which can be achieved either by continuous flow during the detectors operation, or by containing the gas inside the detector. For the latter, a gas purification system is required to remove impurities. This process is used when the filling gas is expensive. When the detector operates in continuous flow, there is no need for a purification system since new gas is always entering the detector.

### 2.3.3 Regions of operation

To collect electron-ion pairs in a gas-filled detector an electric field must be applied in the gas medium. If the electric field inside the detector is strong enough that recombination becomes negligible, and all the charges are efficiently collected without loss. Fig. 2.2 indicates the regions of operation of such detectors.

The first region of operation is the recombination region, where the electric field is not enough to accelerate electrons and ions and thus they suffer recombination. In the ion chamber region, an increase in voltage does not cause a substantial increase in the charge collected. There is no charge multiplication; therefore, the signal is created only by the primary charges. Increasing the voltage, the detector electric field can reach a magnitude above the threshold value and enable charge multiplication. This is the proportional region: the number of secondary charges is proportional to the number of primary charges and thus to the energy of the incident particle.

Increasing the voltage further some non-linear effects are introduced. In the secondary ionization electron-ion pairs are produced. Because electrons are faster, they are quickly collected, whereas ions move much slower. As a result, an ion cloud can be created and thus a space charge which can alter the electric field inside the detector. This is the limited proportional region. If the applied voltage is high enough, the space charge effect can become dominant and reduce the electric field below the threshold value; ergo, the avalanche process is limited. This is the Geiger-Müller region and the region of operation of Geiger-Müller counters. Finally, at higher voltages the electric field generates a continuous discharge of the medium, with the chamber no longer being sensitive to any incident

radiation. This is the continuous discharge region and is a damaging mode of operation for detectors.

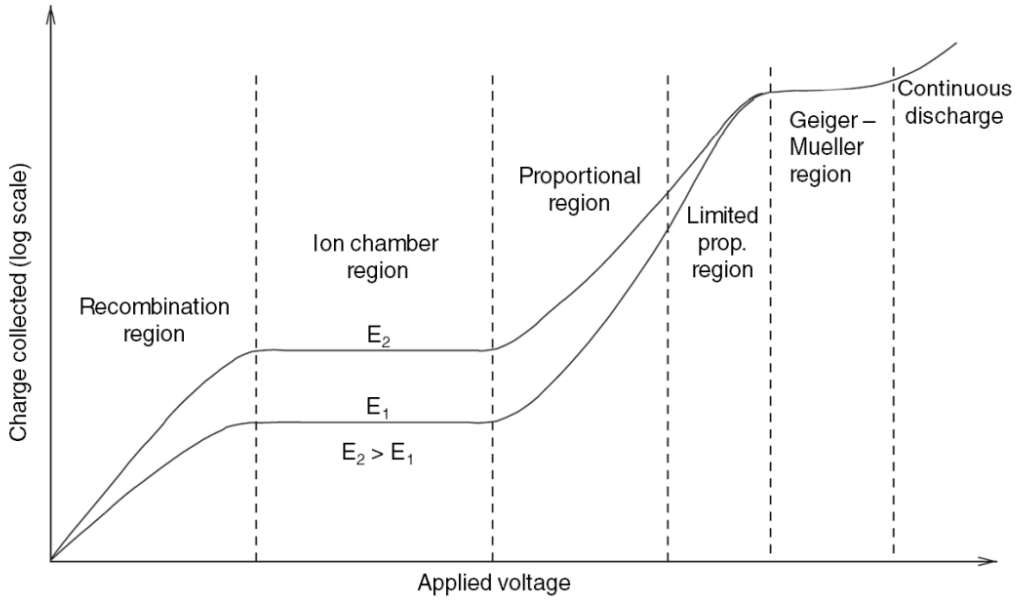


**Figure 2.2:** Regions of operation of gaseous radiation detectors. Pulse height as function of the applied voltage in the anode for two different energies of incident radiation ($E_2 > E_1$). Image from [64].

### 2.3.4 Gas multiplication

As seen, an electron from a primary ionization can be accelerated by the electric field and ionize neutral gas molecules, i.e., each free electron can potentially create more free electrons by ionization. This process forms a cascade of electrons that drift towards the anode, and it is called Townsend Avalanche. The fractional increase in the number of electrons per unit path length is given by the Townsend equation:

$$\frac{dn}{n} = \alpha \, dx \tag{2.15}$$

given $\alpha$ the Townsend coefficient for the gas: its value is zero for electric fields bellow the multiplication threshold and typically increases with the electric field. The total number of electrons created in a path $x$ is given by integrating the Townsend equation (eq. 2.15):

$$n = n_0 e^{\alpha x} \tag{2.16}$$

being $n_0$ the original number of electrons, i.e., the number of primary electron-ion pairs originated in an ionization. This value is given by the ratio between E and W-value of the gas:

$$n_0 = \frac{E}{W} \tag{2.17}$$

where $E$ is the energy deposited in the gas by the incident radiation.

If the detector is working in the proportional region, charge multiplication is happening. The motion of electrons and ions induces an electric current on the electrodes: $Q$ is the total charge generated in the detector.

$$Q = n_0 e M \tag{2.18}$$

given $e$ the elementary charge, and $M$ the gas multiplication factor. This latter is also designated as the detector gain or the gas gain. Considering equation 2.16, the multiplication factor is also given by:

$$M = \frac{n}{n_0} = e^{\alpha x} \tag{2.19}$$

For a cylindrical geometry, where the anode consists of a fine wire positioned along the center axis of a large tube which serves as the cathode, the gas multiplication factor is obtained by integrating the following equation:

$$\ln M = \int_{(a)}^{\varepsilon(r_c)} \alpha \frac{\partial r}{\partial \varepsilon(r)}\, d\varepsilon \tag{2.20}$$

where $r$ is the radius of the detector, $\varepsilon(r)$ is the electric field, $a$ is the anode radius, and $r_c$ is the critical radius, above which the electric field falls below the multiplication threshold. Assuming linearity between $\alpha$ and $\varepsilon$, Diethorn derived the following expression for M [23]:

$$\ln M = \frac{V}{\ln(b/a)} \frac{\ln 2}{\Delta V} (\ln \frac{V}{pa \ln(b/a)} - \ln K) \tag{2.21}$$

given $V$ the applied voltage, $b$ the cathode radius, $p$ the gas pressure, $\Delta V$ the potential difference through which an electron moves between successive ionizing events, and $K$ is the minimum value of $\varepsilon/p$ below which multiplication cannot occur. Variables $\Delta V$ and $K$ are constants for a given gas.

### 2.3.5 General characteristics of a detector

#### Detection efficiency

A very important characteristic of a detector is its detection efficiency. One may consider two types of efficiency: absolute efficiency and intrinsic efficiency.

The absolute or total efficiency depends not only on the detector properties, but also on the detectors geometry. It is given by:

$$\epsilon_{absolute} = \frac{events\ \ registered}{events\ \ emitted\ \ by\ \ the\ \ source} \tag{2.22}$$

The intrinsic efficiency depends only on the type of radiation, its energy, and the detector material, i.e., depends on the detector and source properties. It is given by:

$$\epsilon_{intrinsic} = \frac{events\ \ registered}{events\ \ impinging\ \ on\ \ the\ \ detector} \tag{2.23}$$

Since uncharged radiation must first undergo a reaction to produce secondary charged particles, detecting a good fraction of the incident radiation is complex. For this reason, the detector detection efficiency is of special importance for this type of radiation.

### Dead time

Dead time is the minimum time required for a detector to separate two different events for them to be registered as two separated pulses. During the dead time detectors may be either insensitive or sensitive. If they are insensitive, events that occur during dead time are lost; if they are sensitive, the same events may pile-up on the first event causing a distortion of the signal and loss of information. Dead time affects the detection efficiency directly. For this reason, an energy threshold is defined in order to distinguish radiation interactions from background noise.

### Energy resolution

Energy resolution is the ability for a detector to accurately determine the energy of the incoming radiation, i.e., it is the capacity for a detector to distinguish between two energy values.

The process of avalanche multiplication is statistical in nature, causing fluctuations on the number of ionizations and excitations. As a result, the pulse height spectrum (PHS) of a monoenergetic beam is not a delta-function, but a Gaussian with a well define width. The energy resolution is given by the full width at half maximum (FWHM) of the peak. If $\Delta E$ is the width at energy $E$, the resolution is given by $Resolution = \Delta E/E$. Fig. 2.3 demonstrates two energy peak with different resolutions.

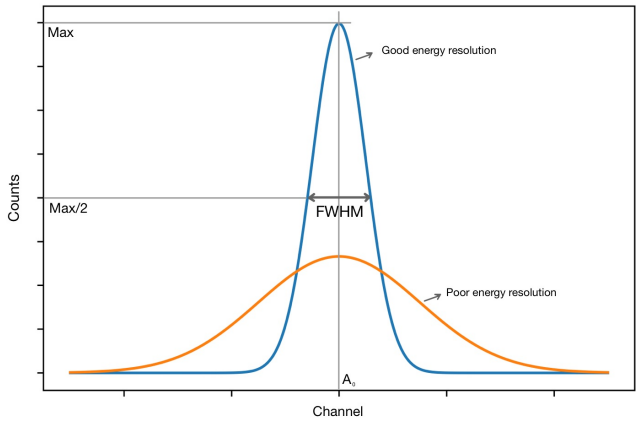


**Figure 2.3:** PHS of two detectors: one with good energy resolution (blue) and other with poor energy resolution (orange).

The smaller the FWHM value is, the better energy resolution the detector has. Considering the $A_0$ the peak centroid of the Gaussian distribution, the energy resolution can also be given as:

$$R = \frac{FWHM}{A_0} \tag{2.24}$$

If the energy deposited in the detector is $E$, the average number of electron-ion pairs produced is $E/W$. Considering that this process can be described as a Poisson distribution, the standard deviation of the number of pairs is:

$$\sigma = \sqrt{\frac{E}{W}} \tag{2.25}$$

The FWHM of a Gaussian distribution is related to the standard deviation by $FWHM = 2\sqrt{2\ln 2}\sigma \approx 2.355\sigma$ and thus the energy dependence on the resolution can be:

$$FWHM \simeq 2.355\frac{\sqrt{\sigma}}{\sigma} = 2.355\sqrt{\frac{W}{E}} \tag{2.26}$$

Experience has shown that the energy resolution is better than the one calculated from Poisson distributions. This is because energy deposited by an incident particle is not a constant value as it was considered, and thus can fluctuate. The Fano Factor is introduced to give the experimentally observed variance and results from the energy loss in a collision not being purely statistical. Making the necessary modifications, eq. 2.26 is rewritten as:

$$FWHM = 2.355\sqrt{\frac{F\,W}{E}} \tag{2.27}$$

The Fano factor is an empirical value between $0 < F \leq 1$. If all the deposited energy is converted into electron-ion pairs, the process has no statistical fluctuations and $F = 0$.

In addition to the fluctuations in ionization, other mechanisms can also affect the energy resolution: random noise, fluctuations of the electric field, and fluctuations in the multiplication process for proportional counters.

**Spatial resolution**

The spatial resolution characteristic is key in detectors which the goal is to obtain the position of the incident radiation and/or to track the particle inside the detector's volume. These type of detectors are called position sensitive detectors (PSD). Single-wire proportional counters have many usages in detection and energy loss measures; however, determining of the position of the incident particle is limited by the physical size of the detector. For that purpose, a position sensitive detector is required. The multi-wire proportional chamber consists of a set of wires, which can be considered independent proportional counters; therefore, allowing to know the position where the radiation was detected.

The response of a position sensitive detector to an input point source is given by the point spread function (PSF). Considering a perfect punctiform beam entering the detector,

the detector's response is a Gaussian curve centered in the position of the incident beam (fig. 2.4). The FWHM of the point spread function is the spatial resolution of the detector.

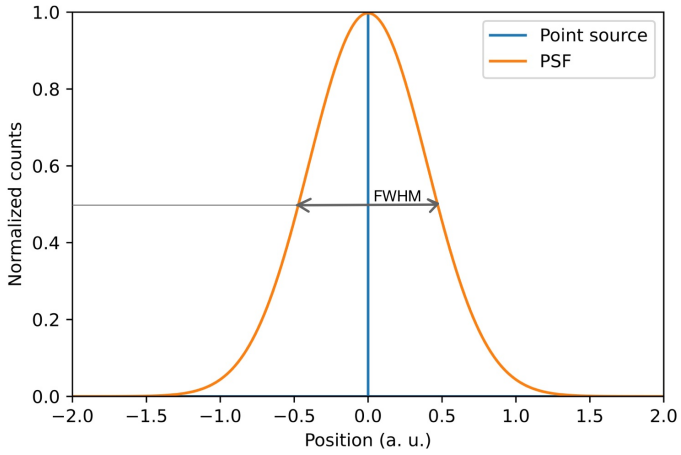


**Figure 2.4:** Point spread function of a perfect punctiform beam.

A real beam is not punctiform, but has a non-negligible width and a shape. In this case the reconstructed position distribution of every particle has a gaussian shape and the reconstructed position distribution of the beam is the convolution of the beam shape and the gaussian distribution [24].

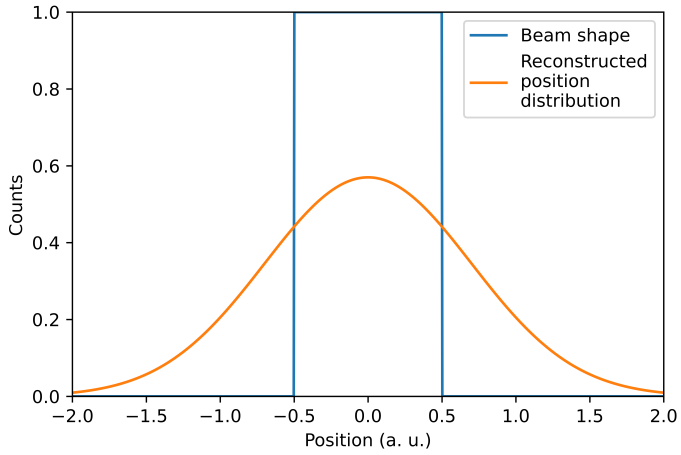


**Figure 2.5:** Reconstructed position distribution obtained from the convolution of the incident point source with the PSF of the detector.

The beam is narrower than the spatial resolution (fig. 2.5). In fact, the FWHM of the distributions do not depend significantly on the beam width. Fig. 2.6 shows the expected reconstructed position distribution with several beam width over spatial resolution ratios. The spatial resolution is the FWHM of the PSF.

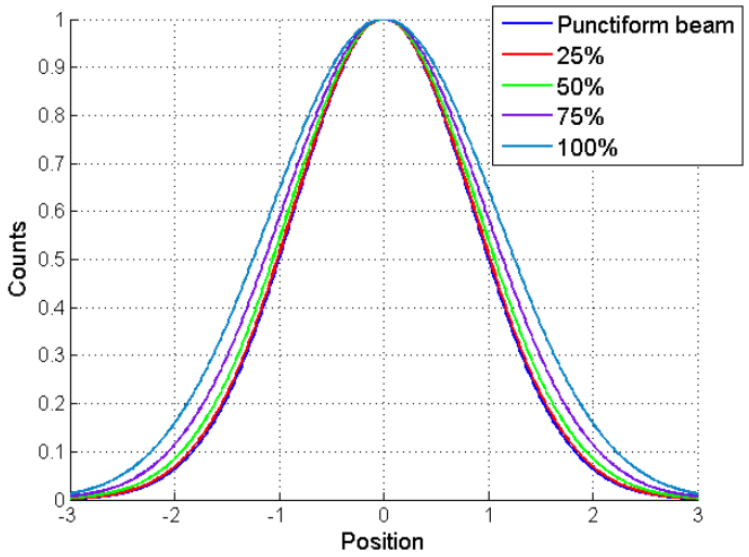


**Figure 2.6:** Reconstructed position distribution for several beam width over spatial resolution. Image from [24].

From fig. 2.6, the FWHM of the distributions does not depend significantly on the beam width.

### 2.3.6 Multi-wire proportional counters

The multi-wire proportional chambers (MWPC) consists of a set of thin, parallel and equally spaced anode wires. High voltage is normally applied to the wires (anode), and the conductive walls are at ground potential (cathode). The distance between the wires is limited to 1 or 2 *mm* for technical reasons. Each wire acts as a proportional counter and has an independent readout, meaning that the position where the particle was detected can be retrieved. The detectors geometry, electric field lines and equipotentials are represented in fig. 2.7.

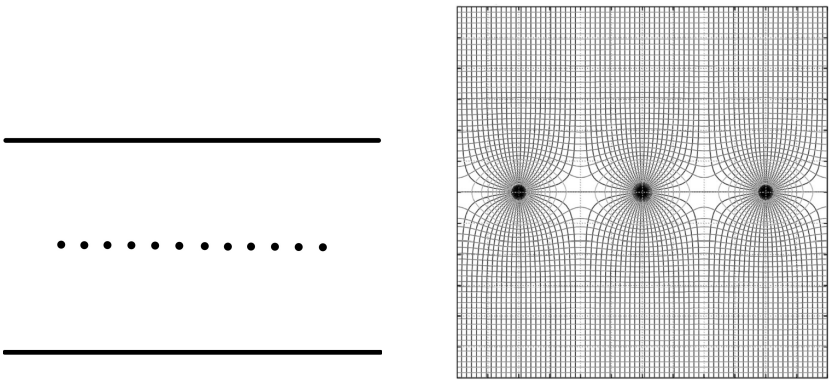

**(a)** MWPC geometry.

**(b)** Electric field and equipotential lines near the anode wires. Image from [22].

**Figure 2.7:** Geometry (a), electric field lines, and equipotentials lines (b) of a MWPC.

Electrons created by the ionization process drift towards the anode along the field lines; the avalanche occurs in the multiplication region near the wires. A large negative-polarity-induced pulse arises on the anode wire on which the avalanche is collected, while the neighboring anodes show smaller positive amplitude pulses [6]. Signal formation is faster in MWPC than for the proportional counter because the path of electrons and ions since their formation place until the anode (electrons) or the cathode (ions) is smaller; therefore, MWPC have a higher counting rate.

The resulting charges due to the particle passing in the gas are generally distributed over more than one anode. Being $d$ the distance between wires and $Q(x)$ the charge readout in the position $x$, the spatial resolution is the standard deviation and is given by:

$$\sigma^2 = \int Q(x)(x - \bar{x})^2 \, dx \Rightarrow \sigma = \frac{d}{\sqrt{12}} \tag{2.28}$$

The spatial resolution of a MWPC depends on the anode wire spacing. The worst possible situation for spatial resolution is when a particle is only detected in one single wire instead of on multiple wires.

The readout system can be configured into several different ways, but only two will be discussed in Chapter 5: each wire has its own individual readout system; or by a charge division chain. In the first, signals can be treated individually; however, this requires a preamplifier for each wire, increasing the complexity of the readout system. In the second method, the wires are interconnected by resistors to form a charge division chain. Two preamplifiers are used at both ends of the chain and the position of the particle is retrieved by identifying the centroid of the charge in the chain.

# Chapter 3

# State of the Art of Neutron Detectors

Neutrons have high applicability in different areas, such as particle physics, crystallography, archaeology, biology, medicine, and homeland security [3]. For this reason, new neutron detection techniques have been researched for the purpose of improving spatial resolution, detection efficiency, and high-rate capability. As a result of neutrons neutral charge, they have unique characteristics: lower interaction with matter and higher penetration power when compared with charged particles, but they are also more complex to detect. Since neutrons do not ionize atoms directly, they are detected indirectly upon producing a charged particle, which is then detected. The most common neutron-to-charged particle convertor is Helium-3; however, it is a very rare gas and has become particularly difficult to acquire. For that reason, there is an increasing need for the development of new detectors and techniques using alternative convertors. These detectors and techniques must also fulfill the requirements of state-of-the-art neutron sources, as the one under construction: European Spallation Source in Sweden.

## 3.1 $^3$He-crises

Helium-3 is a rare isotope on earth, which natural abundance is only 1.37 parts per million [25]; therefore, it is manufactured by nuclear decay of tritium, which is a radioactive isotope of hydrogen. The radioactive decay of tritium to helium-3 has a half-time of 12.3 years [26]:

$$^3H \rightarrow ^3 He + e^- + \overline{\nu} \tag{3.1}$$

Helium-3 is a noble, inert, nontoxic and nonradioactive gas. The main characteristics of $^3$He are its neutron absorption capability, its high neutron detection efficiency, and its good gamma-ray discrimination; then, it is widely used in scientific applications, namely in neutron detection. Other characteristic of $^3$He is its ability to detect neutron-emitting radioactive isotopes such as plutonium: a key ingredient in certain types of nuclear weapons.

The only method currently in use to produce $^3$He gas is collecting it as a byproduct of the manufacture and purification of tritium for use in nuclear weapons; therefore, the production of $^3$He gas depends on the manufacturing of nuclear weapons. The main two sources of $^3$He are the USA and Russia. With the end of the Cold War, the production of

nuclear weapons decreased and consequently the production of $^3$He gas. Although, despite the declining supply, it was enough to exceed consumption.

After the terrorist attacks of 9/11, the U.S. government installed radiation portal monitors (RPMs) with neutron detectors at ports and border crossings to control illicit transportation of nuclear and radiological material. RPM's are large area gaseous detectors filled with $^3$He with capability to detect gamma-rays, fast neutrons and thermal neutrons. Because of $^3$He application in homeland security, the consumption of $^3$He has risen rapidly and unprecedentedly since 2001.

Despite the high demand of $^3$He through the years, its production did not increase and thus it was not enough to exceed consumption. In 2009, it was recognized that the helium-3 stockpile could be exhausted and that the available supply might not meet future demand, starting the so called $^3$He-Crisis [27][28]. Fig. 3.1 represents the chronological evolution of $^3$He stockpile.

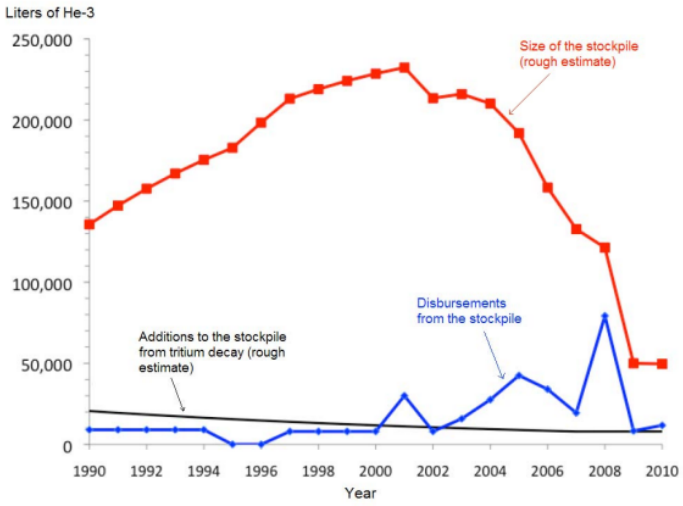


**Figure 3.1:** Chronological evolution of $^3$He from 1990 to 2010. Image from [27]

Table 3.1 shows the applications of $^3$He and their usage. The requested supply of $^3$He for Homeland Security is 84.5%.

| Application | % |
|---|---|
| Neutron detectors for security | 84.5% |
| Neutron-scattering | 10.0% |
| Oil & gas detectors | 2.5% |
| Medical imaging | 1.7% |
| Low-temperature physics | 1.3% |

**Table 3.1:** $^3$He different applications and their usage. Data from [29].

$^3$He-based detectors are since 1970s the golden standard for thermal neutron detection because of its detection efficiency, pulse resolution, gamma-ray rejection, physical robustness, and non-toxicity [30]. The $^3$He-Crisis calls into question these types of detectors: $^3$He prices skyrocketed and heavy restrictions in acquisition were implemented. As a result,

new technologies for neutron detection must be developed. Nonetheless, there is no immediate substitute for $^3$He with the same properties and specifications. For that reason, in the past decades R&D efforts have been in place to find equivalent and sustainable alternatives for helium-3 [31] [32] that must fulfill modern requirements of state of the art facilities, such as neutron spallation sources.

## 3.2 European Spallation Source

The European Spallation Source (ESS) is currently under construction in Lund, Sweden, and aspires to become the most powerful pulsed neutron beam. It will provide a neutron beam up to one hundred times brighter than currently available at any other facility [38] and a unique long pulse time structure of slow neutrons. Fig. 3.2 shows the comparison between ESS pulse brightness and other neutron facilities. The full blue represents the pulse brightness of the initial design [39] and the blue line the current design [40], possible through the optimization of the neutron moderation system. The red line is the ESS brightness for a 5 MW accelerator power.

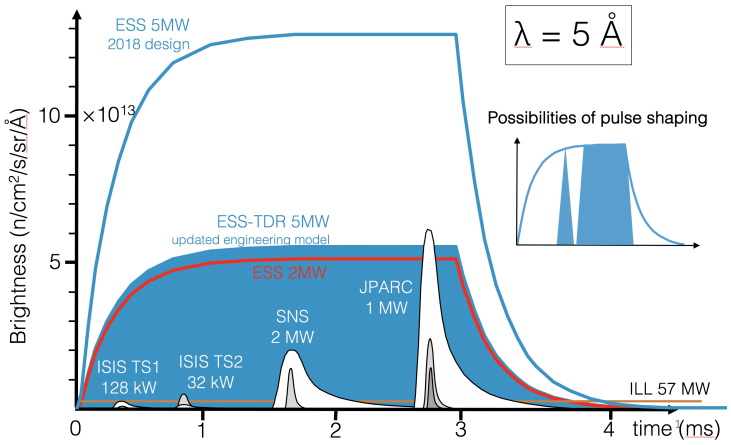


**Figure 3.2:** Single-pulse source brightness as a function of time at a wavelength of 5Å. Comparison between ESS, ISIS targets 1 and 2, SNS, J-PARC, and ILL. Image from [38].

This state-of-the-art facility requires state-of-the-art equipment, namely detectors with excellent detection efficiency, high-rate capability, and outstanding spatial resolution [40] [41] [42]. Because of the $^3$He-Crises, R&D programs have been created to develop large area and high-rate capability neutron detectors that can fulfill the requirements of the ESS with alternative convertors.

## 3.3 Gaseous neutron detectors

### 3.3.1 $^3$He proportional counter

The $^3$He proportional counter consists of a proportional counter filled with $^3$He gas. This gas is simultaneously the gas medium, where the ionization takes place, and the

conversion material, where the neutron is "converted" to charged particles. The principal characteristics of $^3$He proportional counters are its high detection efficiency and its good gamma-ray discrimination.

When a neutron enters the detector, it may interact with the $^3$He gas producing a trition and a proton with energies of 191 keV and 573 keV, respectively (reaction 2.11). Due to momentum and energy conservation, both secondary particles are emitted in opposite directions. Ideally both reaction products will travel in the gas medium, ionizing its molecules and depositing all their energy. In this case, the response of the detector will be a full energy deposition peak with a Gaussian shape centered at 764 keV (fig. 3.3 right); however, this is not accurate. Frequently the range of the secondary particles is larger than the dimensions of the detector, hence they may collide with the detector's wall (fig. 3.3 left: a and b). When this happens, the particle's energy is dissipated and does not contribute to the full energy peak, thus creating a low continuum of energies in the detector response (fig. 3.3 right). This is called the wall effect. By increasing the detector's dimensions or the gas pressure it is possible to reduce this effect.

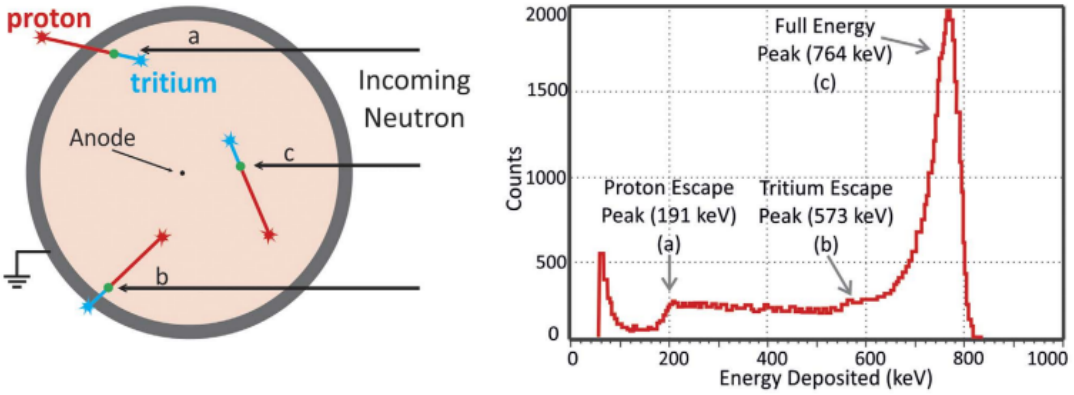


**Figure 3.3:** Left: three possible neutron interactions inside a $^3$He proportional counter (a, b, and c). From the interaction a trition (191 keV) and a proton (573 keV) are emitted. Right: pulse height distribution of a $^3$He proportional counter with interactions a, b, and c evidenced. Image from [43].

If the detector is large enough, the majority of the interactions will be like interaction *c* of fig. 3.3, where the reaction products are stopped inside the detector and deposited all their energy.

The efficiency of $^3$He proportional counters varies depending on volume and pressure; nonetheless, the detection efficiency can reach 80-90% for a typical pressure of 10 *bar* [17] [24].

Despite the high detection efficiency, and good gamma-ray discrimination, the $^3$He proportional counters are being replaced. Due to the $^3$He shortage, prices have heavily increased and availability has become limited, forcing scientists pursuing other alternatives. For the past decade, several efforts were made in founding a good replacement for $^3$He. Although the constant efforts, no other detector or technique have yet met the characteristics of the $^3$He proportional counter.

### 3.3.2 $BF_3$ proportional counter

The $BF_3$ detector is a proportional counter filled with Boron Trifluoride ($BF_3$) gas that is enriched to more than 90% of $^{10}B$ [4]. When a neutron interacts inside the detector, a $\alpha$-particle and a $^{7}Li$ ion are emitted (reactions 2.13 and 2.14). This gas is simultaneously the converter material and the detection medium. The detector has the same design and operation as the $^{3}He$ proportional counter, with a different gas medium.

The pulse height spectra of this detector is similar to the $^{3}He$ Proportional Counter (fig. 3.4). It shows two energy peaks corresponding to the Q-value of the two reactions of boron (reactions 2.13 and 2.14). The difference between the two is given by their probability ratio: 94% and 6%. The full energy peak is centered at 2.31 MeV corresponding to the 94%, where both $\alpha$-particle and $^{7}Li$ ion are fully stopped inside the detector. The wall effect is also demonstrated in this detector: when one of the reaction products collide with the detector wall, its energy is dissipated. The Lithium edge in fig. 3.4 represents the situation where the $\alpha$-particle strikes the wall and the $^{7}Li$ deposits all its energy in the gas (0.84 MeV). The Alpha edge is the reverse situation; the $^{7}Li$ collides with the wall and the $\alpha$-particle deposits all its energy (1.47 MeV).

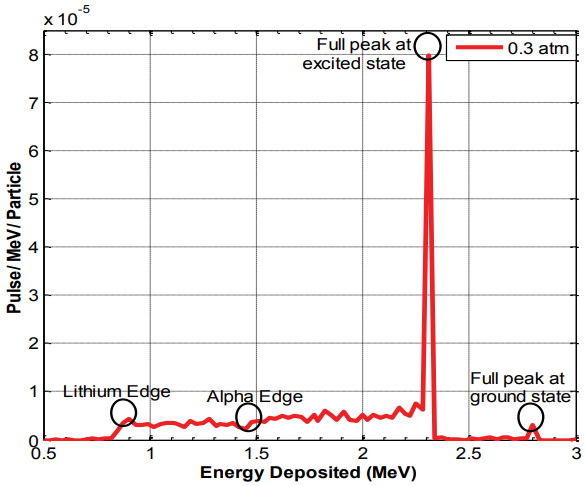


**Figure 3.4:** Pulse height distribution of a $BF_3$ proportional counter. Image from [45].

Compared to the $^{3}He$ PC pulse height spectra, the range of energies is higher because of the higher Q-values of the reactions. This characteristic provides a better gamma-ray discrimination; however, the detection efficiency of the $BF_3$ proportional counter is about 30-60% [17] [24] depending on the pressure.

The $BF_3$ gas is not an ideal working gas for proportional counters: it is toxic, corrosive, and slightly electronegative [18]. Consequently, $BF_3$ proportional counter is not a safe alternative for $^{3}He$-based detectors.

## 3.4 Boron-coated gaseous neutron detectors

To replace $^{3}He$ detectors it has been studied the use of $^{10}Boron$ as film converter based on gaseous detector. In this section several detectors who use a solid $^{10}B$ layer will be

explained; however, there are other neutron detection technologies.

### 3.4.1 Boron-lined proportional counter

The Boron-lined proportional counter consists on a conventional proportional counter with a solid layer of $^{10}$B acting as conversion material. This is the simplest gaseous neutron detector based on a solid boron converter. Unlike $^{3}$He or $BF_3$ proportional counters, the conversion material and the ionization gas are two separated materials: in the $^{3}$He or $BF_3$-based detector, the neutron interacts inside the gas volume, whereas in the boron-lined PC it interacts inside the boron layer (fig. 3.5 left). An advantage is the liberty to choose any type of gas for charge multiplication convenient for the detector's purpose.

When an incident neutron interacts with an atom of $^{10}$B, an $\alpha$-particle and a $^{7}$Li ion are produced. Due to momentum and energy conservation, the particles are emitted in the same line but in opposite directions. The boron layer, where the neutron interaction occurs, is located on the detector wall. This means that when an interaction occurs at least one of reaction products will be absorbed either in the converter or in the wall; the other particle enters the detector and deposits its energy, although, because it had to travel through some thickness of coating, the particle's energy is a fraction of its initial energy. Fig. 3.5 left (b) represents this situation and right the pulse height spectra of the detector. It is also possible that, despite an interaction event, the neutron cannot be detected: if the reaction products are emitted aligned in respect to the detector wall they will not enter the detection medium, or if the particle that should enter does not have sufficient energy to escape the boron layer.

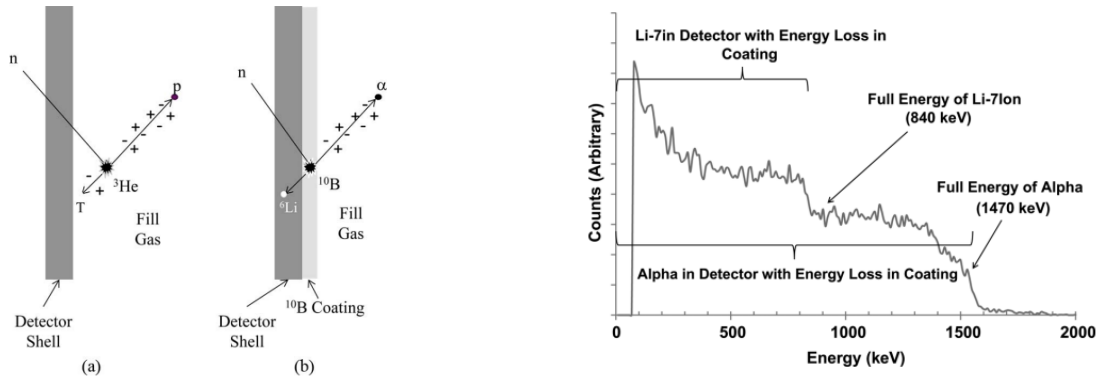


**Figure 3.5:** Left: (a) $^{3}$He proportional counter; (b) Boron-lined proportional counter. Right: pulse height spectra of the Boron-lined proportional counter. Images from [46].

The spectrum (fig. 3.5 right) exhibits the wall effect. This compromises the detection efficiency of the detector and its gamma-ray discrimination.

The neutron-to-charged particle conversion occurs in the $^{10}$B layer. The thickness of the layer is a decisive factor for neutron detection and detection efficiency. On the one hand, if it is too thick the secondary particles may not be able to escape the layer. On the other hand, if it is too thin the incident neutron may not interact with the $^{10}$B. Fig. 3.6 shows the detector efficiency as a function of the thickness of the boron coating.

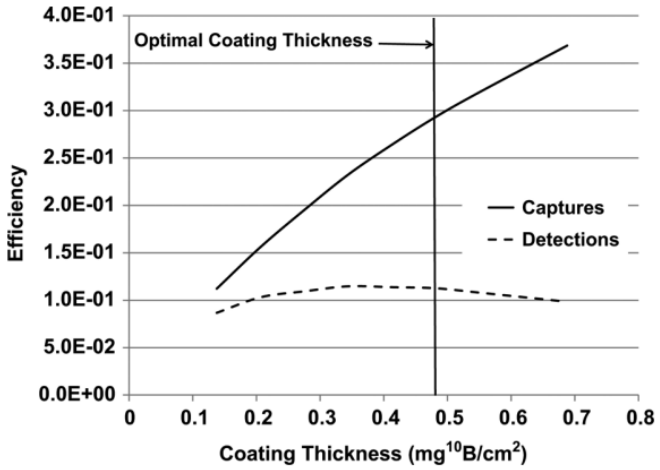


**Figure 3.6:** Simulation-based modeling of the relationship between coating thickness, thermal neutron capture efficiency, and detection efficiency for an individual Boron-lined proportional counter. Image from [46].

The vertical line in fig. 3.6 represents the optimal coating thickness. The detection efficiency of a single Boron-lined proportional counter is approximately 12% (using $^{10}$B enriched boron), assuming detection on both $^{10}$B layers that the neutron must traverse. This value significantly lower than $^{3}$He proportional counters.

### 3.4.2 Boron-coated straws

One possible solution to increase the detection efficiency in boron based neutron detectors is to have multiple Boron-lined proportional counters: the Boron-coated straws are an array of smaller diameter Boron-lined PC (fig. 3.7). This detector is a low-cost technology based on long copper tubes (straws), coated on the inside with a thin layer of $^{10}$B-enriched boron carbide ($^{10}B_4C$) [47].

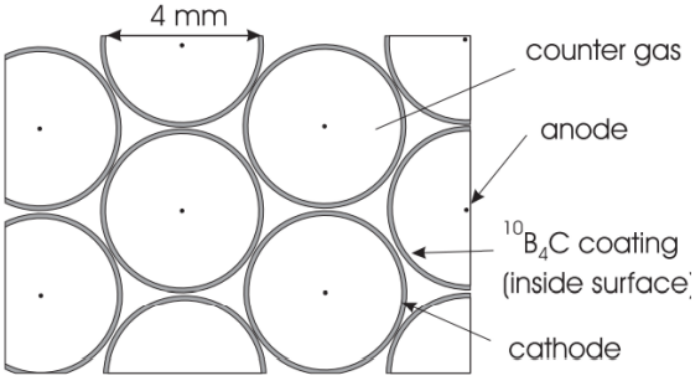


**Figure 3.7:** Geometry of the Boron-coated straws detector. Image from [48].

The Boron-coated straws detector was first designed for high rate imaging applications [48]; however, because of the $^{3}$He-Crisis, it was optimized for homeland security applications to act as RPM's [49]. The technology was modified to increase the boron-coated area

in order to achieve the best detection efficiency. The straw-tube design was replaced by a star-shape straw for that purpose. Fig. 3.8 shows two star shapes (center and right).

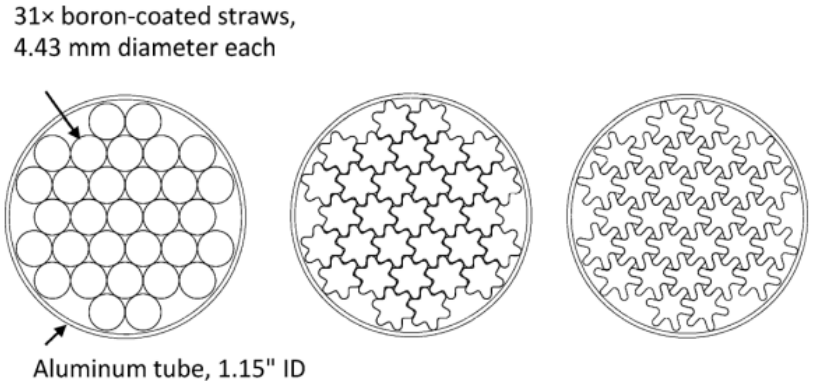


**Figure 3.8:** Left: array of 31 boron-coated straws housed inside a 2.92 cm tube. Center and right: design variations with star shaped straws referred to as Star1 (center) and Star2 (right). Image from [50].

Monte Carlo simulations were performed to determine the optimal coating thickness that represents the maximum detection efficiency. The maximum detection efficiency was obtained with the Star 2 detector, yielding 50.9% for thermal neutrons with a 1.28 $\mu m$ coating. Star 1 detector showed an efficiency of 42.1% for a 1.49 $\mu m$ coating, and the tube-shaped achieved the lowest efficiency of 36.5% efficiency with a 1.63 $\mu m$ coating [50]. A Star1 prototype was built with 31 straws and a 0.85 $\mu m$ thick of $^{10}B_4C$.

The straw neutron detector offers a cost effective solution that has proven itself compatible with robust and stable operation in field applications. High levels of gamma rejection, matching or exceeding those achieved with $^3He$, are provided by a simple threshold cut [50]. This detector is available commercially by Proportional technologies, Inc. [51].

### 3.4.3 Multi-grid detector

Analogous to the Boron-coated straws, the multi-grid detector also consists on multiple individual detectors; however, arranged in a different geometry. The Multi-Grid is a large area gaseous detector. It was projected to be composed by eight square tubes filled with gas where each tube has stacked 128 electrically insulated grids. One single grid is represented in fig. 3.9 left. Each grid has a series of short and long blades parallel and orthogonal to the entrance window, respectively, dividing the grid into cells. Anode wires go through the length of the columns formed by each cell (fig. 3.9 right). The studied model consists of 96 grids, 60 anode wires and has an active area of $200 \times 200\ cm^2$. The short blades in each grid are coated with 1 $\mu m$ thick layer of $^{10}B_4C$.

The Multi-Grid detector was tested on a monoenergetic neutron beam with an intensity of $10^6\ n/cm^2$ at the CT2 test instrument at ILL (Institut Laue-Langevin). The measured detection efficiency was 47.9% at a wavelength of $2.52 \times 10^{-10}\ m$. The incident particle position is determined by the cell in which the event is detected, and thus the spatial resolution is a detection-cell dimension ($4 \times 2.35 \times 1\ cm$) [52] [53] [54].

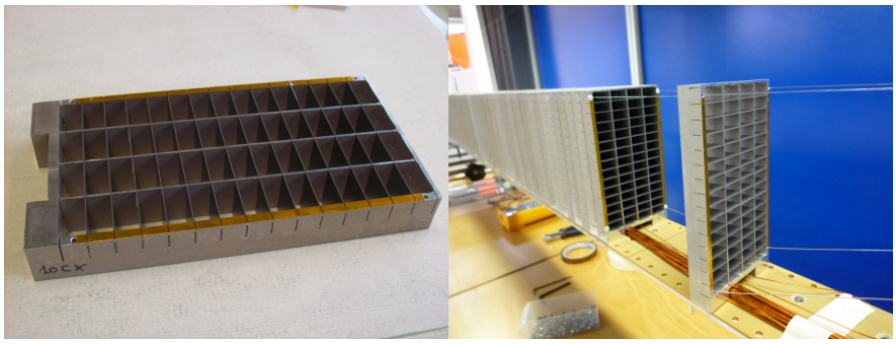

**Figure 3.9:** Left: one grid of the multi-grid detector. Right: one tube with 128 grids. Image from [53].

### 3.4.4 GEM-based detectors

To accomplish the ESS requirements it is essential to develop neutron detectors with high-rate performance, high detection efficiency and excellent spatial resolution such as gas electron multiplier (GEM) [55] [56]. The GEM detector consists of a polymer foil coated with electrodes on both sides and pierced with a high density of holes immersed in a suitable gas medium. A potential difference is applied between the two sides of the foil creating an electric field. Primary electrons released by the radiation interaction with the gas molecules drift towards the holes where the electric field is high enough to trigger the electron multiplication process (fig. 3.10). The produced electrons are then collected in an electrode [57]. This detector is used for charged particles; however, by adding a "converter" such as a boron layer it is possible to detect thermal neutrons.

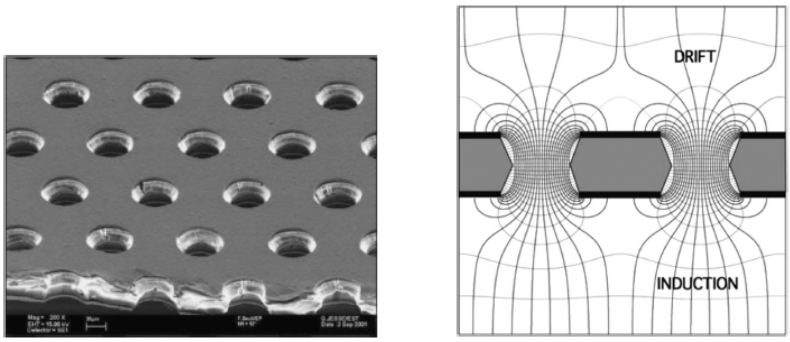


**(a)** Holes in a GEM foil

**(b)** Electric field in the region of the holes

**Figure 3.10:** GEM geometry (a) and electric field inside and near the holes (b). Image from [57].

#### BAND-GEM technology

The boron array neutron detector (BAND-GEM) consists of a triple GEM detector and a 3D-converter cathode that is made of 24 aluminium grids insulated between each other and coated with 0.59 $\mu m$ of $^{10}B_4C$ [58]. The 2D position of the incident neutron is reconstructed through a padded anode composed of 128 pads with different dimensions ($4 \times 3\, mm, 4 \times$

6 $mm, 4 \times 12\ mm$) (fig. 3.11). The detector has an active area of $5 \times 10\ cm^2$. The whole detector can be tilted at an angle $\theta$ with respect to the incoming beam, increasing the conversion probability by $1/sen(\theta)$ and consequently enhancing the detection efficiency. The BAND-GEM detector working principle and a photography of a detector padded anode are presented in fig. 3.11. This detector was tested on the EMMA instrument at ISIS. The measured efficiency of the BAND-GEM detector was 40% at a wavelength of $4 \times 10^{-10}\ m$ and a tilted angle of $\theta = 5°$. The measured spatial resolution was 7 $mm$ at the same conditions. The relative charge extraction efficiency of the 3D converter was 67%.

A similar detector, which converter grids were coated with 1 $\mu m$ of $^{10}B_4C$, was tested at the ORPHEE reactor [59]. The count-rate measured was about 8 $MHz/cm^2$ with a non-linearity value of 55%, or 2 $MHz/cm^2$ with a non-linearity value of 11%.

Although the BAND-GEM rate capability is higher than the $^3$He tubes ($\sim$ 100 $kHz/tube$), its detection efficiency is lower: $^3$He tubes have a detection efficiency of about 80%. Nevertheless, the count-rate is sufficient to satisfy the requirements of the ESS and thus is a good candidate to replace $^3$He-based detectors.

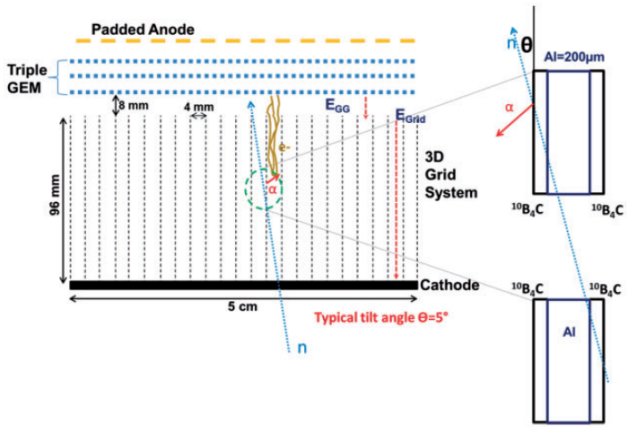


**(a)** BAND-GEM detector working principle. Image from [58].

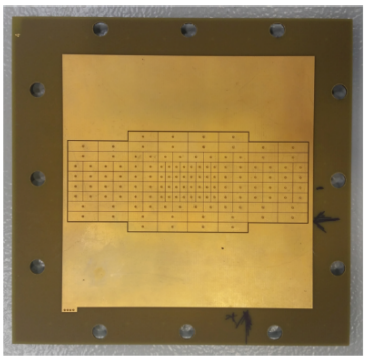

**(b)** Padded anode of the BAND-GEM detector. Image from [59].

**Figure 3.11:** The BAND-GEM technology: working principle and anode.

### THGEM

The thick gas electron multiplier (THGEM) has a hole-structure similar to the GEM, but with 10-fold expanded dimensions. It is manufactured by standard PCB techniques of drilling holes in G10 and cooper etching [60]. The THGEM is an interesting detector due to its simplicity, robustness, and is economic when compared to GEM.

In order to have a neutron detector, a thin $^{10}B_4C$ layer is coupled to two thick gas electron multiplier (THGEM) [61]. The incident neutrons are localized by the position-sensitive charge readout. The $^{10}B_4C$ layer has a thickness of 1 $\mu m$ and an active area of $10 \times 10\ cm^2$. This detector was tested with cold neutrons at the ICON facility at SINQ (PSI). The measured intrinsic neutron detection efficiency was around 5%. The spatial resolution of the THGEM is 1.32 $mm$ for the x-coordinate and 1.38 $mm$ for the y-coordinate.

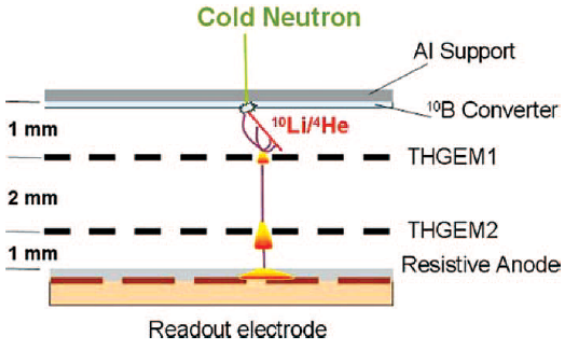


**Figure 3.12:** The THGEM detector working principle. Image from [61].

The THGEM is a good solution because of its simplicity and low-cost solution for large area. The THGEM has a high counting rate capability in the *MHz* range [60], thus it can be used in pulsed neutron sources.

### GEM-based neutron detector

The GEM-based neutron detector consists of a stack of boron-coated cathodes, BGEMs and Gain-GEMs [62]. From top to middle there is a sequence of a boron-coated cathode to neutron-to-charged particle conversion, four BGEMs, a Gain-GEM to amplify the signal, and a double-sided flexible readout board (fig. 3.13). In this readout board, cross-strips were put in opposite surfaces to obtain the 2D position of neutrons. The detector is symmetrical and has in total 10 boron layers with 1.2 $\mu m$ thick each. In the BGEM, the cathode is composed of a 400 $\mu m$ thick Aluminium layer covered by a 1 $\mu m$ thick $B_4C$ coating for neutron detection [63].

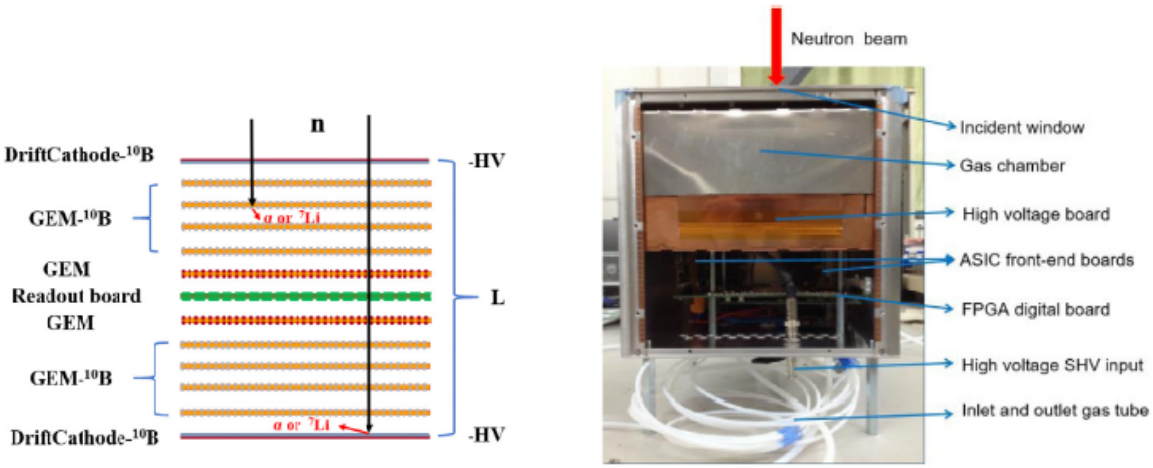


**(a)** The detector working principle. **(b)** A photograph of the physical detector.

**Figure 3.13:** GEM-based neutron detector: working principle and physical detector. Image from [62].

The detector was tested on a monoenergetic neutron beam at the Triple-axis Spectrome-

ter of CMRR and a test beamline of CSNS. The detector's sensitive area was $200 \times 200\ cm^2$, its detection efficiency was 54% at a wavelength of $4.9 \times 10^{-10}\ m$, and its spatial resolution is $2.94\ mm$ (FWHM). This detector has an overall detection efficiency identical to a conventional $^3$He neutron detector. Its high-rate capability must yet be studied; however, the GEM-based neutron detector is apparently a notable alternative to $^3$He-based detectors.

# Chapter 4

# The coincidence detector

The main concern of the state of the art neutron detectors is that it is impossible to reconstruct the line of action of the conversion reaction and to collect its total released energy. When a neutron interacts with a boron atom the charged particles ($\alpha$ and $^{7}$Li) are emitted in opposite directions. Because of the range of the secondary particles in $^{10}$B, the layer's thickness, and the detectors geometry, one of the emitted particles (at best) cannot reach the gas and thus cannot be detected. As a result, part of the neutron capture information is lost. To collect all information, it is necessary to detect the two secondary particles. The solution is to optimize the B-coating thickness. This technique will be discussed in this chapter.

## 4.1 Limitations of boron-coated gaseous neutron detectors

Boron-coated gaseous neutron detectors have a solid $^{10}$B layer deposited in a substrate where the neutron capture reaction occurs; the resulting charged particles interact in the gas and thus are detected. When a neutron interacts with a boron atom, an $\alpha$-particle and a $^{7}$Li ion are emitted in-line in opposite directions (reactions 2.13 and 2.14). Geometrically only one of the reactions products enters the gas, while the other is absorbed by the boron layer or the substrate. Because of this, part of neutron capture information is lost, namely its released energy.

Increasing the boron layer thickness will increase the probability for a neutron to interact with a boron atom, hence the neutron detection efficiency also increases; however, only to a certain point. Because the range of the secondary particles is only a few microns in solids, if the boron layer is too thick, they will not escape the boron layer avoiding detection. To study the effect of the $^{10}$B converter thickness on the detection efficiency two modes are considered: backscattering and transmission.

Fig. 4.1 represents the backscattering and the transmission modes, and its corresponding detection efficiency. The maximum detection efficiency is approximately 4.5% for a $B_4C$ coating thickness of 3 $\mu m$ in backscattering mode.

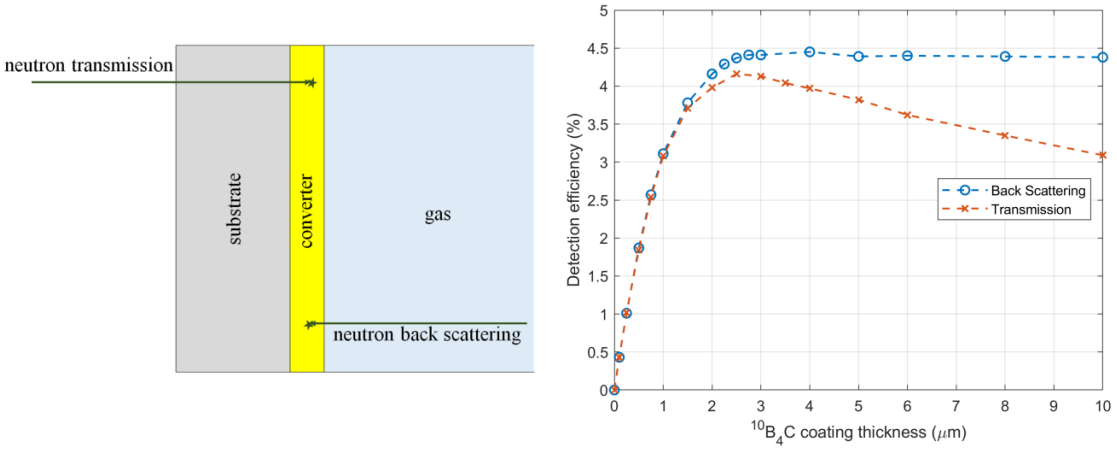


**Figure 4.1:** Left: layout of neutron interactions in transmission and backscattering modes. Right: detection efficiency as a function of the $B_4C$ (99% $^{10}B$ enriched) thickness, for a neutron beam in transmission and backscattering mode, obtained by GEANT4 simulations. The boron layer is deposited on a 0.5 *mm* thick aluminium foil. Detector physical volume was a box with a volume of $10 \times 5 \times 2.5$ $cm^3$, filled with Ar:$CO_2$ (90:10) at 1 atm. Image from [64] and [65].

The goal of the novel detector presented in this thesis is to improve spatial resolution by optimizing the boron thickness for it to be smaller than the range of the alpha and the $^7$Li ion; therefore, both charged particles can escape the conversion layer, reach the gas with enough energy, and be detected.

## 4.2 Operating principle and geometry

The novel technique consists on a neutron detection with a thin $^{10}B$ layer deposited on an equally thin substrate allowing both secondary particles to escape the solid layer with sufficient energy to be detected. Two independent readout systems are placed in opposite sides of the detection layer to simultaneously detect the track of each reaction products (fig. 4.2 left).

The converter foils consists on two $B_4C$ layers (0.5 $\mu m$ each) deposited on both sides of a mylar foil with a thickness of 0.9 $\mu m$ [64] [65] (fig. 4.2 right). The two readout systems (detector A and B) can be considered two independent MWPCs. Each readout is on each side of the converter foil in order to detect the secondary particles emitted back-to-back. Both secondary particle tracks can be reconstructed along the x-coordinate and thus the neutron incident position can be inferred. In the example present in fig. 4.2, detector A detects the $\alpha$-particle in a range between 0 *mm* and 4 *mm*, and detector B the $^7$Li ion in a range between -2 *mm* and 0 *mm*. Because each detector is composed of discrete wires, this means that several of them would be triggered. Considering a single independent readout, the neutron capture position will lay inside the respective ranges; however, by combining the information of both detectors, this value will be much closer to the real value (0 *mm*), as shown by fig. 4.2 left.

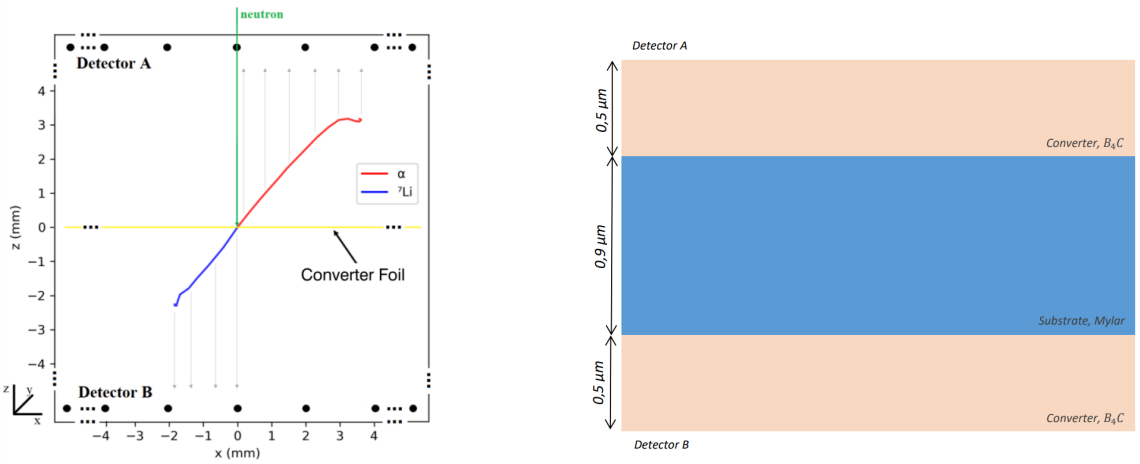


**Figure 4.2:** Left: Scheme of the neutron coincidence detector. Simulation of a neutron interacting with a conversion foil, in which both secondary particles leave long tracks in the gas. Two MWPCs representing the two independent readout systems (detectors A and B). Image from [64] and [65]. Right: Symmetric converter coating layout made of two $B_4C$ layers (0.5 $\mu m$ each) deposited on both sides of a mylar foil (0.9 $\mu m$).

The neutron interaction position estimation depends on the collected charge by each wire, which in terms depends on the energy deposited by each particle in the gas along their track. The deposited energy depends on the particle's initial energy when it escapes the boron layer. This technique makes use of the information available in the neutron capture reaction by collecting the energy and track position of both secondary particles instead of only one.

## 4.3 Materials

The material choice will influence the performance of the detector. In this section three material categories will be discussed: neutron converter, substrate, and filling gas. The reasons behind each selection will also be detailed.

### Neutron converter

The neutron conversion material is based on Boron-10. In the present detector, the chosen conversion material was $^{10}B_4C$ [64].

The neutron capture probability for thermal neutrons at low solid thickness is better for $^{10}$B-based substrates than for $^{6}$Li; the range of the neutron capture reaction products is also better for $^{10}$B [64], hence the $^{10}$B reaction is selected for neutron-to-charge-particle conversion. It can be used in their elemental form: $^{10}$B; or as compounds: $B_4C$ (boron carbide), and BN (boron nitride). The elemental form of boron has bad oxidation resistance and poor electrical conductivity [66]; therefore, it is not the best option to use as a cathode nor as deposited on a substrate. The boron nitride is widely used in semiconductor neutron detectors [67]; however, it has not been used in gaseous neutron detectors. Finally, boron carbide is the most stable compound of boron. It has excellent thermal stability and

chemical resistance, better conductivity than the elemental boron [66], and is not damaged by radiation [68]. For these reasons, $B_4C$ is the selected neutron converter.

### Substrate

For the substrate, three types of materials were considered: aluminium (Al), mylar ($C_{10}H_8O_4$), and kapton ($C_{22}H_{10}N_2O_5$). The chosen substrate must be transparent to neutrons, have low density, have the mechanical capability to go through the deposition process without suffering deformations, and be available in thin films. Aluminium is the common choice for $B_4C$ deposition in neutron detectors because of its transparency to neutrons and the mechanical capabilities to endure the deposition process; however, its density is higher than for mylar or kapton.

Despite the theoretical assumptions, the availability of thin films is the most critical factor and thus the decisive one. Kapton foils bellow 1 $\mu m$ thickness were not found, and aluminium foils were very fragile and difficult to manipulate. The mylar foils were the less challenging because of its superior elasticity and robustness [64].

Depositing thin Boron thicknesses on a thin Mylar substrate requires complex techniques, such as DC-magnetron suttering [69][70], room temperature pulsed laser deposition [71][72], or a method of dripping the solution containing $B_4C$ nano-particles [73]. Currently two converter foils are physicalyl available for testing. A 1 $\mu m$ thick boron foil in the form of a 1 cm diameter, which is commercially available, and a $100 \times 100$ $mm^2$ mylar foil with 0.5 $\mu m$ thickness coated by a 0.5 $\mu m$ enriched $B_4C$ on both sides.

### Filling gas

As seen in Section 2.3.2, the filling gas must be a mixture of a noble and a quenching gas. The quenching gases are normally $CH_4$ (methane) or $CO_2$ (carbon dioxide). Hydrogen has the highest neutron scattering cross section, hence a collision between a neutron and a hydrogen will deflect the first of its original path. Consequently, the detection efficiency will decrease or an uncertainty will be added to the position determination. This scattering process cannot be ignore, thus the quenching gas choice must fall on $CO_2$. For the purpose of this thesis, the filling gas is Ar:$CO_2$ (90:10) at atmospheric pressure.

# Chapter 5

# Simulation setup

From the interaction between a neutron and a boron atom results two charged particles: alpha and Lithium-7 (reactions 2.13 and 2.14). These charged particles, when traversing the detector produce ionization patterns. The primary ionization data is obtained from GEANT4 simulation [64].

In this chapter it will be discussed the software and processes used in simulating electron and ion transport, induced current in the readout system, and spacial resolution of the detector. The detector operation principle and geometry is the same discussed in Chapter 4.

## 5.1 Garfield ++

The main software used for the simulation of the detector was Garfield++. It is a toolkit for the detailed simulation of signals in particle detectors based on ionization measurement in gases or semiconductors [74]. An interface to the Magboltz program [75][76] is used to calculate the transport properties of electrons in gas mixtures. For visualization purposes, such as plotting the drift lines, and making contour plots of the potential, different classes in Garfield++ are available; they depend on the ROOT framework [77].

### 5.1.1 Flow of the simulation process

To describe gaseous media, the *MediumMagboltz* is implemented. This class calculates transport properties, interpolates gas tables, and imports and stores gas files. For calculating the electric field inside the detector, the class *ComponentAnalyticField* is used; it can handle two-dimensional sets of wires and planes. The elements which define the geometry of the detector (planes and wires) are added in this class. This class also allows the calculation of the induced signal in the wires of the readout system. The object *sensor* acts as an interface between *ComponentAnalyticField* and transport classes.

The electron avalanche calculation is done either by Runge-Kutta-Fehlberg integration - class *DriftLineRKF* - or by Monte Carlo integration - class *AvalancheMC* or *AvalancheMicroscopic*. The latter provides the most detailed and accurate result; however, because this class follows electrons from collision to collision, it requires the most computation time. This

class only covers electrons; for tracking ions, a secondary avalanche class must be added. The chosen avalanche class for the simulation was *DriftLineRKF*, explained latter in this chapter.

As the information about charged particles (e.g., alpha and lithium-7) crossing the detector is provided by GEANT4 simulations [64], there is no need to simulate ionization patterns produced by them; however, it could be done by classes of type Track: *TrackHeed* or *SRIM*. Garfield++ uses as input the primary ionization information to launch at the indicated position an electron with the respective energy and direction of movement provided.

Fig. 5.1 shows the interplay between classes and the flow of Garfield++ simulation. As output, Garfield gives data files and designs graphics with the help of ROOT.

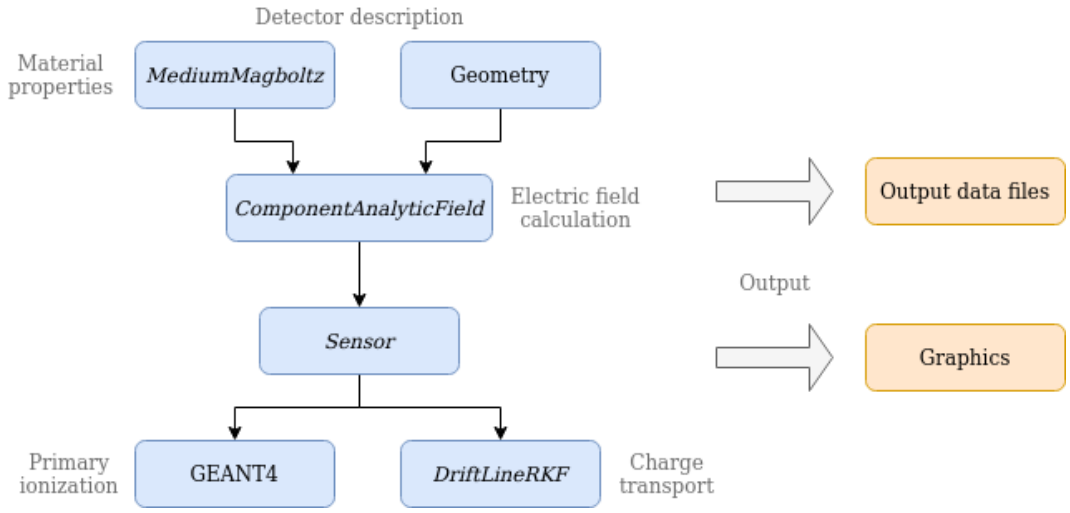


**Figure 5.1:** Flow of the simulation process and classes' interplay.

### 5.1.2 The coincidence detector in the simulation

#### General considerations

The GEANT4 simulations were performed with a perpendicularly incident infinitely collimated thermal neutron beam at (x,y) coordinates (0,0). The total number of incident neutrons was $10^6$. Considering a symmetric 1 $\mu m$ $^{10}B_4C$ coating in a 0.9 $\mu m$ mylar, the detection efficiency of the coincidence detector was 1.39% [64]. For input to the Garfield++ simulations a pre-selection of events was done, being one event a neutron that interacts with the Boron-10 producing two charged particles that escape the boron layer and the substrate interacting in the respective detector. The selection consisted on choosing events in which:

- there is coincidence in detectors A and B from the same event, i.e., the same incident neutron;
- the energy of the $\alpha$-particle and the $^7$Li is more than the threshold energy of 100 keV;
- the particle has some movement after each interaction with the gas molecules until full energy deposition.

The threshold energy of 100 keV is for gamma-ray discrimination. A particle from a selected event is called an eligible particle. The coincidence detector detection efficiency is now 1.33%.

In a single event, two eligible particles are originated ($\alpha$-particle and Lithium-7): one interact in detector A and the other in detector B. This is due to the fact that they are emitted in the same line of action, but with opposite directions. In each interaction with the gas particles, the eligible particle has a determined energy that decreases along their track. This decreasing amount in each interaction can be roughly considered as the deposited energy. The number of electron-ion pairs formed in each interaction is given by $E_{deposited}/W$. For Ar the W-value is 26 eV (table 2.4). If for any case the deposited energy was less than 26 eV, the considered value was the latter. The electron formed in an interaction has an energy equal to the ionization potential: 15.8 eV (table 2.4).

### Geometry

To perform the simulations a determined geometry was considered. Fig. 4.2 is a very good representation. The detector is symmetrical; therefore, both detector A and B are equal, inverted in the y-axis. The geometrical considerations are: the distance between the wires is 2 $mm$; the wire radius is 25 $\mu m$; the distance between the boron plane and the wires is 8 $mm$; and the distance between the wires and the cathode plane is 2.5 $mm$. Fig. 5.2 is a geometrical representation of the detector.

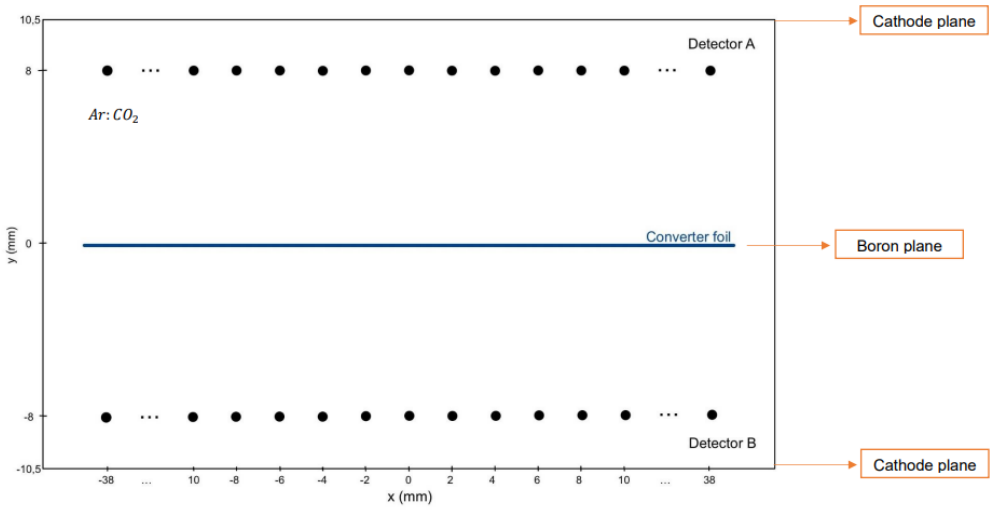


**Figure 5.2:** Geometrical scheme of the coincidence detector.

The detector prototype has 39 wires in each readout system. For the purpose of reducing the computational time and resources, only 11 wires in each detector A and B were simulated. From the GEANT4 simulations, the distance travelled by an eligible particle in the x-projection is less than 8 $mm$; therefore, 11 wires (10 $mm$) are sufficient to perform the simulations.

### 5.1.3 Gas mixture, and ion mobility

Magboltz interface calculates the transport properties of electrons drifting in gas mixtures under the influence of electric and magnetic fields by using semi-classical Monte Carlo simulation [76]. Through *MediumMagboltz* it is possible to specify gas composition, temperature, and pressure, and to create a gas file. The chosen gas mixture for this simulation is the same used in the GEANT4 simulations: 90% Ar and 10% $CO_2$ [64]. The gas file contains the transport properties of the gas for electrons and a table that stores the rates calculated by Magboltz of excitation and ionization levels.

For tracking ions a ion-mobility file is required and must be entered manually. For the purpose of this simulation, the ion-mobility file corresponds to a table of reduced electric fields and their corresponding reduced ion mobility of Ar+ in pure Ar. The ion mobility ($K$) depends on the drift velocity ($V_{drift}$) and drift field ($E_{drift}$):

$$K = \frac{V_{drift}}{E_{drift}} \tag{5.1}$$

The reduced ion mobility of $Ar^+$ in pure Ar as a function of reduced electric field is presented in fig. 5.3. Because there is no current data in literature for drift in the Ar mixture, this value is an approximation.

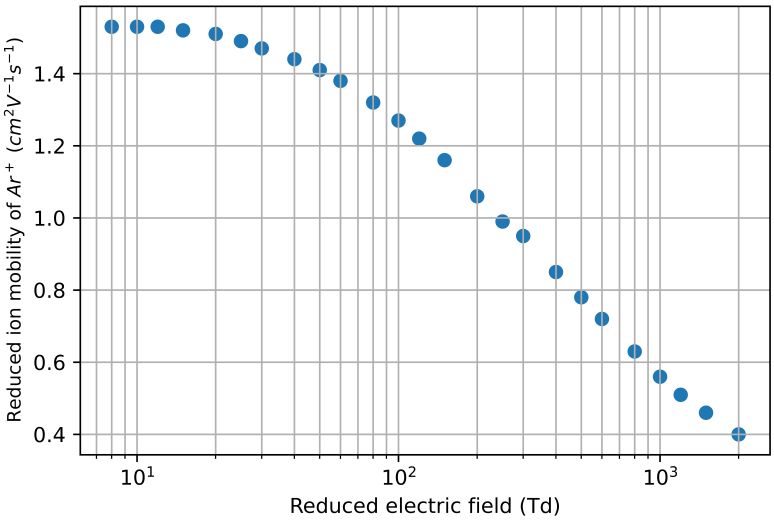


**Figure 5.3:** Reduced mobility of $Ar^+$ in pure Ar as a function of reduced electric field. Data from [74]. The horizontal axis is in logarithmic scale.

### 5.1.4 Electron and ion transport

The role of GEANT4 is to simulate the passage of the secondary charged particles of neutrons reaction with Boron-10 through both detectors, giving the required information of primary ionizations. The GEANT4 simulations were previously done [64]. The avalanche process is calculated through the following methods:

- Monte Carlo integration: *AvalancheMicroscopic* class covers microscopic tracking of electrons, which are followed from collision to collision. It requires a table of collision rates for each scattering process as a function of electron energy, provided by the class *MediumMagboltz*. Ions, on the other hand, cannot be tracked microscopically in Garfield++ using this class and consequently are tracked macroscopically by a secondary class: *AvalancheMC* or *DriftLineRKF*. To simulate the drift lines of ions it is required the macroscopic drift velocity as a function of the electric field provided by a ion-mobility file. This is a very thorough technique, which consumes an enormous amount of time and computational resources due to the dimensions of the detector and the number of primary ionizations. *AvalancheMC* also uses Monte Carlo integration for avalanche calculation. The difference between both classes relies on the time interval, the distance, and the collision rate between each collision. In *AvalancheMC* the user must specify one value of the three: time steps, distance steps, or collision rate. In the first case the integration is done using fixed time steps, in the second case using fixed distance steps, and in the third the class is instructed to do the integration with exponentially distributed time steps with a mean equal to a multiple of the collision time. This is a more simpler calculation compared to *AvalancheMicroscopic*; however, not so accurate in the microscopic level and for detailed calculation of ionization and excitation processes.

- Runge-Kutta-Fehlberg integration: *DriftLineRKF* (RKF) method gives the average expected path for a single electron drifting from a certain point in the detector and allows a relatively quick assessment of the general drift characteristics of a particular geometry as compared to performing a full Monte Carlo simulation [78]. With this technique it is also possible to simulate ions avalanche. RKF is suitable for tracking electrons over large distances and in cases where detailed calculations of ionization and excitation processes are not required, such as this one. Thus, this is the chosen method for avalanche calculation.

Primary electrons move towards the wires and make an avalanche in their proximity. Primary electrons located in detector A go to the respective wires in the same detector, and equally for detector B. In the ionization process many electron-ion pairs are created. The number of electrons at the end of the drift line is thus given by [74]:

$$n_e = exp(\int (\alpha - \eta)\, ds) \tag{5.2}$$

Since $exp(\int \alpha\, ds)$ is the multiplication factor, $exp(\int \eta\, ds)$ is the loss factor, $\alpha$ the Townsend coefficient, and $\eta$ the attachment coefficient.

Ions start going to the drift region. They go in the direction of the boron layer or the down and up plane when in detector B or A, accordingly. An example of the avalanche process can be seen in fig. 5.4, where the drift paths of the electrons and ions are shown with the orange and red lines, respectively. The calculation was performed on Garfield++. The electron drift lines were calculated using the *AvalancheMicroscopic* class in order to have a detailed description of the drift; for the ion drift lines, the *AvalancheMC* was used. In both cases, the track of the $\alpha$-particle and the $^7$Li ion is considered a straight line simulating an ideal track.

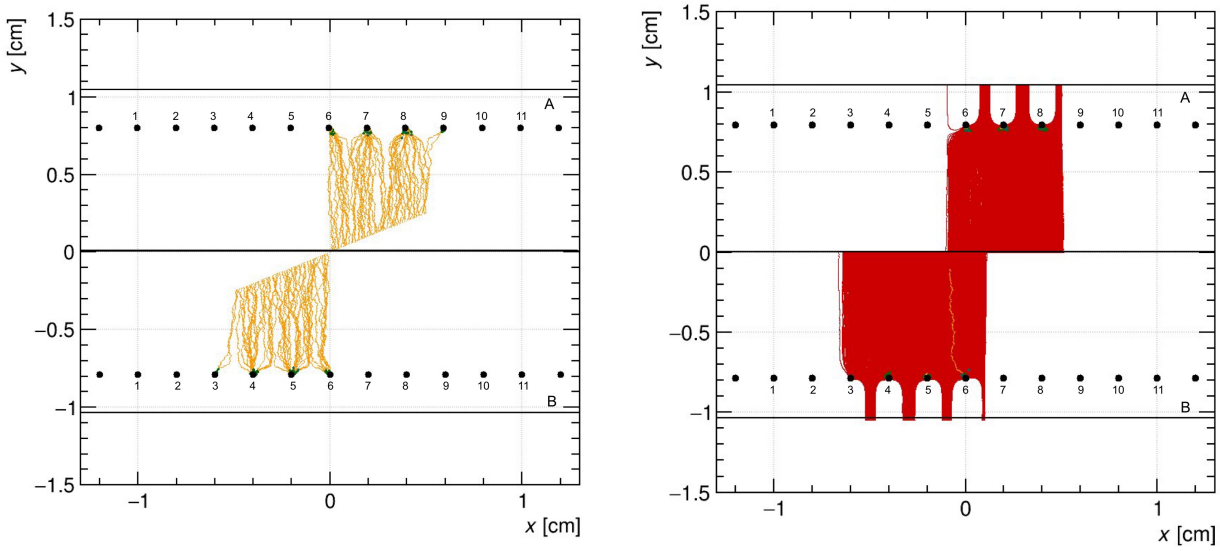


**Figure 5.4:** Electrons (left) and ions (right) drift lines using the classes *AvalancheMicroscopic* for electron drift lines and *AvalancheMC* for ion drift lines. An ideal alpha and lithium track was used.

In fig. 5.4 left, it is observed that the majority of the electrons drift towards the nearest wires (in this case, wires 3, 4, 5, 6 of detector B, and 6, 7, 8, 9 of detector A). Although, some may drift to the neighbour wires (1 and 2 of detector B and 10 and 11 of detector A). It is predictable that the induced current in the nearest wires will be negative and higher in absolute than the furthest ones. Because the ion drift lines are not calculated interaction by interaction, they are not so detailed (5.4 right) due to the class used. The green spots signal the excitation processes near the wires where the field is higher.

## 5.2 Gain

To optimize the applied voltage in the wires and in the boron plane in order to maximize the multiplication factor, gain curves were performed. The simulations accounted for the real number of wires: 39 wires in each detector. Changing the number of wires translates to a change in the electric field map. In this case, the gain should be as truthful as it could be, so the real number of wires were used. The *DriftLineRKF* class was used, and the gain is given by the multiplication factor [74]:

$$M = exp(\int \alpha \, ds) \tag{5.3}$$

Two cases of gain dependence were study: changing the applied voltage in the wires and in the boron plane, and changing electron's initial position along x and y-coordinates. In both cases, one initial electron was launched in each respective position with an energy equal to the ionization potential, 15.8 eV.

### Gain dependence on the applied voltages

The initial electron was launched from the position were $x = 0\,cm$ and $y = -0.3\,cm$. Two situations were studied: (1) varying the applied voltage in the wires between 1500V and 4000V, and fixing the boron plane voltage at 1000V and the cathode voltage at 0V; (2) varying the applied voltage in the boron plane between 200V and 2000V, and fixing the wire voltage at 3000V and the cathode voltage at 0V.

The gain calculated for the situation (1) is represented in fig. 5.5.

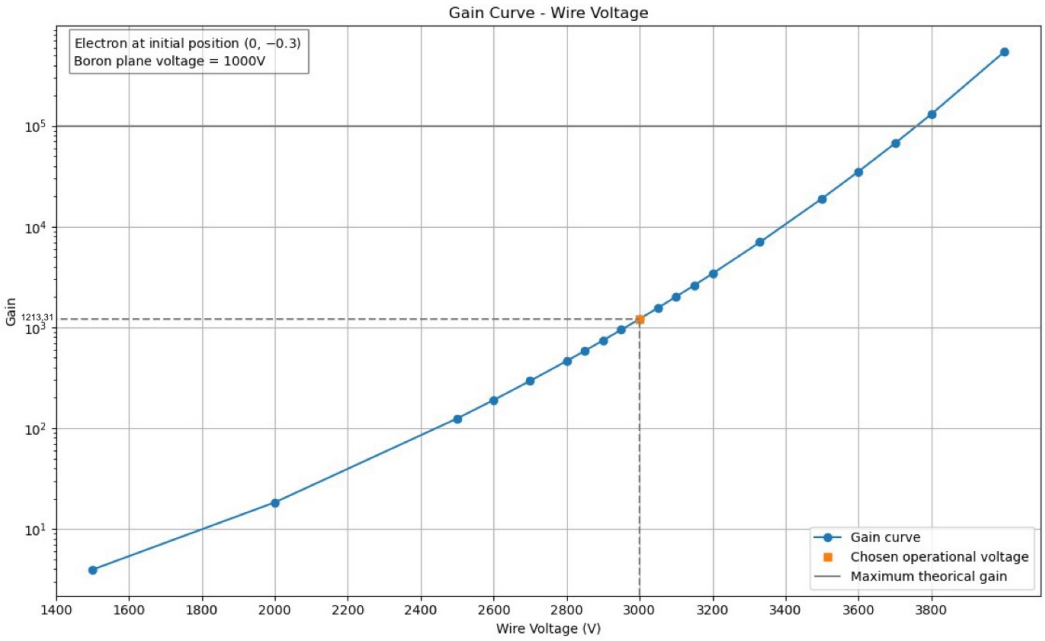


**Figure 5.5:** Gain curve calculated by varying the wire voltage between 1500V and 4000V (1). Simulations performed with 39 wires in each detector, boron plane voltage of 1000V, and cathode voltage of 0V; the position of the initial electron is (0 cm;-0.3 cm). The maximum theoretical gain corresponds to $10^5$ [6] above which the detector breaks down with continuous discharges. The chosen operational voltage is 3000V.

As expected, the gain increases with the applied voltage; however, voltages of more than 3000V are difficult to maintain without considerable electronic noise. For this reason, the ideal operational wire voltage is 3000V, corresponding to a gain of 1213.31.

Increasing the applied voltage in the boron plane while the wire voltage is 3000V, decreases the potential differential between the boron plane and the wires. As a result, the gain decreases with the voltage increase in the boron plane.

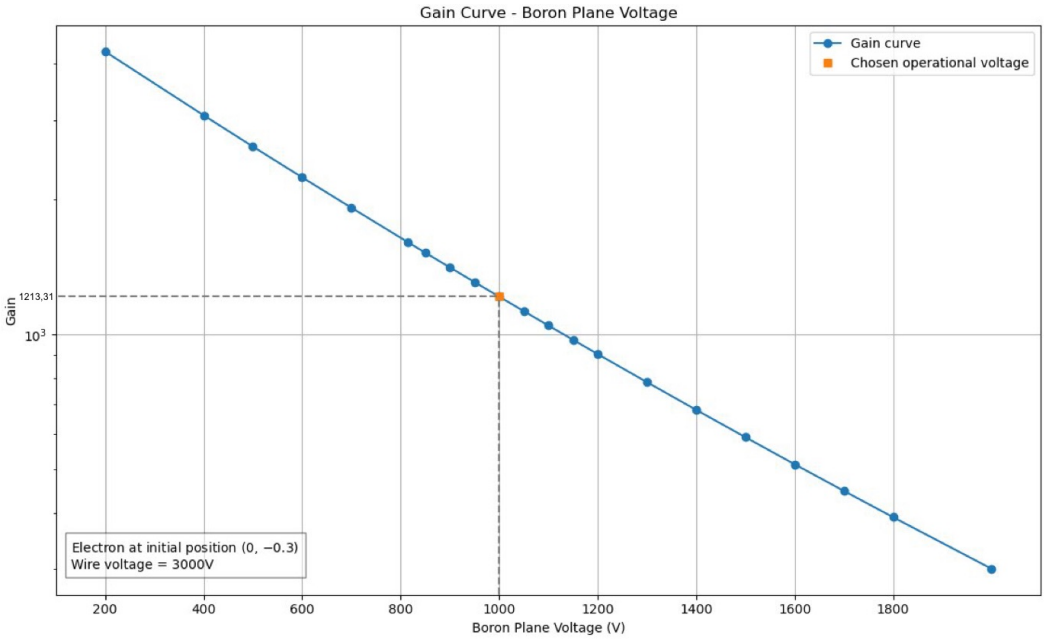


**Figure 5.6:** Gain curve calculated by varying the boron plane voltage between 200V and 2000V (2). Simulations performed with 39 wires in each detector, and wire voltage of 3000V; the position of the initial electron is (0 cm;-0.3 cm). The chosen operational voltage is 1000V.

To achieve the best multiplication factor, higher voltages must be applied, i.e., higher potential differences between the wires and the boron. Although, this leads to an increase in the electronic noise to major levels that directly affect the detector's performance. The choice must then be balanced between maximizing the gain and minimizing the noise.

After careful consideration, the selected voltages are:

| Wire voltage (V) | Boron plane voltage (V) | Cathode voltage (V) | Gain |
|---|---|---|---|
| 3000 | 1000 | 0 | 1213.31 |

**Table 5.1:** Selected wire, boron plane, and cathode voltages for a gain of 1213.31.

These are the voltages used in the next Garfield++ simulations.

### Gain dependence on the electron initial position

After the selection of the applied voltages, the variation of the multiplication factor depending on the electron initial position is studied. Also two situations were considered: (3) varying the x-coordinate between -2 cm and 2 cm at 0.1 cm intervals, and fixing the y-coordinate at -0.3 cm; (4) varying the y-coordinate between -0.1 cm and -0.7 cm at 0.1 cm intervals, and fixing the x-coordinate at 0 cm.

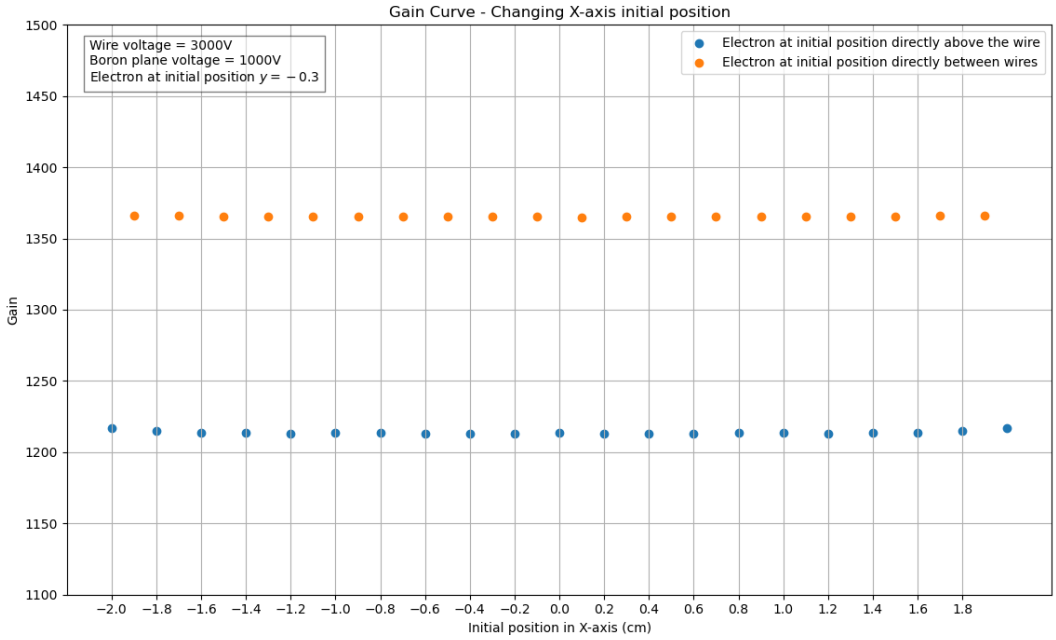


**Figure 5.7:** Gain curve calculated by varying the x-coordinate between -2 cm and 2 cm at 0,1 cm intervals (3). Simulations performed with 39 wires in each detector, wire voltage of 3000V, and boron plane voltage of 1000V; the y position of the initial electron is -0.3 cm.

The distance between the wires is 0.2 cm, then at 0.1 cm intervals some points will fall right above the wires and others between then. Because the electric field is assumed to be different in the direction above the wire and between two wires, the gain should also be different. The electric field will be studied in the Section 5.3. In this case, when the electron is launched in the direction above a wire (blue), the gain is 1213.31; when it is launched in the direction between two wires (orange), the gain is 1365.26. The relative error between the two gains is 11.1%.

In situation (4), varying the y-coordinate, translates to a minimal change in the multiplication factor that is difficult to observe in fig. 5.8. For that reason, the gain along the y-coordinate in both detectors is considered to be constant.

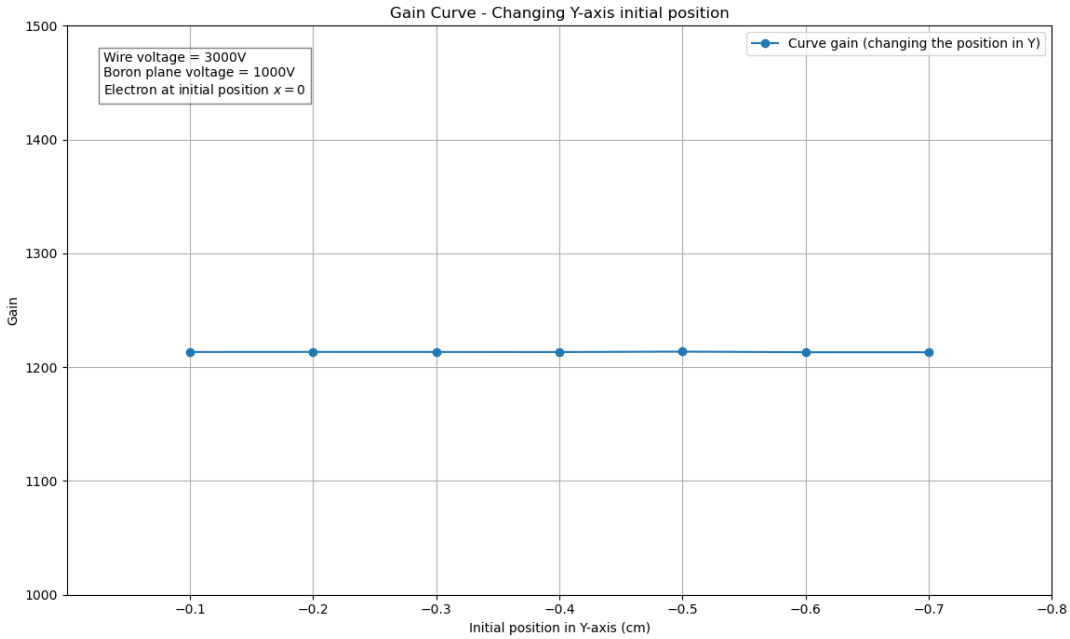


**Figure 5.8:** Gain curve calculated by varying the y-coordinate between -0.1 cm and -0.7 cm (4). Simulations performed with 39 wires in each detector, wire voltage of 3000V, and boron plane voltage of 1000V; the x position of the initial electron is 0 cm.

## 5.3 Electric field

As seen above, the electric field is critical to a good detector performance; therefore, it will be studied in this section. Although it is possible to calculate the electric field with Garfield++ and represent it with the help of ROOT, the calculations were done outside of these programs. To design the detectors geometry and meshing the *Salome* [79] program was used; to perform the electric field calculations the *Elmer FEM* [80] program was also used. The electric field lines are presented next (fig. 5.9).

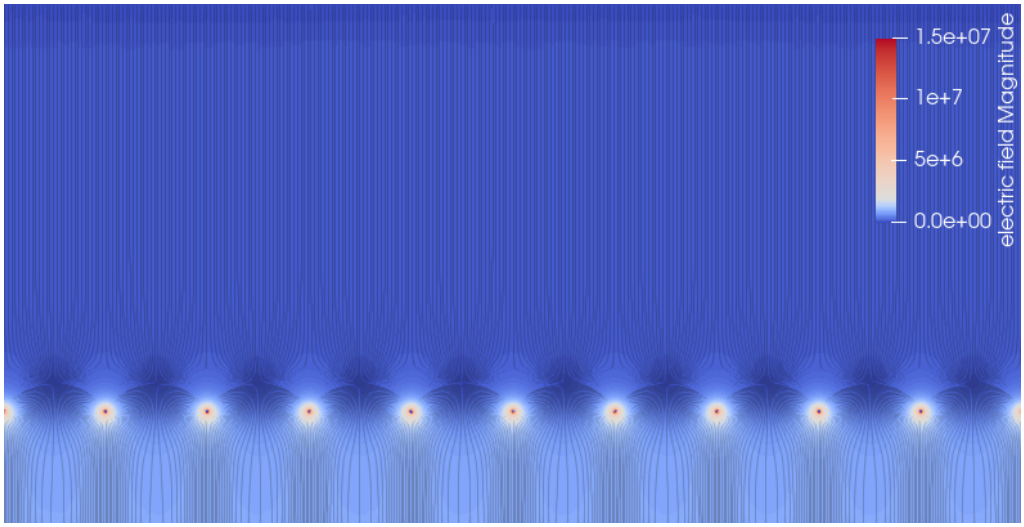


**Figure 5.9:** Electric field lines for 11 wires in detector B. The electric field magnitude is evaluated through a colour scale.

The electric field lines are represented only for 11 wires in the detector B; however, since the coincidence detector is symmetric, it is equal for detector A (inverted in the y-axis). The electric field lines have the same behaviour for the other wires, except for the outer ones. Near the wires the electric field has its maximum value. Analytically, the electric field close to a long line of charge can be obtained using a Gauss' law and is given by:

$$E = \frac{\lambda}{2\pi r \varepsilon_0} \tag{5.4}$$

$\lambda$ is the charge per unit length. The smaller the dimensions of the wire, the higher the electric field close to it will be. The reduced electric field value near the wires presented in this section is smaller than the real one due to the impossibility of the programs to represent infinite spaces. The Elmer electric field calculation is limited by the mesh size. Moreover, its size near the wires was chosen to have the same magnitude as the distance between consecutive collisions. In the region between the wires and the cathode plane the field is more intense than in the region between the wires and the boron plane due to the distance between both.

The electric field was studied in detail for the operational voltages used in the simulation (table 5.1). In the following figures, several configurations were used to determine the reduced electric field value plotted over a line.

**Straight line from the boron plane to the wire**

The first configuration is the reduced electric field plotted over a straight line from the boron plane to the wire, as it is indicated in fig. 5.10 above.

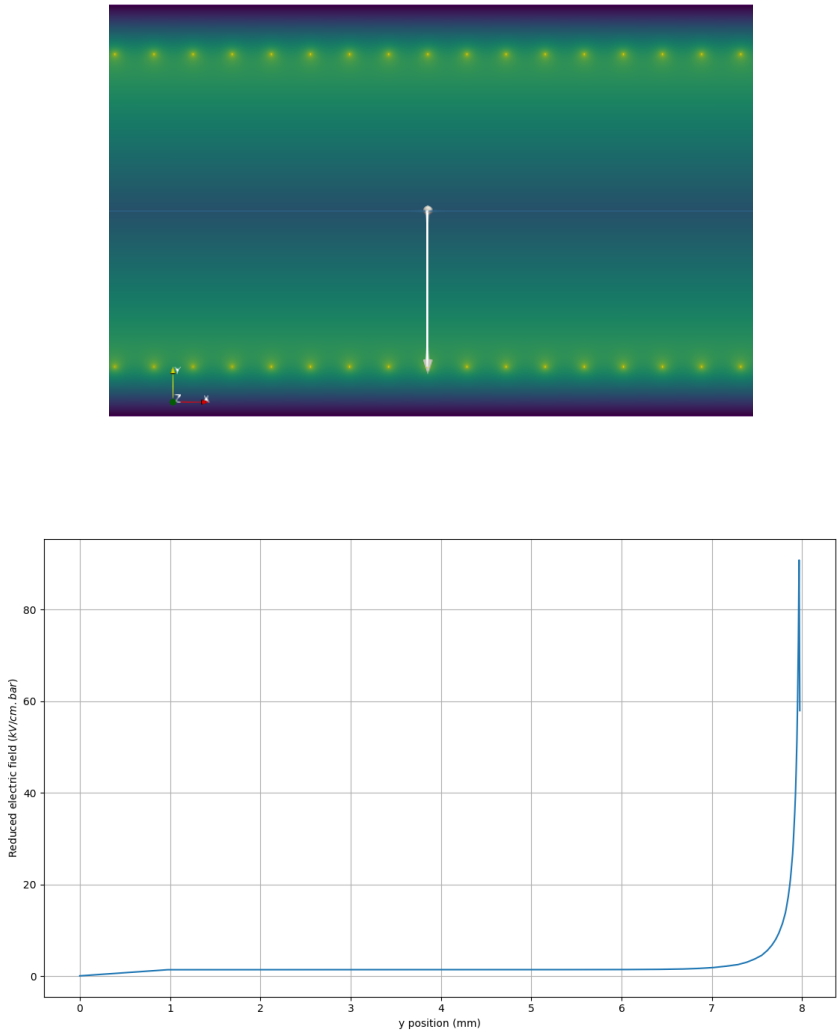


**Figure 5.10:** Above: geometrical representation of the line in the detector. Below: reduced electric field ($kVcm^{-1}\,bar^{-1}$) over a straight line from the boron plane ($y = 0\ mm$) to a wire ($y = 8\ mm$) at atmospheric pressure.

The reduced electric field is zero when $y = 0\ mm$ because it represents the boron plane. In the region between the boron plane and the wire, the electric field is constant. Closer to the wire, it increases exponentially. In the region near the wire, the electric field is maximum; however, fig. 5.10 below does not represents that due to software limitations.

Charged particles that are formed in the boron plane drift towards the wires. The drift region is from $y = 0\ mm$ to $y \approx 7\ mm$ (fig. 5.10 below). The multiplication process occurs near the wires where the reduced electric field is high enough to surpass the ionization potential; therefore, the multiplication region is from $y \approx 7\ mm$ to $y \approx 8\ mm$ (fig. 5.10 below).

**Straight line from the cathode plane in detector B to the cathode plane in detector A between wires**

The second configuration is the reduced electric field plotted over a straight line from the cathode plane in detector B to the cathode plane in detector A passing between the wires (fig. 5.11 above).

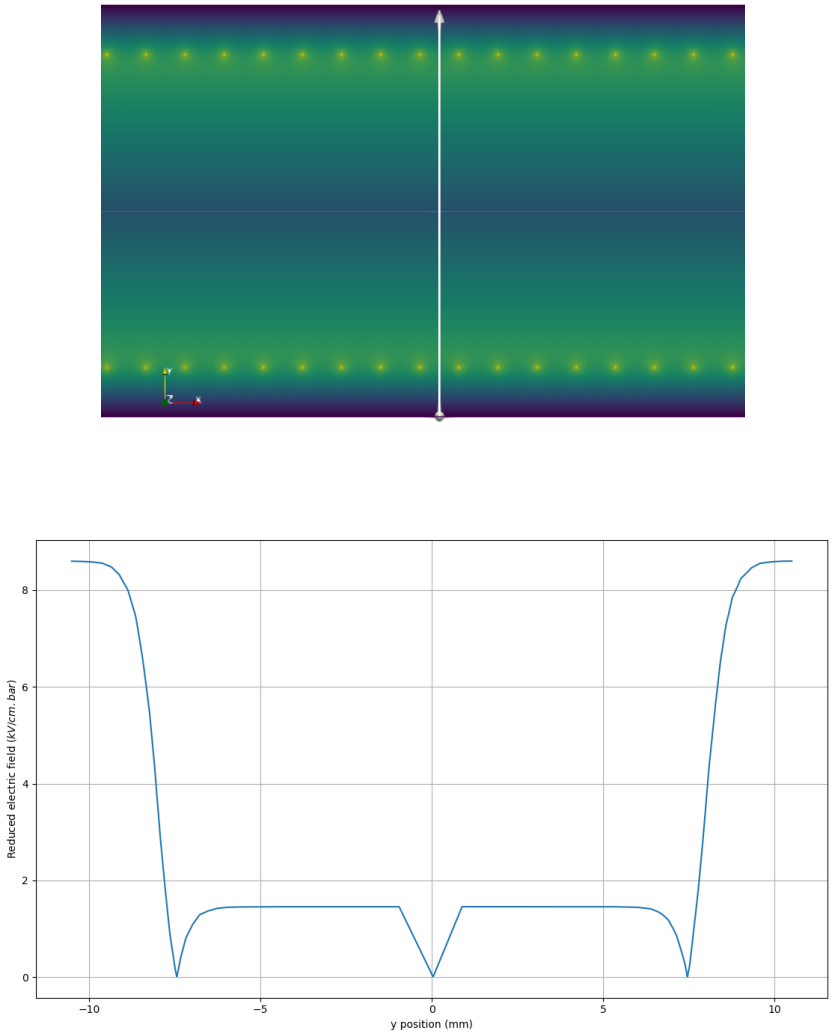


**Figure 5.11:** Above: geometrical representation of the line in the detector. Below: reduced electric field ($kVcm^{-1}\,bar^{-1}$) over a straight line from the cathode plane in detector B ($y = -10.5\ mm$) to the cathode plane in detector A ($y = 10.5\ mm$) passing between the wires at atmospheric pressure.

Fig. 5.11 below shows three points where the reduced electric field is approximately zero: the boron plane at $y = 0\ mm$, where there is no reduced electric field inside it, and at $y \approx -7.5\ mm$ and $y \approx 7.5\ mm$ because of the minimum value that it has in this area (fig. 5.9). As expected the reduced electric field is constant between the boron plane and the wires. It is also constant near the cathode planes at $y = -10.5\ mm$ and $y = 10.5\ mm$. Additionally, the reduced electric field is more intense in the latter region (fig. 5.9).

**Straight line from the cathode plane in detector B to the cathode plane in detector A above the wires**

The third configuration is similar to the second: instead of passing between wires, the line passes through the wires (5.12 above). The reduced electric field is plotted over a straight line from the cathode plane in detector B to the cathode plane in detector A passing above the wires.

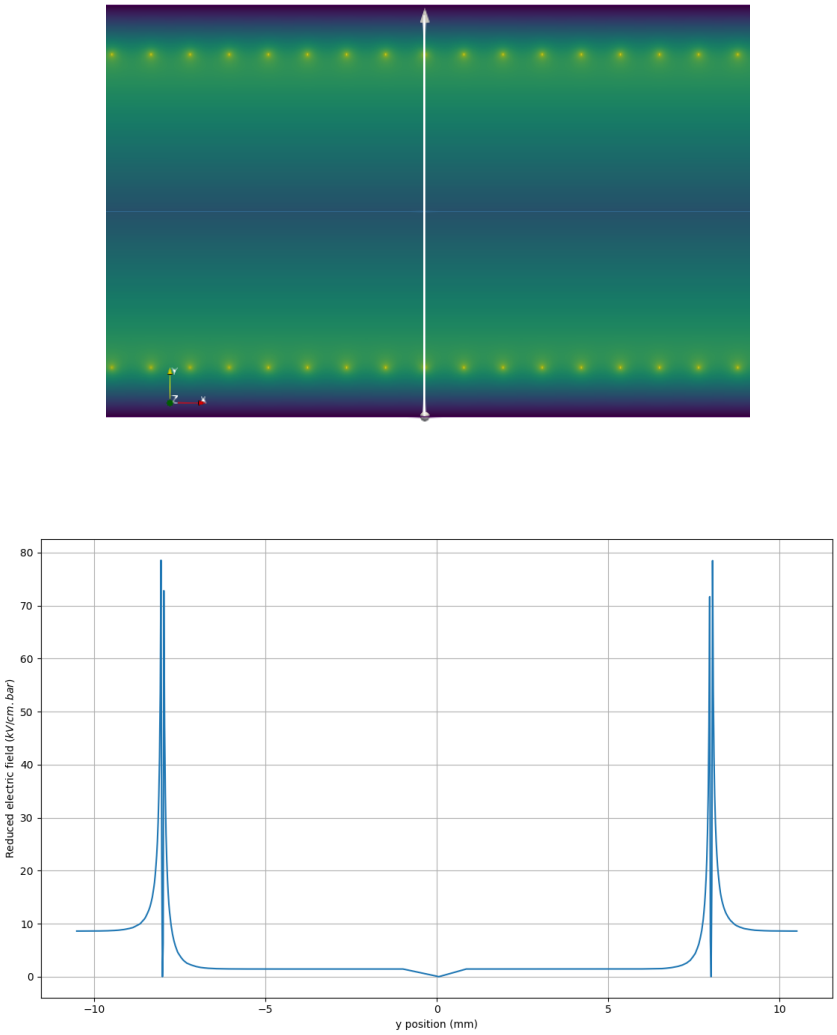


**Figure 5.12:** Above: geometrical representation of the line in the detector. Below: reduced electric field ($kVcm^{-1}\,bar^{-1}$) over a straight line from the cathode plane in detector B ($y = -10.5\ mm$) to the cathode plane in detector A ($y = 10.5\ mm$) passing above the wires at atmospheric pressure.

In fig. 5.12 below there is also three points where the electric field is zero: the wires are at $y = -8\ mm$ and $y = 8\ mm$, and the boron plane at $y = 0\ mm$. Inside these materials there is no electric field and thus it is zero. Compared to fig. 5.11 below, the electric field is also constant near the cathode planes and between the boron plane and the wires. Additionally, it is lower in the latter region. The reduced electric field near the wires in fig. 5.12 below is not the real value due to the reason explained early.

**Straight line from one wire to the consecutive other**

The fourth and last configuration is the reduced electric field plotted over a straight line from one wire to the consecutive other (fig. 5.13 above).

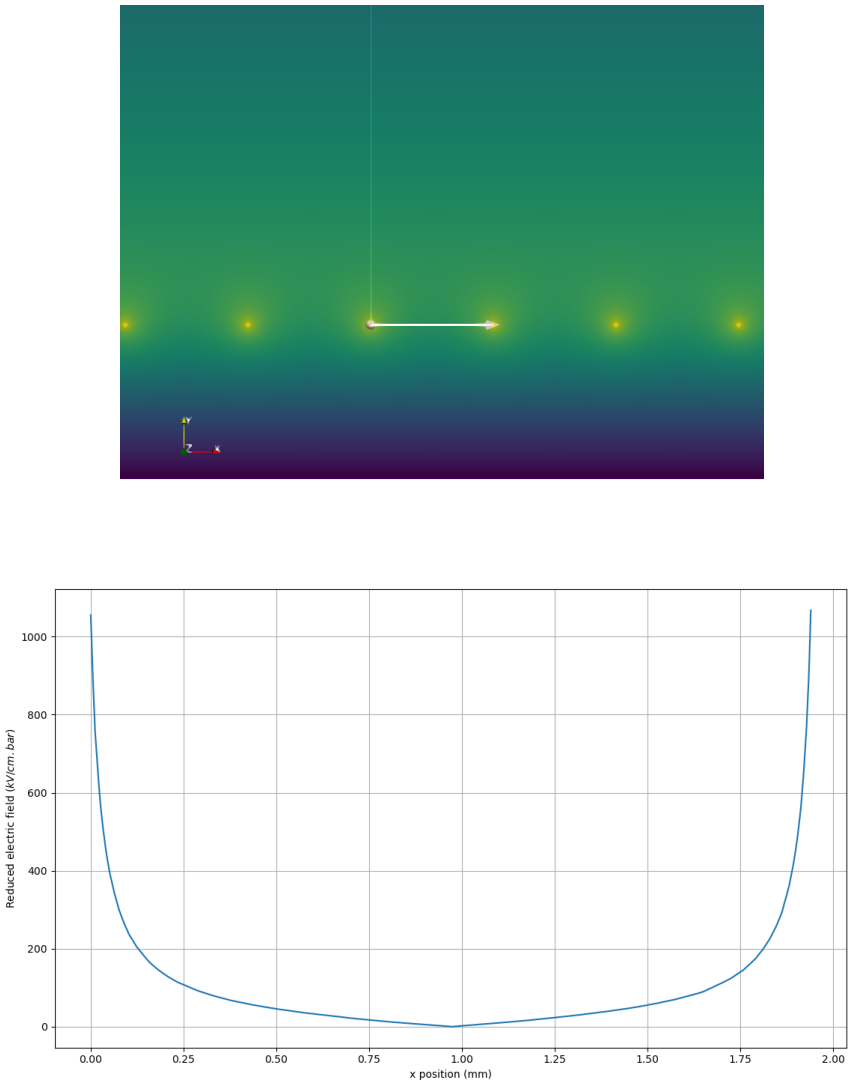


**Figure 5.13:** Above: geometrical representation of the line in the detector. Below: reduced electric field ($kVcm^{-1}\,bar^{-1}$) over a straight line from one wire ($x = 0\ mm$) to the consecutive other ($x = 2\ mm$) at atmospheric pressure.

Again, the reduced electric field close to the wires ($x \approx 0\ mm$ and $x \approx 2\ mm$) should be higher than the one indicated in fig. 5.13 below. The reduced electric field decreases as closer it gets to the middle, and in this point it appears to be approximately zero; however, it is minimal but not zero. This is due to program limitation in calculating infinite points.

## 5.4 Electron drift time

The *DriftLineRK* class gives the information about the end point of the current drift line, e.g., electron drift time [74]. The drift time is the time that a electron takes from their point of origin to the wires. Despite the possibility of simulating the ion drift time, only electron's was performed due to the computational effort required. The electron drift velocity is higher than ion drift velocity and thus the drifting time of ions is expected to be higher.

This simulations were not performed for the totality of events because of the computational resources needed. Each event has thousands of interactions, which one resulting in several electrons. This means that the resources required to analyse the drift time of all electrons are tremendous; therefore, only a representative number of events was selected. The chosen sample was around 5% of total events, i.e., 700 events, and they were randomly chosen. Fig. 5.14 represents the histogram of the electron drift time for this case.

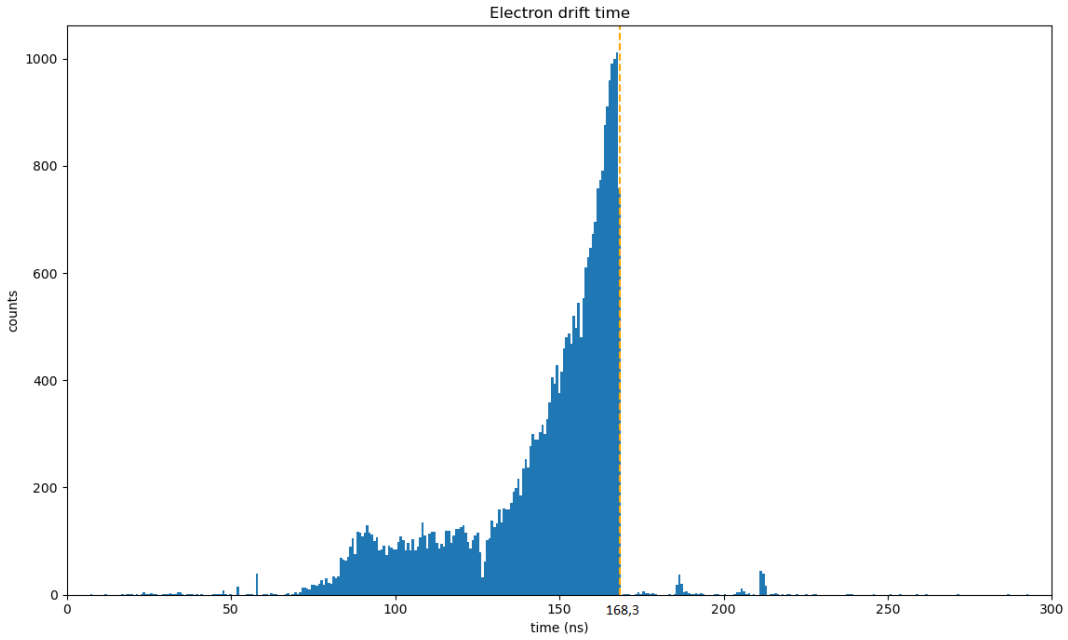


**Figure 5.14:** Histogram of the electron drift time for 700 random events.

From fig. 5.14 the electron drift time increases until a certain value. This value is indicated and is 168.3 *ns*. Electrons drift towards the wires with a certain drift velocity, which depend on the reduced electric field and on the type of gas (equation 5.1). For each point of the reduced electric field, the drift velocity may be defined; therefore, the maximum time it takes for an electron to reach the wires is also a concrete value: 168.3 *ns*. The region between $\sim$ 70 *ns* and $\sim$ 168.3 *ns* represent situations were the distance traveled by electrons is smaller. This may be because of interactions with gas molecules, or the proximity to the wires of the electron point of origin. Some fluctuations are visible outside of this interval and symbolize electrons with very small paths in the medium (bellow $\sim$ 70 *ns*), and electrons that for some reason do not go towards the wires (above 168.3 *ns*).

## 5.5 Induced current

The charged particles from the neutron capture reaction generate a free moving charge $q$ within the detector. The movement of $q$ and its multiplication in the gas induces a charge $Q$ on an electrode. Then $Q$ is amplified and converted to the output signal. This is the common principle of radiation detection techniques. The current induced by the drift of electrons and ions in the wires of detector A and B is calculated using the Shockley-Ramo theorem [81][82]. It states that the current $i$ on an electrode induced by a moving point charge $q$ in a position $r$ at a velocity $v$ is given by:

$$i(t) = -qv \cdot E_W(r) \tag{5.5}$$

where $E_W$ is the weighting field, which determines how charge movement couples to a specific electrode. It is the component of the electric field in the direction of $v$ at the charge's instantaneous position, under the following conditions: charge removed, given electrode raised to unit potential, and all other conductors grounded.

In *Garfield++* to simulate the induced current in the wires it is required a component class (*ComponentAnalyticField*) and a transport class (*DriftLineRKF*). In this case, both negative and positive charges were considered.

A random event was selected, and the induced current in the wires of both detectors A and B was plotted in fig. 5.15 and 5.16, respectively. The neutron impinges on the position (0, 0, 0) of the detector, due to the incident position of the neutron beam.

In both fig. 5.15 and fig. 5.16, the induced current as a function of the time is represented. On the wires nearest to the neutron initial position the induced current is negative (fig. 5.15c, 5.15d, 5.15e, 5.16c, 5.16d, 5.16e) due to the negative charge collected. From the electron drift lines in fig. 5.4 left, in detector A the electrons move towards the wires on the right, and in detector B on the left, ergo the induced current on the different wires will translate that behaviour. The same happens in fig. 5.15 and fig. 5.16, but not so pronounced: on detector B the current has a higher absolute value on wire 5 and then on wire 6. This means that the charged particle moved slightly towards the left side. Moreover, the current on wire 5 is higher in absolute because of the track on the particle: it became closer to wire 5 than to wire 6. In the same detector, wire 7 also shows a negative current due to the electrons that move to there when in the initial position. In detector A, this behaviour is less perceptible. In terms of the higher absolute value, wire 5 is the winner; however, its curve is not ideal. One possible justification is that the track of the charged particle was within the region of the sixth wire and thus also affected wires 5 and 7.

The furthest wires such as 1, 4, 8, and 11, represent a smaller positive charge due to the drift of ions. This is a very small current ($10^{-6}\ fC/ns \sim\ pA$) that can be considered zero. Wires 2, 3, 9, and 10 are not illustrated in these figures; however, the same conclusion can be taken.

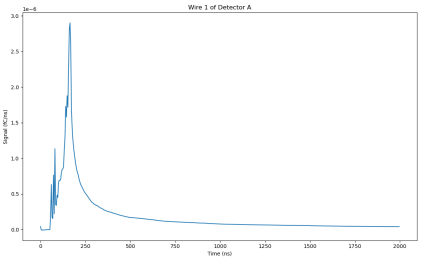


**(a)** Wire 1 of Detector A

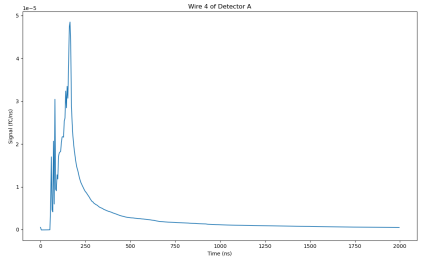


**(b)** Wire 4 of Detector A

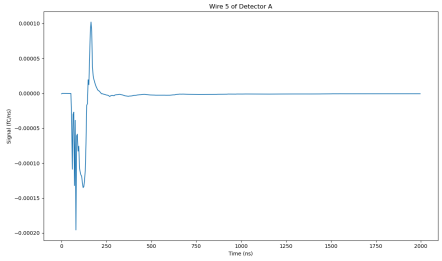


**(c)** Wire 5 of Detector A

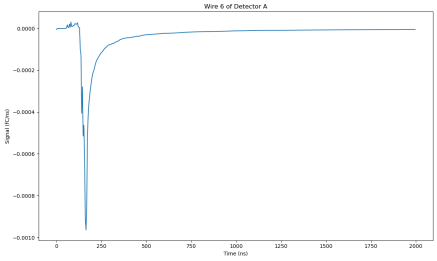


**(d)** Wire 6 of Detector A

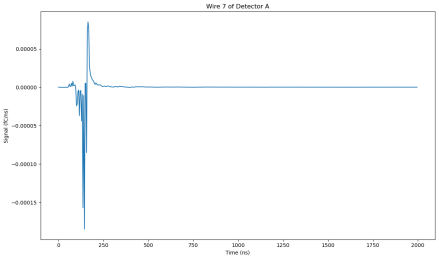


**(e)** Wire 7 of Detector A

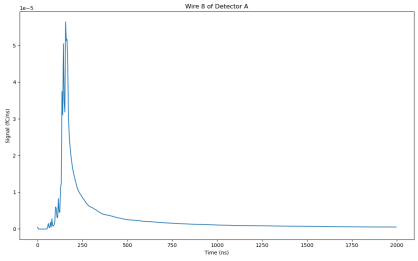


**(f)** Wire 8 of Detector A

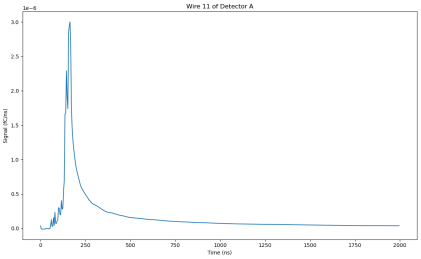


**(g)** Wire 11 of Detector A

**Figure 5.15:** Induced current ($fC/ns$) on wires 1, 4, 5, 6, 7, 8, and 11 of Detector A for a random event as a function of time ($ns$).

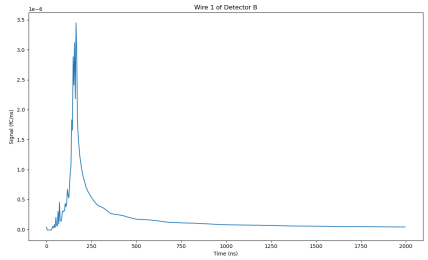


**(a)** Wire 1 of Detector B

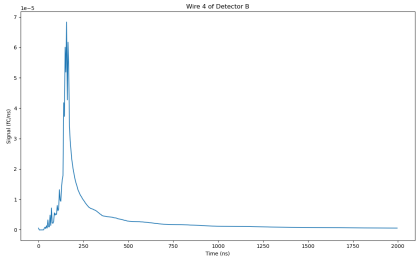


**(b)** Wire 4 of Detector B

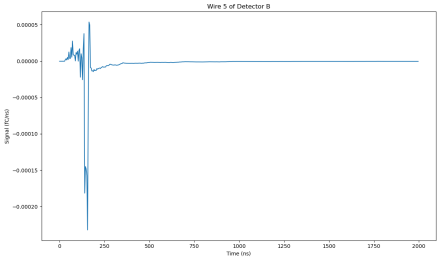


**(c)** Wire 5 of Detector B

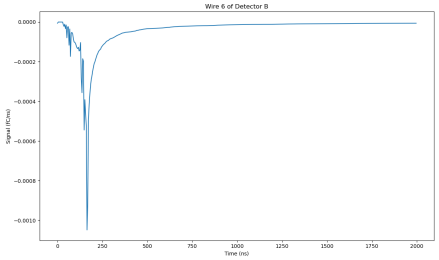


**(d)** Wire 6 of Detector B

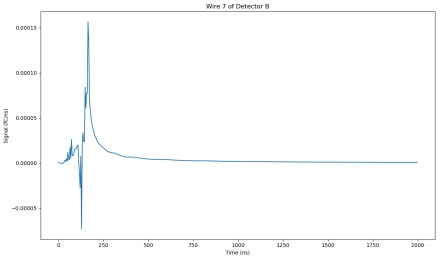


**(e)** Wire 7 of Detector B

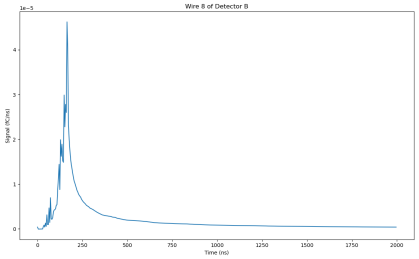


**(f)** Wire 8 of Detector B

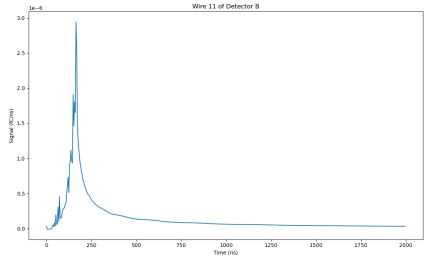


**(g)** Wire 11 of Detector B

**Figure 5.16:** Induced current ($fC/ns$) on wires 1, 4, 5, 6, 7, 8, and 11 of Detector B for a random event as a function of time ($ns$).

## 5.6 Spatial resolution

To calculate the spatial resolution of the coincidence detector, it is necessary to determine the signal readout of both readout systems, which is composed by two MWPCs (detector A and B). Each MWPCs has a set of wires connected by a resistive chain in order to obtain the one-dimension position of the neutron capture site by the charge division method. This way, two channels per MWPC are required. This is a much more simpler technique than using an individual readout for each wire.

The physical detector has 39 wires each connected by 120 Ω resistors. The first and last wire also have a resistor before the output, making a total of 40 resistors. Because the simulation only considered 11 wires in each detector, it is impossible to determine the spatial resolution for the 39 wires; however, an assumption can be made. Since all incoming neutrons are centered in the detector and since the induced current in the wires furthest from the center can be considered zero (Section 5.5), the calculated position of the neutron capture site is the same for a detector with 39 wires and 40 resistors, and a detector with 11 wires and 12 resistors. This will be discussed following.

From the simulation detector geometry (Section 5.1.2) each wire has a separation of 2 *mm*. A resistor is placed at each separation and next to the first and last wires. In both ends of the resistive chain a charge sensitive pre-amplifier is connected, which converts the current signals into voltage pulses. A representation of this readout system is in fig. 5.17.

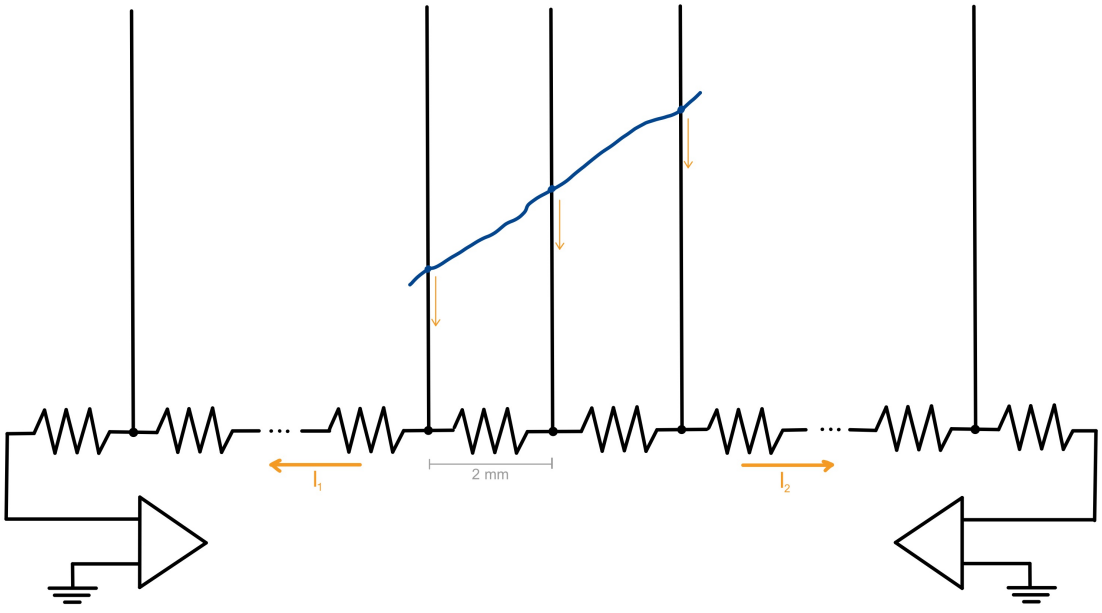


**Figure 5.17:** Readout system: MWPC. The blue line represents a particle track, the small orange arrows the induced current in each wire by the electrons, and the orange arrows ($I_1$ and $I_2$) the current in the resistive chain. Each end of the chain is connected to a charge sensitive pre-amplifier.

In the charge division method, the current is divided in proportion to the length from the point at which the wire is triggered. The position in one dimension of the interaction site is given by:

$$x = \frac{I_2}{I_1 + I_2} L \tag{5.6}$$

Being $I_1$ the current at one end of the resistive chain, $I_2$ the current at the other end, and $L$ the width of the MWPC. Given the Ohm's law: $I = \frac{V}{R}$, eq. 5.6 can be rewritten:

$$x = \frac{\frac{V}{R_2}}{\frac{V}{R_1} + \frac{V}{R_2}} L \Leftrightarrow x = \frac{1}{\frac{R_2}{R_1} + 1} L \tag{5.7}$$

Being $R_1$ and $R_2$ the resistors sum in the path between the end of the resistive chain and the location of the triggered wire. If an interaction occurs in the initial left side of the chain: $R_2 >> R_1$ then $x \approx 0$; if it occurs on the right side: $R_1 >> R_2$ then $x \approx L$; if it occurs in the middle of the chain: $R_1 = R_2$ then $x \approx \frac{L}{2}$. Consequently, the left-end of the resistive chain is the beginning of the coordinate system, i.e., $x = 0$.

Now it is necessary to calculate $I_1$ and $I_2$. From fig. 5.15 and fig. 5.16, the simulation gives the current ($fC/ns$) per time ($ns$). To obtain the current in respect to the peak of the collected charge of the ionizations, it was integrated until 10% of the absolute maximum value. Then this value was multiplied by the corresponding time, giving the current in each wire. The currents $I_1$ and $I_2$ are given by:

$$I_1 = \frac{I \cdot \sum_{R_{n+1}}^{R_N} R}{R_{total}} \qquad I_2 = \frac{I \cdot \sum_{R_1}^{R_n} R}{R_{total}} \tag{5.8}$$

where $N$ is the total number of resistors, $n$ the resistor number on the left side of the triggered wire, and $n + 1$ on the right side of the same wire.

The position $x$ was calculated for all events in the detector A and in the detector B and then plotted. The graphics were translated for the position coordinates to correspond to the detector's coordinates. A gaussian curve was fitted: its parameters are in the following figures.

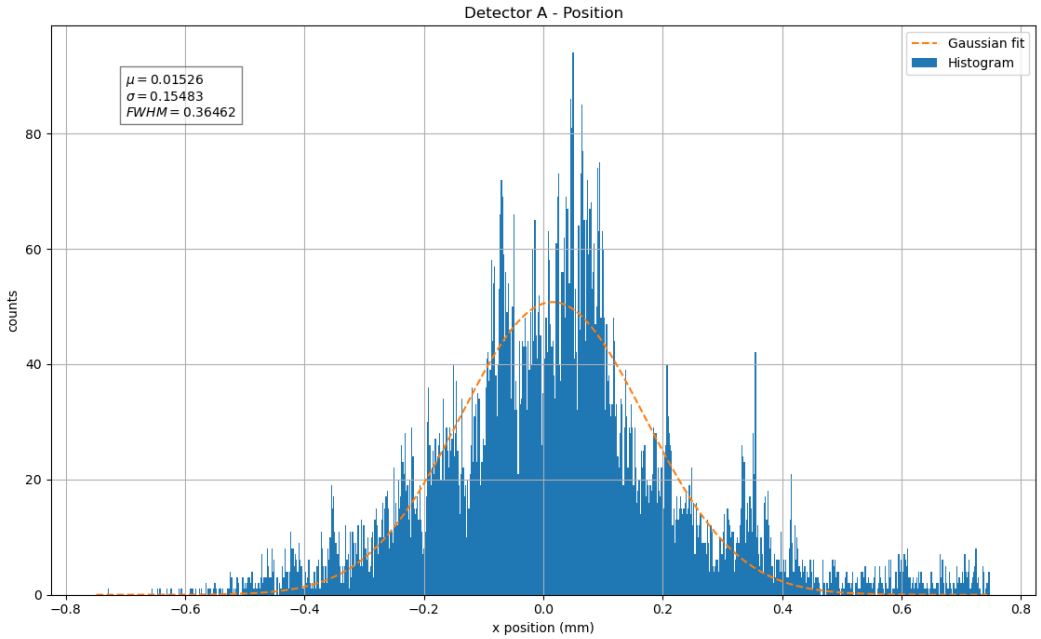


**Figure 5.18:** Histogram of the estimated positions in detector A from the pre-selected events. The gaussian curve parameters are in the figure.

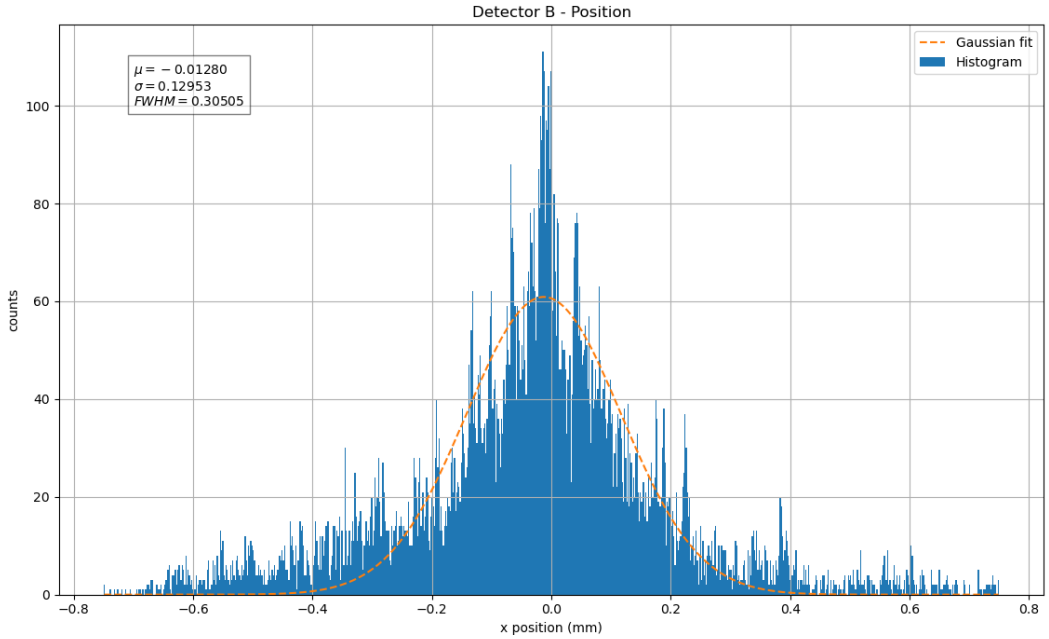


**Figure 5.19:** Histogram of the estimated positions in detector B from the pre-selected events. The gaussian curve parameters are in the figure.

The FWHM gives the spatial resolution. For detector A it is $FWHM_A = 0.36\,mm$, and for detector B $FWHM_B = 0.31\,mm$, both calculated from the gaussian fit. Eq. 2.28 gives

the minimal theoretical value for the spatial resolution. For a pitch between wires of 2 $mm$: $\sigma = \frac{2}{\sqrt{12}} = 0.58mm$, which is higher than $FWHM_A$ and $FWHM_B$. Consequently, the spatial resolutions of detectors A and B are not correct. This aspect will be discussed next along with the spatial resolution of the coincidence detector.

To reconstruct the neutron capture site from the secondary particle's position in detectors A and B there are to possible estimations: the arithmetic mean, and the energy weighted average. The first consists on the arithmetic mean of the estimated positions of each detector A and B. Equation 5.9 gives the reconstructed neutron capture site by this method.

$$x_{coinc} = \frac{x_A + x_B}{2} \tag{5.9}$$

The energy weighted average consists on weighting the estimated position of the charged particle in a detector by the energy of the other detected in the opposite detector. Equation 5.10 gives the reconstructed neutron capture position from this technique.

$$x_{coinc} = \frac{x_A E_B + x_B E_A}{E_A + E_B} \tag{5.10}$$

Since both secondary particles have different ranges in the detection layer and in the gas, depending on the location of the neutron capture reaction in the detection layer, one can have a longer track than the other. If the reaction occurs near the boron surface with the gas, one particle will escape the layer with higher energy, while the other will have to go through a substantial thickness of converter and substrate materials; therefore, escaping with lower energy.

For the symmetric Boron-10 coating, the two formulas produce very similar results [64]. This is because the boron deposited on both sides of the Mylar foil translate to a more balanced energy deposition in detectors A and B. The arithmetic mean method was used.

The reconstructed neutron capture site was calculated for all events. Again, the graphics were translated for the position coordinates to correspond to the detector's coordinates. A gaussian curve was fitted.

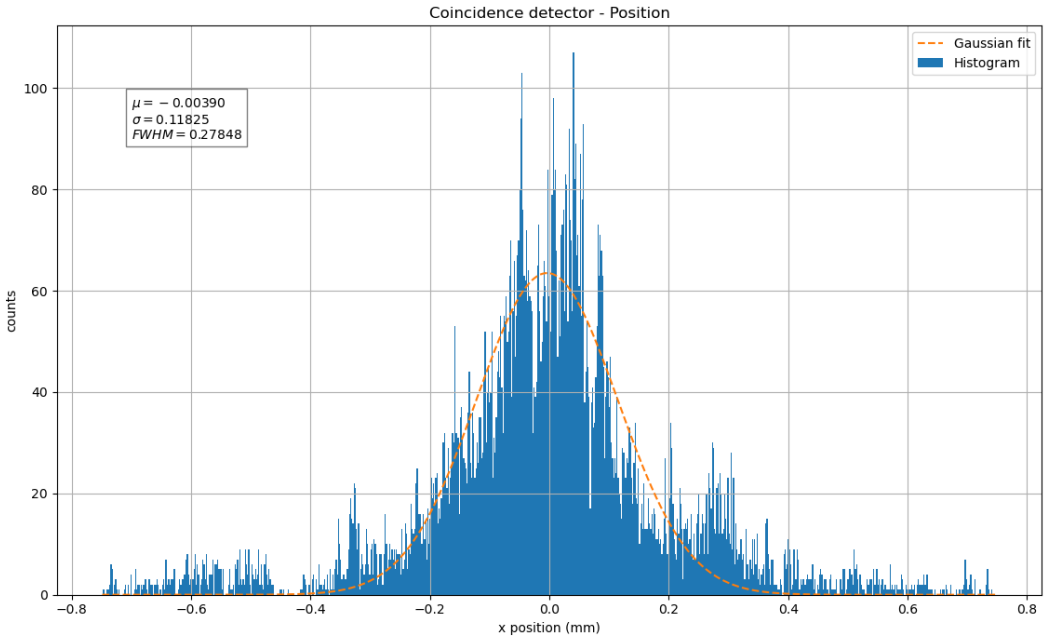


**Figure 5.20:** Histogram of the reconstructed positions in the coincidence detector from the estimated positions of detectors A and B. The gaussian curve parameters are in the figure.

The spatial resolution of the coincidence detector is 0.28 *mm* (FWHM). This value is similar to the one estimated from the GEANT4 simulations [64]; however, the latter was calculated regarding only the position of each interaction and the energy deposited by the secondary particle there [64] [65]. The estimated position from Garfield++ is obtained considering the induced signal produced by each event in each detector A and B, and thus should be more realistic.

The pre-selection of events consisted on: having coincidence in detectors A and B, having a particle's energy higher than the threshold energy (100 keV) along its track, and having some movement after each interaction with the gas particles. This means that the simulation was performed with the less energetic charged particles that escaped from the Boron-10 layer and the mylar substrate and that are within the pre-selected events. From the interactions between the particles and the gas particles, the first deposits all its energy in the material. If its energy is low since it escapes the detection layer, it is lost more rapidly; therefore, the particle travels a lower distance inside the material, i.e., has a lower range. Since particles are expected to escape the detection layer near the (x,y) position (0,0), which is the neutron incident site, its reconstructed position is a gaussian curve centered around (0,0) with a very small FWHM due to the small range.

Other important factor is the low statistic derived from the low number of pre-selected events from GEANT4 simulations [64]: the intrinsic detection efficiency obtained from this selection is 1.33%.

# Chapter 6

# Experimental setup

## 6.1 Detector

The Coincidence Detector is composed by two cathode planes, two MWPCs as readout systems, and a detection layer, and is filled with Ar:$CO_2$. The detector is symmetric in respect to the detection layer in order to achieve its working principle to reconstruct the neutron capture site.

The cathode are $100 \times 100\, mm^2$ aluminium planes with a thickness of $3\, mm$. It was the chosen material due to its robustness at this thickness and due to its transparency to neutrons.

The detection layer is a $0.5\, \mu m$ enriched $^{10}B_4C$ coating deposited on each side of the $0.9\, \mu m$ Mylar foil. Its effective area is around $100 \times 100\, mm^2$, and it is placed in a frame.

The two readout systems consist on two MWPCs. Each has 39 wires with a gap between them of 2 mm. The wires are connected by 38 resistors and 2 are added before the first and after the last wire, making a total of 40 120 Ω resistors. The wires are 100 mm long and made of gold-coated tungsten with a diameter of 50 $\mu m$; therefore, the detection layer as an active area of $100 \times 100\, mm^2$. The wires and the resistors are placed on a G10 frame. The resistors are covered in tape to protect them and the wire connection from external influences. A photograph of a single MWPC is present in fig. 6.1.

The detector is protected inside a stainless steel vessel with lateral inlets and outlets on opposing sides for the gas to flow through the detector. The detector structure is mounted on four pillars to allow flexibility to change its layout: the distance between the planes can be increase or decreased, and other components can be added if necessary.

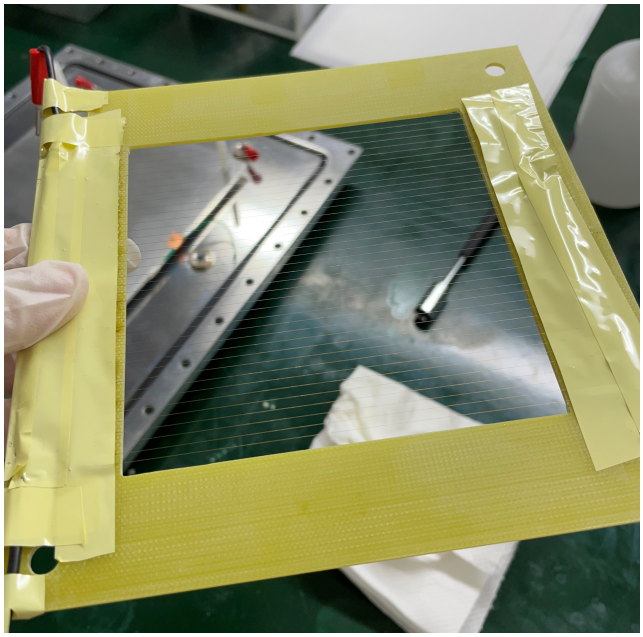

**Figure 6.1:** Photograph of one of the two MWPC: 39 wires with a pitch of 2 mm between them connected with 40 120 Ω resistors. The resistors are covered in tape.

## 6.2 ICNAS and experimental setup

Neutron sources are limited, and thus difficult to access. Besides the sources explained in Section 2.2.1, cyclotrons can also be used as a source of protons to generate neutrons.

ICNAS (Institute for Nuclear Sciences Applied to Health) is a research facility of the University of Coimbra. It congregates the main medical imaging modalities (PET, MRI, CT, EEG) in the same building, including cyclotron and radiochemistry facilities. The facility has two cyclotrons for the production and investigation of radionuclides and radiopharmaceuticals [83]. One cyclotron is the Cyclone KIUBE [84] from IBA (Ion Beam Applications).

Neutrons are emitted in the production of the radionuclide $^{18}$F. In the cyclotron it is produced by the $^{18}$O(n, p)$^{18}$F reaction, where protons are accelerated until reaching an energy of 18 MeV into a liquid enriched $^{18}$O water target. This process emits fast neutrons with an energy range up to 15 MeV, approximately, and a peak centered at 1 MeV [85]. For this energy range, neutron moderation is required. The simpler way of doing so is through hydrogen, e.g., hydrogenous materials. The process of producing $^{18}$F also emits gamma-rays isotropically with high intensity and with an energy range up to 10 MeV, approximately [85].

Because of radiation, the cyclotron is inside a bunker. For the same reason, only the pre-amplifier was installed near it. The remaining components, such as the HV power, and the computer, were placed outside of the bunker due to radiation damage. The filling gas used was Ar:$CO_2$ (80:20), and its bottle was also placed outside. The electric cables and the gas tubes passed under the floor to the inside of the bunker.

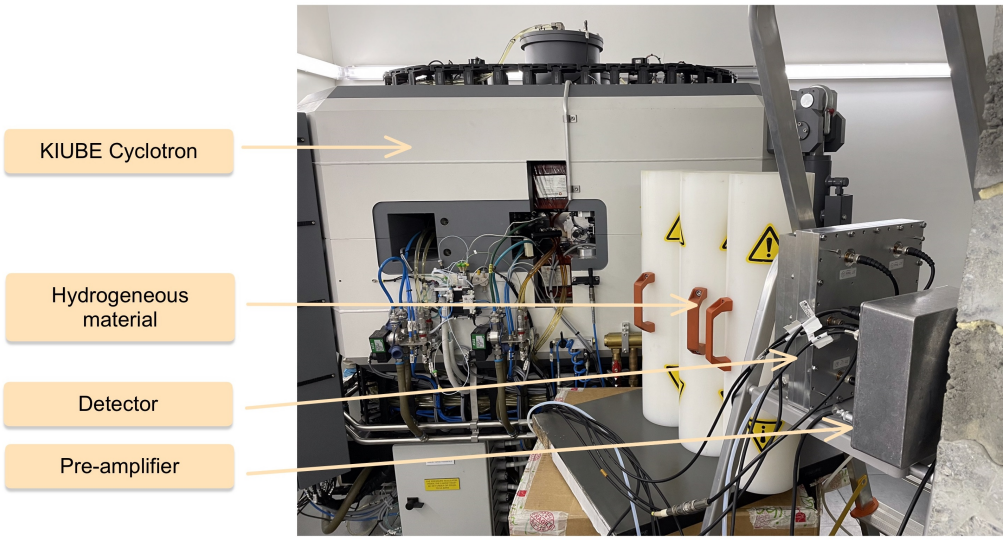


**Figure 6.2:** Experimental setup at ICNAS for irradiation neutrons from the KIUBE cyclotron moderated by hydrogenous material placed between the detector and the cyclotron.

Before starting the measurements, the gas flow was opened for about one hour to purify the gas inside the detector. After that, the cyclotron was switched on. Due to radiation high levels inside the bunker, irradiation times must be kept as minimal as possible for safety reasons. Increasing this time will increase the radiation, and consequently the waiting time before entering the bunker. For this reason, the switched-on time was kept minimal.

## 6.3 Results

Because it is not possible to polarize the pre-amplifier used, the applied voltages were: the wires at ground potential, the boron planes at a negative HV, and the cathode planes at a higher negative HV. Table 6.1 indicates the applied voltages in the detector during the tests.

| Wire voltage (V) | Boron plane voltage (V) | Cathode voltage (V) |
|---|---|---|
| 0 | -900 | -1200 |

**Table 6.1:** Wire, boron plane, and cathode voltages applied in the detector for the experimental setup.

During operation, the detector was kept stable without electrical discharges. The PHS was acquired in four locations: in the two outputs of detector A (up and down), and in the corresponding two outputs of detector B (up and down also). Fig. 6.3 represents the two PHS of both detectors.

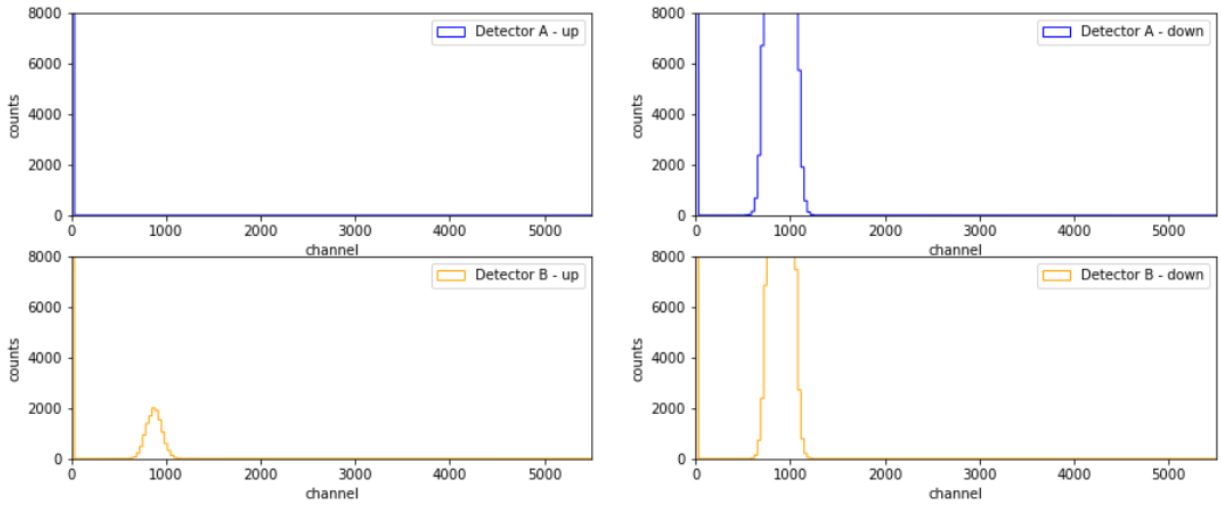


**Figure 6.3:** PHS acquired for the four pre-amplifiers with the proton beam switched on. First row: PHS's corresponding to the two outputs in detector A, up (left) and down (right); second row: PHS's corresponding to the two outputs in detector B, up (left) and down (right).

The KIUBE cyclotron produces neutrons, but also gamma-rays. These are emitted isotropically with high intensity. Consequently, in this environment the background signal was considerable: added to the electronic noise, the gamma interaction rate in the detector was excessively high. Comparing to neutrons, the gamma-ray counting rate was far superior, superimposing with the signal from neutron detections (fig. 6.3). It was not possible to observe a energy peak corresponding to a coincidence event, i.e., a simultaneous detection of an $\alpha$-particle and a $^{7}$Li ion of a neutron capture reaction.

# Chapter 7

# Conclusion and future work

A simulation of signals in the coincidence detector based on the interaction of neutrons was performed using Garfield++. The intrinsic detection efficiency is 1.33% obtained from the pre-selection of events of GEANT4 simulations. A gain study was done in order to optimize the applied voltage in the wires, in the boron plane and in the cathode plane. First the gain dependence on the applied voltages was analyzed by varying the wire and the boron plane voltage separately. The optimal voltages are 3000 V in the wires, 1000 V in the boron plane, and 0 V in the cathode, corresponding to a gain of 1213.32. Next a study of the gain dependence on the electron initial position was also done. When it is launched along the y-axis, the gain has a minimal variation; however, along the x-axis that is not the case. If the electron's initial position is directly above the wires, the gain is 1213.31; if it is directly between two wires, the gain is 1365.26. The relative error between the two is 11.11%.

The electric field is critical to a good detector performance; therefore, four regions were evaluated: between the boron plane and the wires, along the y-axis of all detector passing between the wires and right above the wires, and between two consecutive wires. As expected, the reduced electric field increases in the wire's neighborhood, being maximum near it. Close to the boron and the cathode plane, the reduced electric field is constant. Related to the electric field, the electron drift time was found to have a maximum value of 168.3 *ns*. This value corresponds to the distance between the electron point of origin and the wire.

The drift of electrons and ions inside the detector induces a current on the wires. On the ones nearest to the neutron incident position, the induced current is negative and higher in absolute because of the negative charge collected and the multiplication process in this region. The furthest wires represent a smaller positive charge due to the drift of ions, which can be neglected.

Finally, the neutron interaction site and the spatial resolution were determined. The FWHM of detector A is 0.36 *mm*, and of detector B is 0.31 *mm*. The reconstruction of the neutron capture site was performed through the arithmetic mean of the estimated position in each detector A and B. The spatial resolution of the coincidence detector is 0.28 *mm*; however, this is not a realistic value. From the pre-selection of events, only the ones with lower energies were chosen. This selection translates to a smaller particle range in the gas medium, meaning that particles will not go far from their point of origin, inducing an error in the reconstructed position. Other factors may have influenced the spatial resolution: the method to reconstruct the neutron capture site, and the low statistic derived from the

low number of pre-selected events. To improve the simulation work, the incident neutron position should be reconstructed using the energy weighted average method. This way there will be a balance between the particles' path and its deposited energy in the gas. Since it is difficult to increase the number of pre-selected events without repeating the GEANT4 simulations, a study of the secondary particles' energy and its ranges should be helpful to understand its limitations.

The coincidence detector was tested at ICNAS, which is a research facility of the University of Coimbra. ICNAS has a cyclotron for production of radionuclides and radiopharmaceuticals. From this process fast neutrons and gamma-rays are emitted. After equipment configuration and neutron moderation, the detector was tested. The high gamma-ray interaction rate, did not allow the visualization of neutron detection; therefore, other neutron source must be used. For future testing the ideal is to use a neutron source with less intense gamma-ray background, and with a well characterized neutron beam, such as the SINQ facility at PSI, Switzerland.

# Bibliography


[1] J. Chadwick (1932), *Possible existence of a neutron*, Nature 129, 312

[2] J. Chadwick (1932), *The existence of a neutron*, Proc. Roy. Soc. A 136, 692-708

[3] I. S. Anderson, R. L. McGreevy, H. Z. Bilheux (2009), *Neutron Imaging and Applications*, Springer

[4] Nicholas Tsoulfanidis, Sheldon Landsberger (2015), *Measurement and Detection of Radiation*, 4th edition, CRC Press

[5] William R. Leo (1987), *Techniques for nuclear and particle physics experiments: a how-to approach*, Springer-Verlag

[6] Glenn F. Knoll (2009), *Radiation detection and measurement*, 3th edition, John Wiley & Sons Inc.

[7] T. Jevremovic (2005), *Nuclear princials in engineering*, Springer Science+Business Media Inc.

[8] F. Piscitelli (2013), *Boron-10 layers, neutron reflectometry and thermal neutron gaseous detectors*, PhD Thesis, University of Perugia

[9] F. E. Wietfeldt (2018), *Measurements of the neutron lifetime*, Atoms, 6(4), 70

[10] Gregory R. Choppin, Jan-Olov Liljenzin, Jan Rydberg (2002), *Radiochemistry and Nuclear Chemistry*, 3th edition, Butterworth-Heinemann

[11] Institute Laue Langevin (France), `https://www.ill.eu/`. Accessed: 2022-07-10

[12] Source Heinz Maier-Leibnitz (Germany), `https://mlz-garching.de/englisch.html`. Accessed: 2022-07-10

[13] PIK reactor (Russia), `http://www.pnpi.spb.ru/en/facilities/reactor-pik`. Accessed: 2022-06-16

[14] W.E. Fischer (1997), *SINQ - The spallation neutron source, a new research facility at PSI*, AIP Conference Proceedings 392, 1119

[15] Jeffrey S. Nico, W. Michael Snow (2005) *Fundamental neutron physics*, Annu. Rev. Nucl. Part. Sci. 2005. 55, pg 27–69

[16] K. Kirch, B. Lauss (2020), *Ultracold neutrons*, Swiss Neutron News, vol 55, 6-25

[17] T. W. Crane, M. P. Baker (1991), *Neutron detectors. Passive nondesctructive assay of nuclear materials*, chapter 13, 379-406

[18] Stefaan Tavernier (2010), *Experimental techniques in nuclear and particle physics*, Springer-Verlag

[19] National Nuclear Data Center. `https://www.nndc.bnl.gov/sigma/`. Accessed: 2022-07-11

[20] A. Khaplanova, F. Piscitelli, J.-C. Buffet, J.-F. Clergeau, J. Correa, P. van Esch, M. Ferraton, B. Guerard, R. Hall-Wilton (2013), *Investigation of gamma-ray sensitivity of neutron detectors based on thin converter films*, J. Instrum., 8(10): P10025–P10025

[21] D.H. Bedding, N.H. Johnson, H.O. Menlove (200), *$^3$He neutron proportional counter performance in high gamma-ray dose environments*, Nuclear Inst. and Methods in Physics Research, A vol. 455, 670-682

[22] Fabio Sauli (2014), *Gaseous radiation detectors - fundamentals and applications*, Cambridge university press

[23] W. Diethorn (1956), *A methane proportional counter system for natural radiocarbon measurements*, Technical report, United States atomic energy commission, Technical information service

[24] Edoardo Rossi (2015), *Characterisation of the spatial resolution and the gamma-ray discrimination of helium-3 proportional counters*, Master's thesis, Università degli Studi di Milano-Bicocca

[25] David R. Lide (1998), *CRC Handbook of Chemistry and Physics*, 79th edition, CRC Press

[26] L. L. Lucas, M. P. Unterweger (2000), *Comprehensive review and critical evaluation of the half-life of tritium*, J. Res. Natl. Inst. Stand., vol. 105, 541-549

[27] Dana A. Shea, Daniel Morgan (2010), *The Helium-3 Shortage: Supply, Demand, and Options for Congress*, Congressional Research Service

[28] House Hearing, 111 Congress (2010), *Caught by surprise: causes and consequences of the Helium-3 supply crisis*, U.S. Government Publishing Office, Subcommittee on investigations and oversight, Committee on science and technology, House of representatives, Serial No. 111-92

[29] Adrian Cho (2009), *Helium-3 shortage could put freeze on low-temperature research*, Science, vol. 326, 778-779

[30] Allan J. Hurd, Richard T. Kouzes (2014) *Why new neutron detector materials must replace helium-3*, Eur. Phys. J. Plus, 129, 1-3

[31] Richard T. Kouzes, Azaree T. Lintereur, Edward R. Siciliano (2015) *Progress in alternative neutron detection to address the helium-3 shortage*, Nuclear Inst. and Methods in Physics Research, A vol. 784, 172-175

[32] Richard Stone (2016) *Researchers rise to challenge of replacing helium-3*, Science, vol. 353, 15-16

[33] ISIS (United Kingdom), https://www.isis.stfc.ac.uk/Pages/home.aspx. Accessed: 2022-06-16

[34] SINQ (Switzerland), https://www.psi.ch/en/sinq. Accessed: 2022-06-16

[35] SNS (EUA), https://neutrons.ornl.gov/sns. Accessed: 2022-06-16

[36] J-PARC (Japan), http://j-parc.jp/c/en/. Accessed: 2022-06-16

[37] CSNS (China), http://english.ihep.cas.cn/csns/. Accessed: 2022-06-16

[38] The ESS mandate, https://europeanspallationsource.se/ess-mandate. Accessed: 2022-06-16

[39] S. Peggs, et al (2013), *ESS Technical Design Report*, ESS-doc-274-v15, European Spallation Source

[40] K. H. Andersen et al (2020), *The instrument suite of the European Spallation Source*, Nuclear Inst. and Methods in Physics Research, A vol. 957

[41] V. Santoro, et al (2020), *Development of High Intensity Neutron Source at the European Spallation Source*, Journal of Neutron Research, vol. 22, no. 2-3, pp. 209-219

[42] Oliver Kirstein, et al (2014), *Neutron Position Sensitive Detectors for the ESS*, The 23rd International Workshop on Vertex Detectors, September 15-19 2014, Macha Lake, The Czech Republic

[43] F. D.Amaro, C. M. B. Monteiro, J. M. F. dos Santos, A.Antognini (2017), *Novel concept for neutron detection: proportional counter filled with $^{10}B$ nanoparticle aerosol*

[44] A. Ravazzani, et al (2006), *Characterisation of $^{3}He$ proportional counters*, Radiation measurements, vol 41, 582-593

[45] B. Oryema, M. A. M. Nader, S. A. E. Agamy (2017), *Response function estimation for in-core $BF_3$ and $^{3}He$ neutron detectors using MCNPX - case study of opal reactor*, Advances in Applied Science Research, 8(3), 76-89

[46] Kevin S. McKinny, Thomas R. Anderson, and Nathan H. Johnson (2013), *Optimization of Coating in Boron-10 Lined Proportional Counters*, IEEE Transactions on nuclear science, vol. 60, No. 2

[47] Jeffrey L. Lacy, Athanasios Athanasiades, Liang SunChristopher S. Martin, Tom D. Lyons, Michael A. Foss, Hal B. Haygood (2011), *Boron-coated straws as a replacement for $^{3}He$-based neutron detectors*, Nuclear Inst. and Methods in Physics Research, A vol. 652, 359–363

[48] J. L. Lacy, A. Athanasiades, N. N. Shehad, R. A. Austin, and C. S. Martin (2002), *Novel Neutron Detector for High Rate Imaging Applications*, 2002 IEEE Nuclear Science Symposium Conference Record

[49] Jeffrey L. Lacy, Athanasios Athanasiades, Liang Sun, Christopher S. Martin, and Gerson J. Vazquez-Flores (2009), *Boron Coated Straw Detectors as a Replacement for $^{3}He$*, 2009 IEEE Nuclear Science Symposium Conference Record (NSS/MIC)

[50] J. L. Lacy, A. Athanasiades, C. S. Martin, L. Sun, and G. J. Vazquez-Flores (2013), *The evolution of neutron straw detector applications in homeland security*, IEEE Trans. Nucl. Sci., 60(2), 1140–1146

[51] Proportional technologies, Inc., `https://www.proportionaltech.com/pages/products`. Accessed: 2022-07-19

[52] K. Andersen, et al (2013), *$^{10}B$ multi-grid proportional gas counters for large area thermal neutron detectors*, Nuclear Inst. and Methods in Physics Research, A vol. 720, pg. 116-121

[53] Eszter Dian (2019), *Optimisation of Signal-to-Background Ratio for Thermal Neutron Detectors*, PhD Thesis, HAS Centre for Energy Research, Budapest University of Technology and Economics

[54] K. Andersen, et al (2012), *Multi-grid Boron-10 detector for large area applications in neutron scattering science*, presented at the ICANS-XX conference, March 2012

[55] Bruno Guerard, Richard Hall-Wilton, and Fabrizio Murtas (2013), *Prospects in MPGDs development for neutron detection*, Accademia-Industry Matching Event, CERN October 14-15, 2013

[56] Gabriele Croci, Fabrizio Murtas, and Filippo Resnati (2016), *Prospects in MPGDs development for neutron detection*, Accademia-Industry Matching Event, CERN March 16-17, 2015

[57] Fabio Sauli (2016), *The gas electron multiplier (GEM): Operating principles and applications*, Nuclear Inst. and Methods in Physics Research, A vol. 805, 2-24

[58] Andrea Muraro, et al (2018), *Performance of the high-efficiency thermal neutron BAND-GEM detector*, Progress of Theoretical and Experimental Physics, vol. 2018, Issue 2, February 2018, 023H01

[59] Giogia Albani, et al (2020), *High-rate measurements of the novel BAND-GEM technology for thermal neutron detection at spallation sources*, Nuclear Inst. and Methods in Physics Research, A vol. 805, 163389

[60] A. Breskin, R. Alon a, M. Cortesi, R. Chechik, J. Miyamotoa V. Dangendorf, J. Maia, and J. M. F. Dos Santos (2009), *A concise review on THGEM detectors*, Nuclear Inst. and Methods in Physics Research, A vol. 598, Issue 1, pg. 107-111

[61] M. Cortesi, R. Zboray, A. Kaestner, and H. M. Prasser (2013), *Development of a cold-neutron imaging detector based on thick gaseous electron multiplier*, Rev. Sci. Instrum. 84, 023305

[62] Jianrong Zhou, Qinglei Xiu, Xiaojuan Zhou, Jianjin Zhou, Lingling Mad, Christian J. Schmidt, Martin Klein, Yuanguang Xia, Lin Zhu, Chaoqiang Huang, Guangai Sun, Bitao Hu, Zhijia Sun and Yuanbo Chen (2020), *Highly efficient GEM-based neutron detector for China Spallation Neutron Source*, Nuclear Inst. and Methods in Physics Research, A vol. 953, 163051

[63] G. Albani, G. Crocci, C. Cazzaniga, M. Cavenago, G. Claps, A. Muraro, F. Murtas, R. Pasqualotto, E. Perelli Cippo, M. Rebai, M. Tardocchi, and G. Gorini (2015), *Neutron beam imaging with GEM detectors*, 16th International Workshop on Radiation Imaging Detectors, 22-26 June 2014, Trieste, Italy

[64] N. F. V. Duarte (2021), *Proportional counters equipped with submicrometric $B_4C$ conversion layers for neutron detection*, PhD Thesis, University of Coimbra

[65] N. F. V. Duarte, J. S. Marcos, A. Antognini, C. Klauser, S. A. Felix, C. M. B. Monteiro, and F. D. Amaro (2022), *Improving position resolution of neutron detectors with ultra-thin $B_4C$ foils*, Journal of Instrumentation, vol 17

[66] Mewlude Imam (2016), *Chemical vapour deposition of boron-carbon thin films from organoboron precursors*, Licentiate thesis No. 1741, Linkoping Studies in Science and Technology

[67] K. Ahmed, et al (2017), *Solid-state neutron detectors based on thickness scalable hexagonal boron nitride*, Appl. Phys. Lett., 110, 13-16

[68] Carina Höglund, et al (2015), *Stability of $^{10}B_4C$ thin films under neutron radiation*, Radiation Physics and Chemistry, 113, 14–19

[69] Feng Shi (2018), *Introductory Chapter: Basic Theory of Magnetron Sputtering*, DOI: 10.5772/intechopen.80550

[70] I. Stefanescu, et al (2013), *Development of a novel macrostructured cathode for large-area neutron detectors based on the $^{10}B$-containing solid converter*, Nuclear Inst. and Methods in Physics Research, A vol. 727, 109-125

[71] A. P. Caricato, et al (2019), *Wavelength, fluence and substrate-dependent room temperature pulsed laser deposited B-enriched thick films*, Applied Surface Science, 483, 1044-1051

[72] M. Cesaria, et al (2020), *$^{10}B$-based films grown by pulsed laser deposition for neutron conversion applications*, Applied Physics A: Materials Science and Processing, vol. 126 (6), 404

[73] Z. Fang, et al (2019), *Realization and evaluation of the Boron Nano Particle-based drip-coating method for boron-lined gaseous neutron detectors*, Journal of Instrumentation, vol. 14

[74] H. Schindler (2022), *Garfield++ User Guide*, `https://garfieldpp.web.cern.ch/garfieldpp/documentation/UserGuide.pdf`. Accessed: 2022-06-25

[75] Stephen Biagi, *Magboltz - transport of electrons in gas mixtures*, `https://magboltz.web.cern.ch/magboltz/`. Accessed: 2022-06-25

[76] S. F. Biagi (1999), *Monte Carlo simulation of electron drift and diffusion in counting gases under the influence of electric and magnetic fields*, Nuclear Inst. and Methods in Physics Research, A vol. 421, 234-240

[77] R. Brun, F. Rademakers, et al, *ROOT: An Object-Oriented Data Analysis Framework*, `https://root.cern/`. Accessed: 2022-06-25

[78] S. J. Ross et al (2013), *Charge-Focusing Readout of Time Projection Chambers*, IEEE Nuclear Science Symposium and Medical Imaging Conference, October 29-November 3, 2012

[79] Salome, https://www.salome-platform.org/. Accessed: 2022-07-13

[80] Elmer FM, http://www.elmerfem.org/blog/. Accessed: 2022-07-13

[81] S. Ramo (1939), *Currents Induced by Electron Motion*, Proceedings of the I.R.E., vol 27, 584-585

[82] W. Shockley (1938), *Currents to Conductors Induced by a Moving Point Charge*, J. Appl. Phys., vol 9, 635-636

[83] ICNAS (Coimbra, Portugal), https://www.uc.pt/icnas. Accessed: 2022-08-12

[84] Cyclone KIUBE, https://www.iba-radiopharmasolutions.com/cyclone-kiube. Accessed: 2022-08-12

[85] IBA Radiopharma Solutions. The Cyclone KIUBE Site Requirement Guide.